Preparation and Applications of Multidimensional Graphene Oxide-Based Materials

Dongwoo Kang

Department of Energy Engineering

Graduate School of UNIST

2017

Preparation and Applications of Multidimensional Graphene Oxide-Based Materials

A thesis submitted to the Graduate School of UNIST in partial fulfillment of the requirements for the degree of Doctor of Philosophy

Dongwoo Kang

12. 20. 2016

Approved by

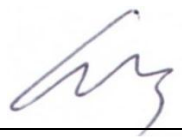

Advisor

Hyeon Suk Shin

Preparation and Applications of Multidimensional Graphene Oxide-Based Materials

Dongwoo Kang

This certifies that the thesis of Dongwoo Kang is approved.

12. 20. 2016

Advisor: Hyeon Suk Shin

Young-Bin Park

Ji-Hyun Jang

Jong-Beom Baek

Hyunhyub Ko

This dissertation is dedicated to my lovely wife and family.

Abstract

Graphene is well known to have excellent electronic, mechanical and thermal properties, but it is still challenges to apply its intrinsic properties to real applications. One possible route to utilizing these properties for applications would be to incorporate graphene sheets in a composite material. Many approaches have been studied for the fabrication of graphene and graphene oxide (GO)-based composite materials with polymer, carbon nanomaterials and metal nanoparticles. This thesis is aimed at discussing the fabrication methods and applications of GO-based high performance composites.

There have been many studies on GO-based composite materials, among which PVA has been considered as the most suitable polymer for GO-based composite applications. For various practical applications, it is very important to improve the mechanical properties of PVA. A large amount of oxygen-containing functional groups inserted onto the GO surface can form strong hydrogen bonds with the hydroxyl group of PVA. In this thesis, we have successfully fabricated PVA-GO composite films and fibers with improved mechanical strength by forming an additional adhesion properties from poly(dopamine) layers between the GO and PVA. The fabricated PVA/GO composite films and fibers resulted in increases in tensile modulus, ultimate tensile strength, and strain-to-failure. A combination of hydrogen bonding, strong adhesion of poly(dopamine) at the interface of PVA and GO sheets resulted in increases in tensile modulus, ultimate tensile strength, and strain-to-failure. In addition, the electrical conductivity of PVA/GO composite films and fibers can be restored owing to the partially reduced GO, and its application on humidity sensing and piezoresistive sensing will also be discussed.

The excellent electrical properties and high specific surface area of graphene can provide a positive effect on various energy storage materials. However, the tendency to restack between sheets always remains to be solved. In this thesis, two-dimensional (2D) GO sheets were assembled into three-dimensional (3D) crumpled structure, and the effect of sheet morphology on electrochemical energy storage performances was studied. In order to prevent restacking of rGO sheets and ensure high specific surface area, crumpled and spherical structure of rGO, and CNT spacer insertion were also studied. Furthermore, we will discuss the fabrication of supercapacitor electrodes with superior performance by using porous rGO/CNT hybrids. Finally, the fabricated 3D porous rGO structure will be combined with platinum nanoparticles and applied as a electrocatalyst showing excellent performance in oxygen reduction reaction (ORR).

Contents

List of Figures

List of Tables

Chapter 1: Research background for the graphene and graphene-based composite materials

1. Graphene: New member of carbon allotropes

The name of graphene originates from a two-dimensional (2D) and sp^2-hybridized carbon sheet. The extended honeycomb structure of graphene can be the primary component of other important allotropes; if it is to be rolled, wrapped or stacked, it becomes 0D fullerenes, 1D nanotubes and 3D graphite. Wide range of π-conjugation in graphene makes outstanding thermal, mechanical, and electrical properties, which have long been the focus of much theoretical research and has recently become an interesting field for real experiments. Although studies on graphite included those who used fewer and fewer layers for a while,[1] single-layer graphene from graphite was firstly exfoliated by Geim and Novoselov in 2004. (Figure 1).[2]

1.2. Characteristics of graphene

1.2.1. Electronic properties

Atomic orbitals each carbon of s, p_x and p_y in graphene constitute sp^2 hybridization form three strong σ bonds with three surrounding atoms. An overlap of the remaining p_z orbital on each carbon atom with neighboring carbon atoms produces a filled band of p orbitals, called the valence band, and empty band of π* orbitals known as the conduction band. The valence and conduction bands touch at Brillouin zone corners, thus making graphene a zero-bandgap semiconductor. Figure 2 shows the energy spectrum of graphene and a zoomed-in view of the energy bands at one of the Dirac points (at the K or K' points in Brillouin zone or the intersection of the valence and conduction band).[3]

Graphene has been shown to exhibit a pronounced ambipolar electric field effect (Figure 3) such that charge carriers can be adjusted continuously between electrons to holes in concentrations *n* as high as 10^{13} cm^{-2} and their mobility can exceed 10,000 cm^2/Vs and is practically temperature independent.[2] This turns into ballistic transport on submicron scales. The room-temperature mobility is limited by impurities or corrugations of the graphene surface, which means that it can still be improved significantly, perhaps up to 10,000 cm^2/Vs. Among the most spectacular phenomena found in graphene so far is new quantum Hall effects (QHE). Figure 4 shows the QHE behavior observed in graphene. QHE in single layer graphene shows up as an uninterrupted ladder of equidistant steps in Hall conductivity, which persists through the neutrality (Dirac) point, where charge carriers change from electrons to holes.

1.2.2. Mechanical properties

The original graphene structure represents a 2D flat sheet of covalently bonded carbon atoms forming an ideal hexagonal crystal lattice. Graphene samples are usually in existence as single layer

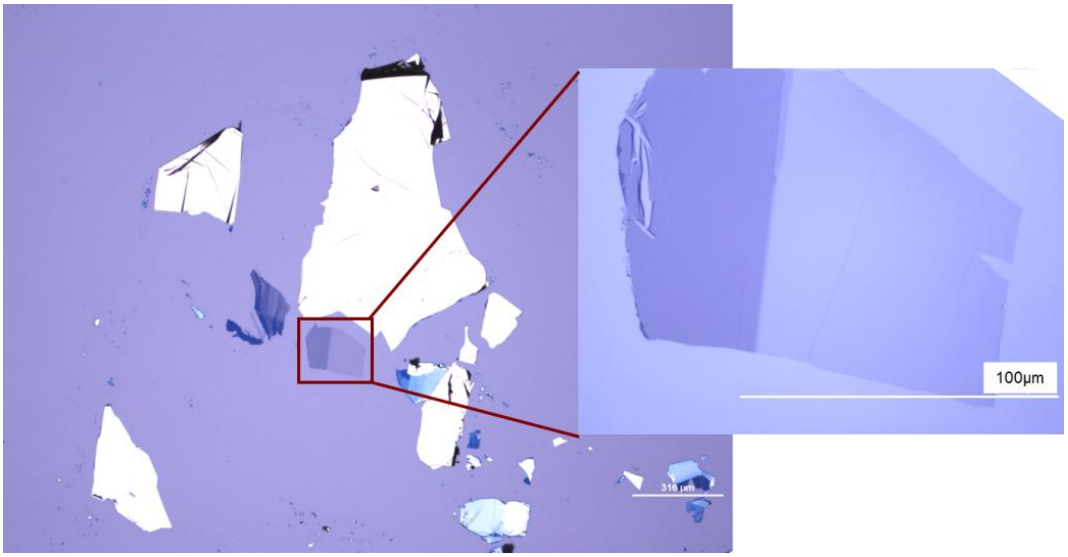

Figure 1. Optical image of the exfoliated graphene layers on 290 nm SiO_2/Si wafers and enlarged view of single layer region, shown as inset.

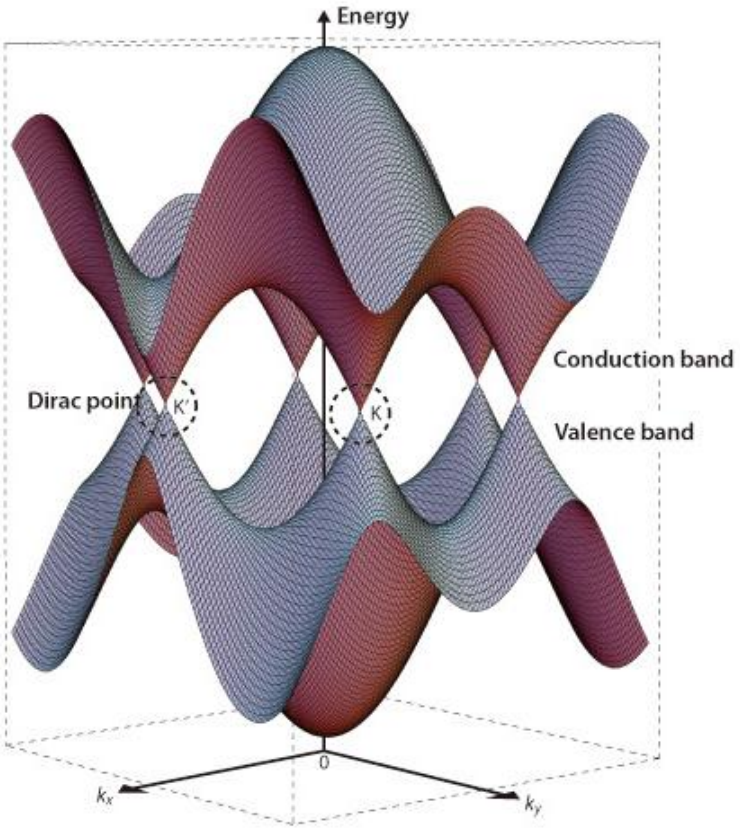

Figure 2. Energy bands near the Fermi level in graphene. The conduction and valence bands cross at points K and K′.

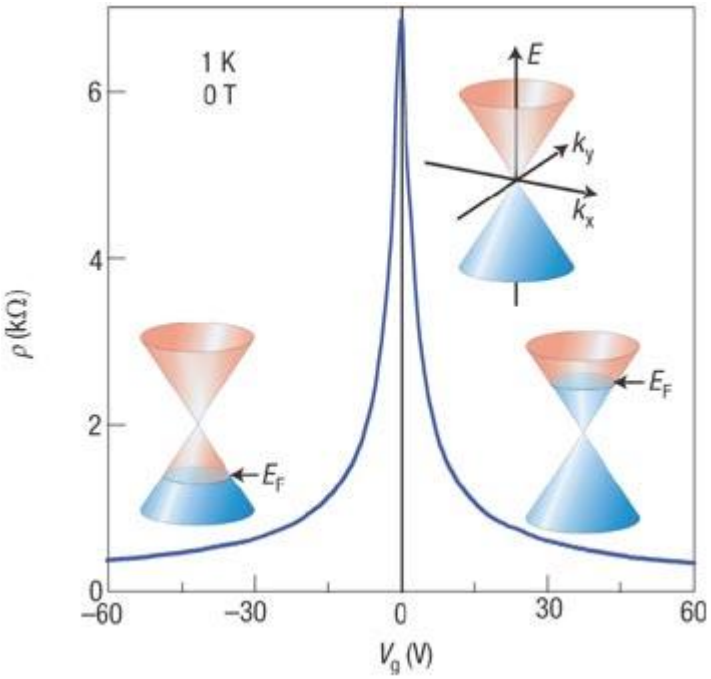

Figure 3. Ambipolar electric field effect in single-layer graphene. The insets show its low-energy spectrum, indicating changes in the position of the Fermi energy E_F with varying gate voltage V_g.

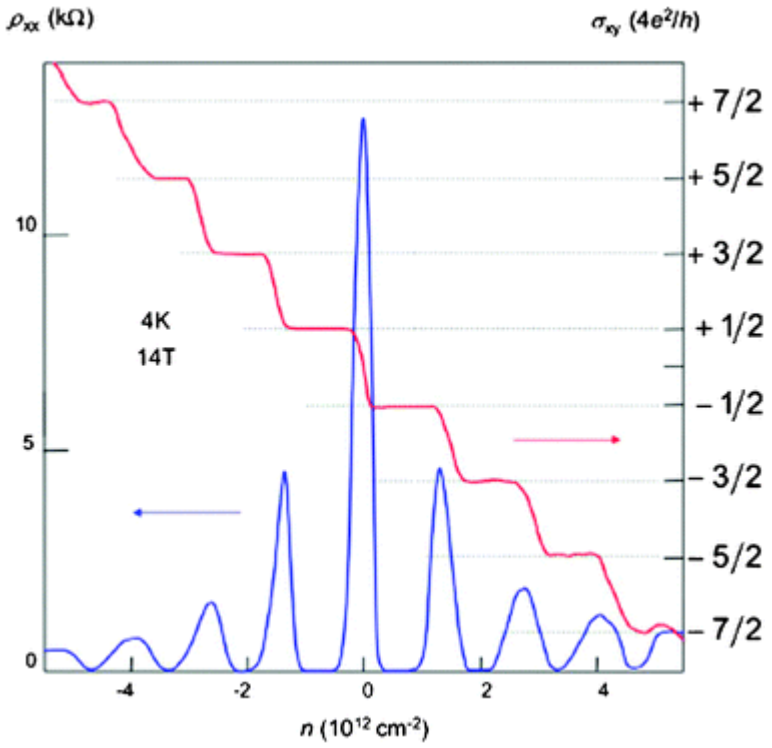

Figure 4. Quantum Hall effect in graphene as a function of charge-carrier concentration. The peak at n = 0 shows that in high magnetic fields there appears a Landau level at zero energy where no states exist in zero field. The field draws electronic states for this level from both conduction and valence bands. The dashed lines indicate plateaus in σ_{xy}.

attached to substrates made of another material such as metal and SiO_2, or free-standing sheets. The term "free-standing graphene" means that a graphene sheet is sufficiently isolated from its environment. Generally, characteristics of its pristine crystal lattice and structural defects like dislocations and grain boundaries inherently have a great influence on mechanical properties of a crystalline solid.[4-5] For example, atom-atom interactions in the ideal, defect-free crystal lattice as well as lattice geometry cause elastic properties of a solid, whereas its strength and plastic flow stress are also strongly affected by characteristics of defects. The pre-existent defects dramatically decrease strength of real solids under mechanical load, compared to the ideal strength inherent to their counterparts free from defects. Structural defects are always present in conventional macroscale solids, and thereby their crucial influence on mechanical properties of these solids is inevitable. In nanoscale solids, however, defects can be absent in the initial, non-deformed state due to nanoscale and free-surface effects, and therefore such solids can exhibit superior strength close to its ideal highest value.[6] In particular, it is the case of comparatively small graphene sheets/membranes that can be fabricated in their pristine, defect-free state. The first systematic experimental analysis of elastic properties and strength exhibited by pristine graphene has been done by Lee with co-workers.[7] In this experiment, a graphene membrane was mechanically deposited onto a substrate with arrays of circular wells and loaded by tip of atomic force microscope (AFM). It was experimentally found that the graphene shows both non-linear elastic behavior and brittle fracture. According to the experiment, graphene is characterized by Young modulus of ~1.0 TPa which is extremely large and close to that specifying carbon nanotubes. Brittle fracture of graphene occurs at a critical stress equal to its intrinsic strength of ~130 GPa. This value is highest ever measured for real materials. The discussed experimental data on the Young modulus (1 TPa) and the intrinsic strength (130 GPa) exhibited by pristine graphene are consistent with computer simulations showing values of E = 1.05 TPa. These values are extremely large and make graphene to be very attractive for structural and other applications. At the same time, graphene can be easily bent, and this is also its specific behavioral feature that can be exploited in practice. Crystallographic characteristics of crack growth in monolayer graphene have been examined in both experiment and molecular dynamics simulations. It was experimentally revealed that cracks or, in other terms, tears are generated and grow in suspended monolayer graphene membranes under unavoidable mechanically applied stress during their processing. In doing so, tears grow predominantly along straight lines in either the armchair or zigzag directions of the hexagonal crystal lattice of graphene occasionally changing growth direction by 30^o. In addition, tears generated under mechanical load in suspended graphene membranes sometimes can grow under electron beam. Kim and coworkers treat this growth process to be driven by a combination of high local stresses concentrated near tear tips and ionization effects of electron beam. In this situation, simultaneously strained and electron-beam excited atomic bonds break in the vicinities of tear tips, providing the experimentally observed tear propagation. Following the computer simulations, the tearing

mechanism represents growth of tears along a dominant armchair direction of the hexagonal crystal lattice of graphene with occasional changes providing rarely distributed small zigzag ledges at the armchair tear edges. This crystallography of tear growth leads to the tapered geometry of the resultant graphene ribbons with low tear angles. In the case of comparatively high adhesion strengths, changes of tear growth direction by 60 ^{o} come into play. The tearing mechanisms under consideration are well consistent with the corresponding experimental data.

1.2.3. Optical properties

The optical transmittance (T) and reflectance (R) are $T= (1 + 1/2\pi\alpha)^{-2}$ and $R=1/4^2\pi\alpha^2T$ for normal incidence light (where $\alpha=2\pi e^2/hc \approx 1/137$, e is the electron charge, c the light speed, and h Planck's constant); the opacity is $(1-T) \approx \pi\alpha \approx 2.3\%$. The expression of T and R in terms of fundamental constants that do not directly involve material parameters is stated to be a result of the structure and electronic properties of graphene. As shown in Figure 5 (a), this constant transparency ($\sim$97.7%) has been experimentally observed for graphene in the visible range and the transmittance linearly decreases with the number of layers for n-layer graphene. Interband optical transitions in graphene have been probed by infrared spectroscopy, and gate-dependent optical transitions have been reported. Due to the low density of states near the Dirac point in graphene, a shift of the Fermi level due to the gate causes a significant variation of charge density, leading to a significant change in transmission.

Given the low throughput of AFM, STM, TEM, and methods for characterizing the transport properties of graphene, other methods are needed to rapidly locate graphene, to identify its morphology and quality and to distinguish the number of layers (n) in n-layer graphene. The optical contrast of graphene on various substrates has been studied. The insulator layer thicknesses employed for the observation of graphene on SiO_2/Si wafer. The contrast of graphene on substrates is dependent on the wavelength and the incident angle of the illumination. The thickness of n-layer graphene with less than 10 layers has been determined using white light illumination on samples supported on a 285 nm SiO_2/Si substrate (Figure 5 (b)).[8] The refractive index of monolayer graphene was obtained as $n=2.0-1.1i$ in the visible range,[8] slightly different from that of bulk graphite $n=2.6-1.3i$.[9] Another study argued that the complex refractive index of graphene and graphite could be generally expressed as $n=3-iC/(3\lambda)$ (where C = 5.446 μm^{-1} and λ is wavelength), by fitting to experimental spectra as a function of wavelength.

1.2.4. Thermal properties

The first experimental studies of the thermal conductivity (K) of graphene were carried out by using Raman spectroscopy. The optothermal Raman measurements were performed with large-area suspended graphene layers exfoliated from high quality HOPG. The researchers found K exceeding ~3,000 W/mK near room temperature, that is, above the bulk graphite limit, observed K

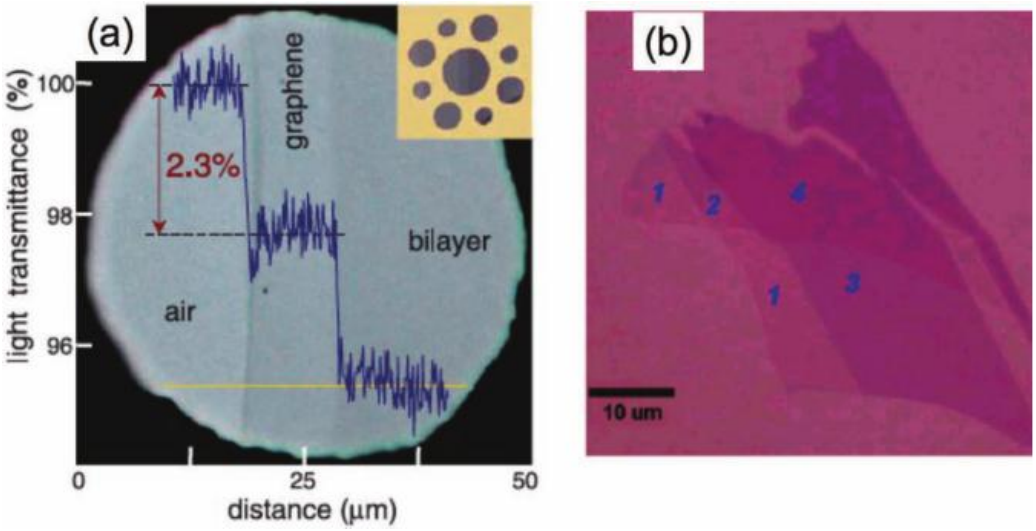

Figure 5. (a) Photograph of a 50 μm aperture partially covered by graphene and its bilayer. The line scan profile shows the intensity of transmitted white light along the yellow line. Inset shows the sample design: a 20 μm thick metal support structure has apertures 20, 30, and 50 μm in diameter with graphene flakes deposited over them; (b) Optical image of graphene flakes with one, two, three, and four layers on a 285 nm SiO_2/Si substrate.

dependence on the layer size and determined that $K_e << K_p$. The phonon mean-free path was estimated to be ~775 nm near room temperature. A following independent study also used the Raman technique, but modified it by addition of a power meter under the suspended portion of graphene. It was found that the K of suspended high-quality graphene prepared by CVD exceeded ~2,500 W/mK at 350 K, and it was as high as ~1,400 W/mK at 500 K (experimental uncertainty ~40%). The reported value is larger than the K of bulk graphite at room temperature. Another group repeated the optothermal Raman measurements found $K \approx 630$ W/mK for suspended graphene at $T \approx 600$ K.[10] Other optothermal studies with suspended graphene found K in the range from ~1,500 to ~5,000 W/mK.[11] The data for suspended or partially suspended graphene is closer to the intrinsic K because suspension reduces thermal coupling to the substrate and scattering on the substrate defects and impurities. For practical applications, it is important to know the K of supported graphene, that is, graphene attached to the substrate along its entire length. The measurements for exfoliated graphene on SiO_2/Si revealed an in-plane K of ~600 W/mK near room temperature. This value is below those reported for suspended graphene, but it is still rather high, exceeding the K of Si (145 W/mK) and Cu (400 W/mK). They attributed the reduced experimental value to graphene–substrate coupling and phonon leaking across the interface.[12]

1.3. Synthetic methods of grpahene

As mentioned above, graphene was first exfoliated from bulk graphite using ‘Scotch tape method’ in 2004. After that, many research groups have developed exfoliation methods and growth methods.

1.3.1. Mechanically exfoliated graphene from graphite

The exfoliated graphene was first achieved by mechanical exfoliation.[2, 13] As is the case of most scientific discoveries, graphene was discovered by accident and surprisingly atomic scale thin layer graphene samples were observed by optical microscope.[2] The key for the success probably was the use of high throughput visual recognition of graphene on a proper chosen substrate, which provides a small but distinguished optical contrast. The graphene sheet made by mechanical exfoliation shows the highest crystallinity and the lowest degree of defects among the graphene samples made until now and therefore it is appropriate for studies about the physical and chemical properties of graphene. However, trained eyes are required for identification of single-layer graphene.

1.3.2. Chemically exfoliated graphene in liquid

Another approach to produce mass production of graphene is chemical exfoliation. The bulk graphite can be dispersed in organic solvent into single layer of graphene. N-methylpyrrolidone (NMP), N,N-dimethylacetamide (DMA), γ-butyrolactone (GBL) and 1,3-dimethyl-2-imidazolidinone (DMI) have been utilized as a dispersion solvent. Recently, o-dichlorobenzene was reported as the

best solvent for dispersion of graphene with simple sonication method.[14-15]

1.3.3. Growth of graphene by chemical vapor deposition (CVD)

Graphene can be grown on metal surfaces by surface segregation of carbon or by decomposition of hydrocarbons. However, this technique is only practical for graphene production if the as-grown graphene can be transferred from the metal substrates to other substrates, which looks straight-forward but only was realized for multilayer and non-uniform films with Ni,[16-18] and for uniform monolayer graphene, with Cu.[19] In contrast to the use of high-cost single crystal metals and UHV systems in previous work by the surface science community, few-layer graphene films were grown on polycrystalline Ni foils by CVD of methane under atmospheric pressure by controlling the cooling rate of the metal substrates so as to suppress carbon precipitation during cool-down.[20] Few-layer graphene films were also grown on thin Ni films from which the amount of precipitated C was also suppressed.[17-18] However, because the solubility of C in Ni is relatively high, it has to date been difficult to suppress C precipitation completely so that the produced graphene films vary from monolayer to tens of layers. Instead, large-area films with > 95% as monolayer graphene were grown on Cu foils by CVD of methane by taking advantage of the very low solubility of C in Cu.[19] By using ^{13}C labeling, it was shown that graphene growth on Cu is a surface-mediated process and the process is self-limiting. That is, once the Cu surface was fully covered with graphene, the growth process terminated, and it was also possible to achieve 100% monolayer coverage.[21] Graphene grown on metal substrates also shows high quality with extracted carrier mobility typically in the range 2,000 to 4,000 cm^2/Vs. These values are lower than values for those from particular graphene flakes made by mechanical exfoliation of graphite. Improvement of quality of the CVD grown graphene in terms of synthesis, and also in terms of transfer to arbitrary substrates, is desirable.

1.3.4. Epitaxial growth of graphene

This method involves CVD growth on epitaxially matched metal surfaces. John May explained in an article published in Surface Science in 1969 how published but unassigned low-energy electron diffraction (LEED) patterns could be rationalized in terms of a monolayer of graphite.[22] Blakely and his group undertook detailed scientific studies of the thermodynamics of growth of 'monolayer graphite' and of 'bilayer graphite' on Ni (111) crystals, publishing a series of insightful papers in the 1970s,[23-26] and a 'sub-discipline' of surface science developed on the topic 'monolayer graphite' or 'MG', that continues to this day (surface scientists now typically refer to the MG they grow as graphene). A more recent thrust in terms of growth of epitaxial graphene, is its large-area growth on SiC wafer surfaces by high temperature (up to 1,300 ^oC) evaporation of Si in either UHV[27-29] or atmospheric pressure as a method to prepare wafer-size graphene with carrier mobility values of about 2,000 cm^2/Vs.[30] Atomically resolved STM has been used to study the bottom-up formation of

graphene on the single crystal SiC surface.[31] Large area and monolayer of graphene has been achieved on Cu films,[19, 21, 32] and this method can be in principle extended to endless length and very large width production simply by exposing appropriate metal foils to C to achieve surface deposition of either monolayer or multilayer. It is of interest that epitaxial growth has not yet been proven for growth on Cu, and so this might eventually be classified as another method for growth of graphene such as non-epi growth. This category might end up including the possibility of growth from (or on) molten metals and amorphous metal substrates. Direct growth of graphene on metal oxide surfaces is an exciting challenge that could benefit, *e.g.*, nanoelectronics.

2. Graphene oxide (GO)

Chemical modification of graphene, which is mainly generated from graphite oxide has been a promising route to achieve mass production of chemically modified graphene (CMG) platelets. Graphene oxide contains a range of reactive oxygen functional groups, which renders it a good candidate for use in various applications through chemical functionalization.

2.1. Chemical structure of GO

Many of the earliest structural models of GO proposed regular lattices composed of discrete repeat units. Hofmann and Holst's structure (Figure 6) consisted of epoxy groups spread across the basal planes of graphite, with a net molecular formula of C_2O.[33] Ruess proposed a variation of this model in 1946 which incorporated hydroxyl groups into the basal plane, accounting for the hydrogen content of GO.[34] Ruess's model also altered the basal plane structure to an sp^3 hybridized system, rather than the sp^2 hybridized model of Hofmann and Holst. The Ruess model still assumed a repeat unit, however, where the first quarter (1/4) of the cyclohexanes contained epoxides in the 1,3 positions and were hydroxylated in the 4 position, forming a regular lattice structure. This was supported by Mermoux based on observed structural similarities to poly(carbon monofluoride), $(CF)_n$,[35] a structure that entails the formation of C–F bonds through the complete rehybridization of the sp^2 planes in graphite to sp^3 cyclohexyl structures.[36] In 1969, Scholz and Boehm suggested a model that completely removed the epoxide and ether groups, substituting regular quinoidal species in a corrugated backbone.[37] Another remarkable model by Nakajima and Matsuo relied on the assumption of a lattice framework akin to poly(dicarbon monofluoride), $(C_2F)n$, which forms a stage 2 graphite intercalation compound (GIC).[38] These individuals also made a valuable contribution to understanding the chemical nature of GO by proposing a stepwise mechanism for its formation via three of the more common oxidation protocols. Certainly, the most well-known model is the one by Lerf and Klinowski (Figure 7(a)). Anton Lerf and Jacek Klinowski have published several papers on the structure and hydration behavior of GO, and these are the most widely cited in the contemporary literature. The initial studies done by Lerf and coworkers used solid state nuclear magnetic resonance (NMR) spectroscopy to characterize the

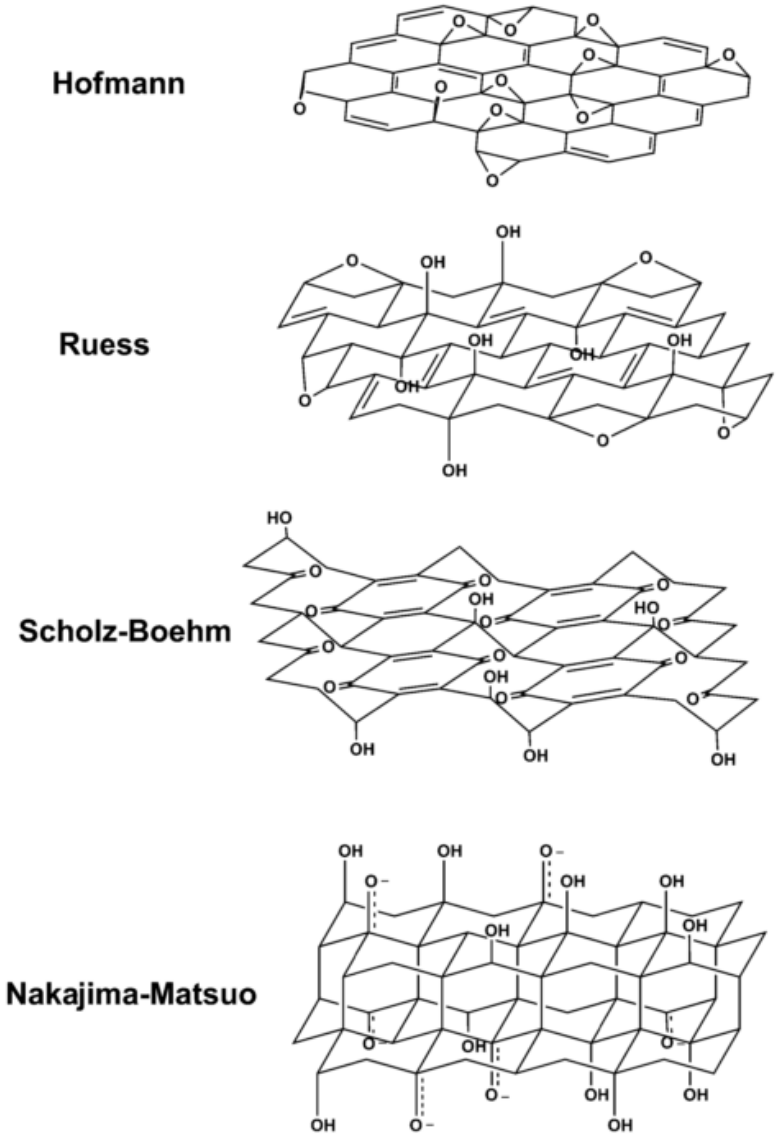

Figure 6. Summary of proposed structural models of GO.

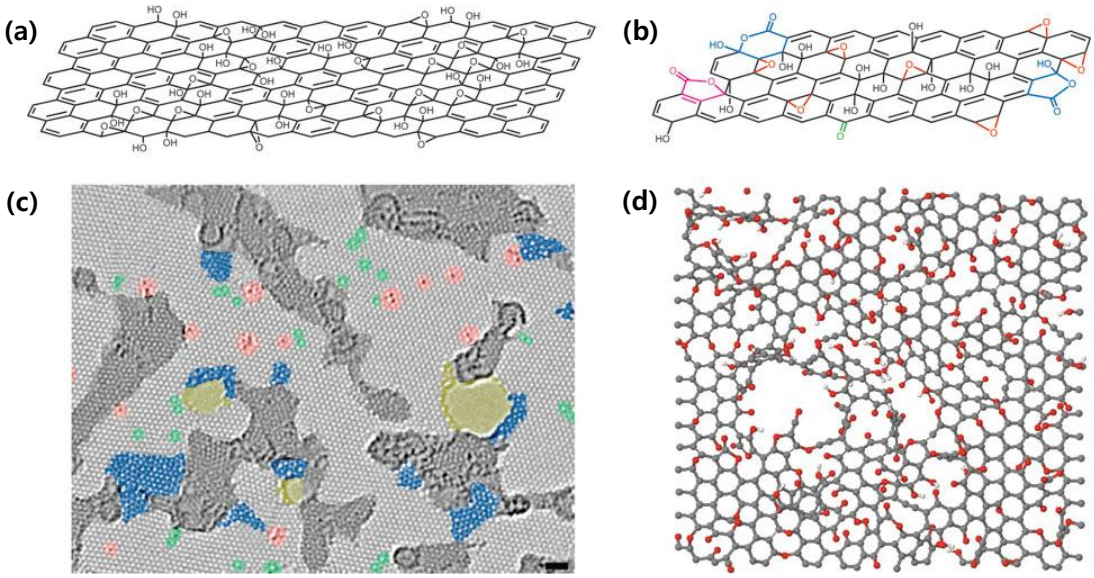

Figure 7. (a) The chemical structure of a single sheet of GO according to the Lerf–Klinowski model, (b) an updated chemical structure proposed by Gao and colleagues, (c) atomic resolution, aberration-corrected high-resolution transmission electron micrograph of a single-layer rGO sheet, and (d) atomic model schematically illustrating disordered rGO basal plane consisting of holes, topological defects and remnants of oxygen groups.

material.[39] This was a first for the field as earlier models relied primarily on elemental composition, reactivity and X-ray diffraction studies. By preparing a series of GO derivatives, Lerf was also able to isolate structural features based on the material's reactivity.[40]

While the studies mentioned above outlined many of the fundamental structural features of GO, a more refined picture of the complexity of the material was necessary. Lerf and coworkers proceeded by reacting GO with a range of reactive species.[40] They determined that the double bonds were likely either aromatic or conjugated, the logic being that isolated double bonds would be unlikely to persist in the strong oxidizing conditions used as known as a modified Hummers method. This revised Lerf-Klinowski model also incorporated the infrared spectroscopic data from decades earlier indicating that carboxylic acid groups were present in very low quantities at the periphery of the graphitic platelets, in addition to other keto groups.[37, 41] More recently, many people have reported on the structure of the GO, and the TEM analysis and computational simulations allow us to visualize more accurate structural models GO and reduced graphene oxide (rGO) as shown in Figure 7.

2.2. Synthetic methods of GO and reduced graphene oxide (rGO)

Comprehensive reviews on the preparation of dispersions of graphene oxide platelets and reduced graphene oxide platelets, made from GO, have recently appeared. In general, GO is synthesized by either the Brodie,[42] Staudenmaier,[43] or Hummers method,[44] or some variation of these methods. All methods involve oxidation of graphite to various levels. Brodie and Staudenmaier used a combination of potassium chlorate ($KClO_3$) with nitric acid (HNO_3) to oxidize graphite, and the Hummers method involves treatment of graphite with potassium permanganate ($KMnO_4$) and sulfuric acid (H_2SO_4). Graphite salts made by intercalating graphite with strong acids such as H_2SO_4 , HNO_3 or $HClO_4$ have also been used as precursors for the subsequent oxidation to GO.[45] The polar oxygen functional groups of GO render it hydrophilic, therefore, GO can be exfoliated in many solvents, and disperses particularly well in water.[46] Dispersions of graphene oxide platelets can be obtained by stirring and more typically by sonication of GO in solvents.

Chemical reduction of the colloidal dispersions obtained has been performed with several reducing agents, such as them hydrazine, hydroquinone, sodium borohydride ($NaBH_4$), and ascorbic acid. Reduction via thermal treatment has been reported to be an efficient and low cost method, producing 'TEGO' material with a BET surface area of 600–900 m^2/g. Electrochemical reduction has been presented as an effective way to remove oxygen functional groups from GO. Chemical reduction using $NaBH_4$ followed by a H_2SO_4 treatment prior to thermal annealing yielded CMG platelets with high C purity. The detailed chemistry of oxidation, reduction, and the chemical tuning of graphene platelets is still an active area of research that should continue to rapidly grow.

3. Recent progress in GO-based composite materials and its applications

3.1. GO-reinforced polymer composite materials

GO-based fillers have been used in polymer nanocomposites and hold potential for a variety of possible applications.[47] GO and rGO can be used as precursors to bulk scale production of an assortment of exfoliated chemically converted graphene for use as a filler.[14] GO-based polymer composites, including polystyrene (PS), PMMA, polyvinyl alcohol (PVA), polyacrylic acid (PAA), polypropylene (PP), epoxy, polyester, silicone foam, polyurethane, poly(vinyldiene fluoride), and polycarbonate, were successfully fabricated. To achieve large property enhancements in their nanocomposites, layered structure of GO must be exfoliated and well dispersed in the polymer matrix. Among other methods, as well as ultrasonication of GO have been used extensively to produce highly-exfoliated platelets for nanocomposites.[14, 48] Notably, thermally-expanded GO (TEGO) is reduced and can be used to make electrically conductive composites, whereas mechanically-exfoliated GO retains its insulating chemical structure. These fillers can be dispersed into polymers using techniques such as solution mixing, melt blending, or in situ polymerization. One of these methods, in situ polymerization might offer superior dispersion of this filler. Polymer nanocomposites with GO-derived materials as filler have shown dramatic improvements in properties such as elastic modulus, tensile strength, electrical conductivity, and thermal stability. Moreover, these improvements are often observed at low loadings of filler evidently due to the large interfacial area and high aspect ratio of these materials, requiring small amounts of filler to achieve percolation. At 0.7 wt% loading, a solution-mixed PVA/GO nanocomposite showed a 76 % increase in tensile strength and a 62 % increase in Young's modulus; the results were attributed to effective load transfer to the GO filler via interfacial hydrogen bonding.[49] Chemical reduction of graphene oxide in the presence of PVA generated conductive composites with a percolation threshold below 1 wt% and produced large shifts in glass transition temperature (T_g).[50] Large increases in Young's modulus and a 30 ^oC shift in T_g at only 0.05 wt% loading of a PMMA/TEGO composite were attributed to the onset of rheological percolation and to the crumpled morphology of the highly exfoliated platelets.[51] Nanocomposites of platelets derived from TEGO have shown higher stiffness across all loadings and equal or lower electrical percolation thresholds than carbon black and nanotube-filled nanocomposites.[52] Low loadings of exfoliated GO platelets in epoxy reduced the coefficient of thermal expansion (up to 32% at 5 wt%) and increased the critical buckling strength (by 52% at 0.1 wt%) versus the neat polymer.[53-54] Covalent functionalization of GO has been used in an effort to compatibilize the filler with polymer hosts for improved dispersion. For instance, isocyanate-functionalized GO was mixed with PS in a solution, and subsequent reduction yielded conductive nanocomposites with an onset of electrical percolation at 0.1 vol%, consistent with some of the lowest thresholds reported, *e.g.,* for CNT nanocomposites.[55] GO was also functionalized with PVA via ester linkages, yielding composites with

well dispersed GO sheets that showed a 20 °C shift in T_g.[56] Silane-functionalized rGO resulted in a 35 % improvement over unmodified EG-epoxy nanocomposites.[57] Covalent grafting of PS microspheres to reduced graphene oxide has been reported using emulsion polymerization.[58] Grafted polymers dramatically improved the solubility of graphene oxide in organic solvents,[59] while nanocomposites of PS-grafted GO in a PS matrix demonstrated substantial mechanical property enhancements (57% increase in modulus and 70% increase in strength at 0.9 wt%).[60] Novel synthesis and processing methods have produced GO-based nanocomposites with large property improvements, unique structures, and some of the lowest percolation thresholds reported to date. For example, layer-by-layer assembly created conductive PAA/GO nanocomposites, and was doubling the modulus versus the neat polymer.[61] A simple method of coating polymer powder with rGO prior to melt blending resulted in a dramatic reduction in the percolation threshold of a PP nanocomposite from 7 wt% to 0.1 wt%,[62] while a 'reduction-extractive' dispersion technique yielded conductive reduced graphene oxide-vinyl acetate/vinyl chloride copolymer nanocomposites with a percolation threshold of 0.15 vol%.[63] Aqueous solutions of polymers and GO were frozen and freeze-dried to produce nanocomposite monoliths with a 3D, porous scaffold-like structure that might also find potential applications in electronics and as catalyst supports.[64] As mentioned above, although a myriad of studies have been conducted, GO-based composite materials are still regarded as the most suitable field for practical applications of graphene.

3.2. GO/carbon nanotube (CNT) hybrid materials

Composites made of only using carbon-based materials including graphene, GO, rGO and CNT, *etc.*, are mainly referred to as "hybrid materials" rather than "composites materials" in most literatures. Owing to its unique optical, electrical and mechanical properties, graphene has emerged as a new class of promisingly attractive materials for various applications. In recent years, combinations of one-dimensional (1D) carbon nanotubes (CNT) and two-dimensional (2D) GO sheets to form flexible three-dimensional (3D) GO/CNT hybrid materials have attracted great attention owing to their intriguing properties. The synergistic effects of these tw0o carbon-based materials improve the electrical, optical, electrochemical, and mechanical properties. GO/CNT hybrid materials have an interconnected network of carbon structures with a synergistic effect in enhanced conductivity. Thus, they are suitable for a variety of applications, such as such as transparent electrodes, optoelectronics, field effect transistors, energy storage materials, biosensors, and composites.

Various techniques have been employed for fabricating GO/CNT hybrid materials, including layer-by-layer (LBL) assembly and hybridization between CNT networks and GO sheets (Figure 8 (a)). Early fabrication methods for LBL assembly are the wet processing of CNT and GO sheets and solid-phase layer stacking of CNT networks on a graphene film.[65] The LBL process involves the assembly of oppositely charged interaction between GO and CNT in dispersions with or without surface

functionalization of CNT. The function of CNT not only provides the electronic conductivity, but also affords mechanical flexibility for the hybrid film, while allowing for electronic contact among GO sheets by bridging their gaps.[66] The sheet resistance and optical transmittance of the as-prepared hybrid film reach 400 Ω/sq and 84 %, respectively. These results suggest a great potential for fabricating high-performance transparent conductors. However, this approach usually produces 2D structures morphologies, and thus it limits the practical applications. Other approaches have been developed to construct 3D hybrid architectures to engineer the number layers of graphene for satisfying the requirements of a specific application such as transparent conductive electrodes.[65-67] Clearly, all the mentioned methods involve difficultly in constructing covalent C-C bonding between graphene layers and CNT in the hybrids, which can significantly limit performance in practical applications. Therefore, recent attention has been focused on efficient methods for fabricating graphene/CNT hybrid that provide covalent C-C bonding between graphene layers. One of the most direct and simple ideas is the growth of CNT on GO surfaces by CVD processing.

CVD is the most promising method that directly grows CNT and graphene on a substrate surface. Thus, it will greatly facilitate the fabrication of all carbon-based nanomaterials. The CVD process is a catalytic conversion of a gaseous precursor at high temperatures into a solid material at the surface of catalyst particles. In this method, large area graphene films are usually produced by deposition of GO platelets in aqueous colloidal suspensions, followed by decorating the platelets with metal catalyst nanoparticles. Then, CNT growth is promoted by segregating the nanoparticles on various spin-coated substrates during the CVD process. The major advantages of CVD methods are efficiency, directness and the ability to produce all carbon-based devices. Therefore, fabrication of rGO/CNT hybrids has mostly employed these methods. Obviously, tremendous efforts have been devoted in recent years to integrate individual CNT into dimensionality of sp^2-hybridized carbon nanostructures to achieve different configurations of graphene/CNT hybrid nanostructures. More recently, Tour *et al.* demonstrated that graphene and CNT are overlapped via π–π stacking rather than covalent welding, resulting in good planar graphene/CNT hybrids (termed as "rebar graphene").[68-69] The CNT act as reinforcing bar (rebar) and graphene is toughened through both π-π stacking domains and covalent bonding where the CNT partially unzip and form a seamless 2D hybrid material (Figure 8 (b)). This type of hybrid possesses a transmittance of 95.8 % at 550 nm and a sheet resistance of 600 Ω/sq, indicating better performance than those of stacked CVD bilayer graphene or CNT films at the same transmittance.

As-mentioned above, rGO/CNT hybrid materials have been utilized for various applications not only transparent conductors but also electron field emitters, field-effect transistors, sensors, and especially supercapacitors. Due to their high surface area, conductivity, electrochemical stability, and mechanical stability, rGO/CNT hybrid materials are considered as an attractive material for supercapacitor electrode. Kim *et al.* fabricated supercapacitors based on rGO/CNT hybrid film and its

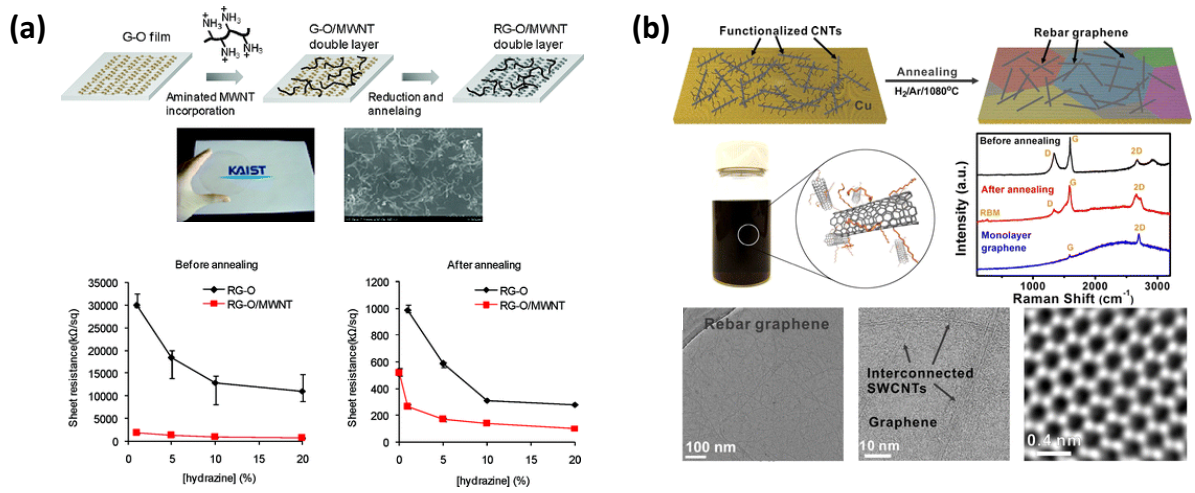

Figure 7. (a) Layer-by-layer assembled rGO/CNT for transparent electrode and (b) CNT-reinforced graphene (a.k.a. “Rebar graphene”) by simply annealing functionalized CNT.

capacitance was 653.7 μF/cm^2 at 10 mV/s, which is considerably higher than the value of 99.6 μF/cm^2 at 10 mV/s for graphene electrodes, indicating potential feasibility of rGO/CNT electrode for supercapacitor with greater capacitance than that of graphene electrodes.[70] Cui and co-workers fabricated supercapacitors based on rGO/CNT hybrid materials. Compared with rGO in both positive and negative potential windows, the galvanostatic charge/discharge curves of rGO/CNT electrodes showed more symmetric and triangular shapes.[71] These rGO/CNT electrodes showed the higher specific capacitance as compared to rGO. Introducing a small amount of CNT into rGO sheets, the capacitance of rGO/CNT hybrid showed a negative potential window with 237 F/g, which was about twice that of rGO only (95 F/g) at the scan rate of 50 mV/s. An increasing the amount of CNT can significantly enhance the capability and cyclic stability rates of the electrode. To this day, rGO/CNT-based supercapacitors still have been demonstrated as promising candidates for use in hybrid vehicles and electrical vehicles.

3.3. rGO-supported Pt catalysts for oxygen reduction reaction

Many attempts are just beginning to understand the wide range of capabilities that can be achieved by carefully designed and integrated graphene-based materials. The application potential towards two important electrochemical devices that rely on oxygen reduction: polymer electrolyte fuel cells (PEFC) and metal–air batteries, is undergoing intensive development with marked progress realized in recent years. The ability to understand and manipulate the properties of graphene and its composites may hold the key to revolutionizing the performance capabilities of these modern clean energy technologies.

Because of the highly graphitic features of graphene that can ideally provide resistivity to carbon corrosion during fuel cell operation, the basal plane surfaces are not favorable for interaction with platinum species. This can make it difficult to deposit well-dispersed, uniform size nanoparticles, and instead commonly results in agglomerate platinum structures or nanoparticle deposition restricted to edge sites. This is analogous to the well-established properties and surface interactions of carbon nanotubes (CNT). In order to achieve excellent platinum nanoparticle dispersion, other researches have used GO during the deposition step. GO has a high concentration of surface functional species that ideally make it readily dispersed in a large number of solvents and allow for suitable interactions with catalyst precursor species.[46] Conversely, these surface species cause interruptions in the graphitic structure and lead to very poor electronic conductivity. Through this approach, however, platinum nanoparticles and GO can be simultaneously reduced using chemical treatments (*i.e.,* with $NaBH_4$) or solvothermal processes. Interestingly, it also appears that using a thermal treatment to simultaneously exfoliate and reduce GO will result in rGO with surface properties that are favorable to the deposition of well dispersed platinum nanoparticles.

One difficulty in exclusively elucidating support effects in graphene-based catalysts is in that the

specific synthetic techniques employed will have a large impact on the size and morphology of the nanoparticles.[72] These parameters are well known to play a role in governing ORR activity and serve to confound direct ORR activity comparisons between different catalyst supports. To avoid these influences, Guo *et al.* separately prepared 7 nm diameter polyhedral platinum-iron nanoparticles with controlled size and morphology.[73] The nanoparticles were then deposited on rGO (obtained by reduction of GO by refluxing in DMF) or carbon black by a solution phase self-assembly. In this regard, the platinum–iron particles dispersed on rGO showed an improvement in ORR activity in 0.1 M HClO4 in comparison to both the carbon supported particles prepared as comparison and commercial Pt/C. In addition to excellent electrochemical stability (after 10,000 cycles from 0.4 to 0.8 V vs. Ag/AgCl at 100 mV/s), the rGO supported catalyst showed much higher double layer capacitance in the cyclic voltammetry (CV) profile. This is commonly reported when using graphene-based catalyst supports and highlights the fact that graphene can provide higher electrochemically accessible surface areas than conventional supports.

A well-recognized issue with graphene materials is its tendency to restack through the strong π-π surface interactions, even when Pt nanoparticles are present on the surface. Xin *et al.* demonstrated that using freeze drying to collect rGO/Pt catalyst samples can allow them to be easily re-dispersed in catalyst inks.[74] However, freeze drying may not be a feasible process for preparing fuel cell electrodes that require the deposition of a catalyst ink onto an electrolyte membrane or gas diffusion layer, followed by solvent removal. In this regard, restacking of rGO-based catalysts will result in oxygen inaccessibility through the entire catalyst layer and issues with the removal of produced water. Li *et al.* investigated this effect during ring disk electrode (RDE) preparation and devised a procedure to prevent graphene agglomeration.[75] By mixing rGO/Pt catalyst with carbon black, they showed improved ORR performance because of pores generated by carbon black. Particularly, rGO/Pt did not display a mass transport limitation at electrode potentials below ca. 0.8 V vs. RHE, which is a common feature for high surface area platinum catalysts. With the addition of carbon black into catalyst ink, mass transport limitations were effectively alleviated, although the catalyst did not perform as well as commercial Pt/C. Graphene-based catalysts will likely be faced with mass transport difficulties when incorporated into an electrode structure. Therefore, there is plenty of opportunity for innovative electrocatalyst and electrode engineering strategies to be designed to address these.

Recently, integrating monolayer graphene into macroscopic 3D porous interconnected networks has attracted significant attention, since the non-agglomerated 3D structure can provide graphene-based nanomaterials with high specific surface areas, strong mechanical strengths, and fast mass and electron transport kinetics due to the combination of 3D porous structures and the excellent intrinsic properties of graphene.[76-79] It is a realistic strategy to further maximize the activity of noble metal-based nanostructures and minimize the use of precious noble metal by loading these highly active

nanomaterials on the surface of supporting materials with low cost, high surface area, and good electrical conductivity, which not only maximizes the availability of surface area for electron transfer and decreases the aggregation of these electrocatalysts, but also provides better mass transport of reactants to the electrocatalysts. As expected, 3D graphene network is believed to be the most promising candidate for ORR owing to its unique properties such as high electrical and thermal conductivities, great mechanical strength, inherent flexibility, and huge specific surface area. Zhu and coworkers constructed a hybrid 3D nanocomposite film by alternatively assembling the graphene nanosheets modified by imidazolium salt-based ionic liquid (IS-IL) and Pt nanoparticles through electrostatic interaction.[80] The introduction of IS-IL on the surface of graphene nanosheets not only increases the dissolubility of graphene nanosheets, but also provides the catalyst support with higher conductivity and abundant positive charge desired in this LBL self-assembly of nanocomposites. This multilayer film exhibited prominent electrocatalytic activity and stability toward ORR. Furthermore, the content of Pt NPs and thus the electrocatalytic activity—of the films could be tailored by tuning the number of bilayers in the LBL process. In 2013, Sattayasamitsathit and coworkers reported for the first time on the use of lithographically defined 3D graphene microstructure as support for catalytic metal NPs (Figure 9(a)).[81] Various noble metal NPs (Au, Pd, and Pt) were deposited on these multilayered highly ordered 3D graphene structures by electrochemical method. The size, morphology, and distribution of the NPs over the 3D graphene structure could be tailored by changing the preparation conditions (*e.g.,* deposition potential or time for electrochemical method; metal concentration, pH, or temperature for chemical reduction method). The catalytic activity toward ORR of Pt nanoparticles on 3D graphene was superior to that of Pt NPs on a 3D carbon substrate and on a glassy carbon electrode, bare 3D graphene, and Pt black. This enhancement of catalytic activity could be ascribed to the macroporosity of 3D graphene which allows deposition of a high surface area of catalytic NPs and the nanosize dimensions of the connecting arms and nodes in 3D graphene structure which provides a highly favorable mass transport environment for delivery of fuels.

In spite of significant progress made in this area within only several years, the research of 3D graphene-based materials still remains at its initial stage. the systematic exploration and deeper understanding of the different catalytic mechanisms of various 3D graphene-based materials for ORR are required for optimum material design and device performance optimization, and the development of facile, green, cost-effective, and controllable preparation method is still a significant issue, because the current assembly process usually needs to be carried out in rigorous conditions. Thus, much further research is needed to realize the aim of final industrial implementation, large scale, low cost, and simple production of 3D graphene-based materials with high catalytic activity and practical durability for ORR.

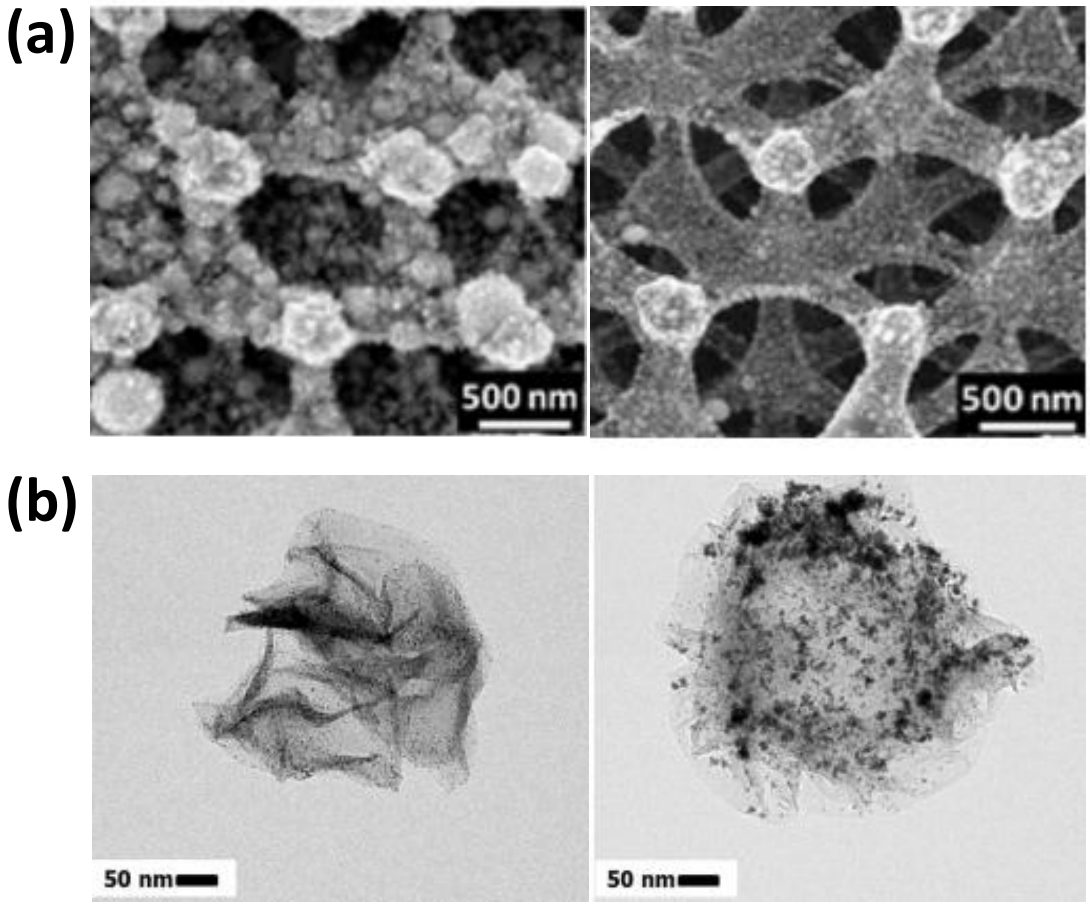

Figure 8. (a) Lithographically defined 3D graphene microstructure and (b) 3D crumpled graphene as support for catalytic metal NPs (Pt and Pt-Au alloy).

4. Poly(dopamine) and its derivative materials combined with GO

4.1. Brief introduction of poly(dopamine)

Adhesion observations on solid surfaces of mussels have led to significant advances in materials science. Mussels are able to be strongly attached to a variety of substrates through high bonding forces even on wet surfaces. It was found that 3,4-dihydroxy-L-phenylalanine (DOPA) and lysine-enriched proteins near the plaque−substrate interface are the major origins of the extra ordinarily robust adhesion.[82] Based on these findings, polydopamine, which has a molecular structure similar to DOPA, attracted attention as a novel coating material in 2007.[83] The main advantage of polydopamine is that it can be easily deposited on all kinds of inorganic and organic substrates, including super hydrophobicity, as seen in mussels.

Poly(dopamine) is also a major pigment of melanin (eumelanin) that can be found in nature. Therefore, poly(dopamine) exhibits many notable characteristics of naturally occurring melanin in optics, electricity, and magnetics, and the most important thing is to have excellent biocompatibility. Another important feature of polydopamine is its chemical structure, which contains many functional groups such as catechol, amine, and imine. These functional groups can serve as an anchor for loading the transition metal ion and the starting point of covalent modification with the desired molecule, which can further realize the appearance of various hybrids due to their strong reducing ability to these metal ions under alkaline conditions. These advantages enable polydopamine to be rapidly integrated into a variety of applications not only coating but also chemical, biological, medical, and materials sciences, as well as in applied science engineering, and the technology fields.

Alternatively, electropolymerization of dopamine monomers has also been used to deposit polydopamine directly on electrodes.[84] This electropolymerization of dopamine can be conducted in deoxygenated solution with cyclic voltammetry within a given potential. In this manner, poly(dopamine) can be coated directly on the electrode with a thicker film thickness as compared to the oxidative polymerization method under the same concentration of the monomer.

Although poly(dopamine) can be made by an easy and simple polymerization process, the molecular mechanism of poly(dopamine) formation has been the subject of scientific disputes for a long time. As illustrated in Figure 10, dopamine is first oxidized to dopamine-quinone followed by intramolecular cyclization via 1,4 Michael-type addition to yield leucodopaminechrome under alkaline conditions. Thereafter, leucodopaminechrome is further subjected to oxidation and rearrangement to form 5,6-dihydroxyindole, which is easily oxidized to 5,6-indolequinone. These two reaction products are able to undergo branching reactions at positions 2, 3, 4, and 7, leading to the formation of multiple isomers of dimers and, in the end, higher oligomers, which self-assemble through the reverse dismutation reaction between catechol and *o*-quinone to give the cross-linked polymer. Preliminary verification of this polymerization mechanism was revealed by FTIR analysis.[85]

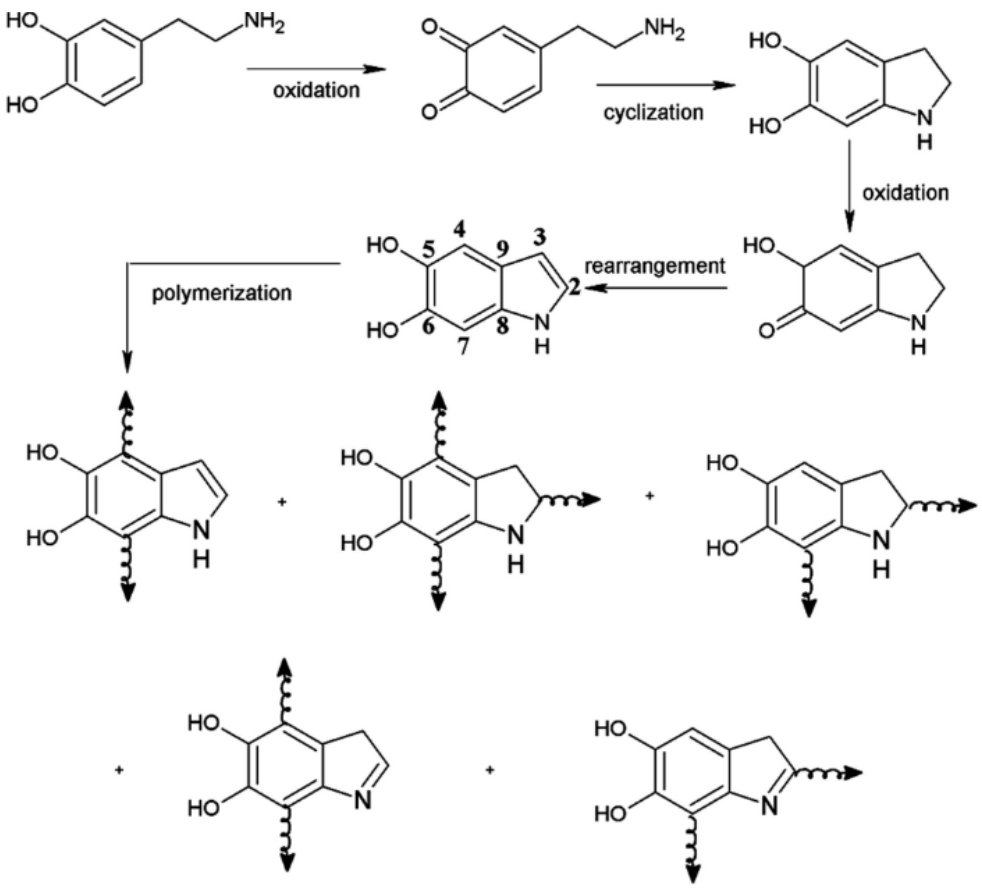

Figure 10. Eumelanin model of the molecular mechanism behind the formation of poly(dopamine).

The disappearance of the peaks at 1,519 cm^{-1} (NH_2 scissoring vibration) and 1,342 cm^{-1} (CH_2 bending vibration), the relatively large absorbance in the 1,500−1,100 cm^{-1} region, as well as the broadened width of the peak at 1,630 cm^{-1} in the FT-IR spectrum of the polymer as compared to that of dopamine monomer all verified the intramolecular cyclization reaction had occurred in dopamine along with the formation of indole derivatives.

The most important properties of poly(dopamine), which is particularly interesting for physicists and chemists, is the strong adhesion to virtually any type of surface, without regard for the substrate's chemistry. Even though there is a general perception that the catechol group plays a central role in the diversity of mussel imitation, the exact bonding mechanism is still difficult to grasp. It is easy to envisage that a covalent binding mechanism can be applied to some specific substrates that contain amine and/or thiol groups on their surfaces via Michael addition and/or Schiff base reactions under alkaline conditions. On the other hand, poly(dopamine), similar to its monomer, is prone to diffusion on substrates through noncovalent binding interaction such as π−π stacking, hydrogen bonding, metal coordination or chelating, and quinhydrone charge-transfer complexes to provide an effective adlayer under ambient conditions. As a result, chelating and coordination bonding interactions play a key role in the adhesive properties of polydopamine on metal or metal oxide surfaces. For example, some results revealed that Fe_2O_3, Al_2O_3, ZrO_2, *etc.,* were coated with poly(dopamine) via the coordination interaction between the catechol group and metal. Adhesion to organic and hydrophobic surfaces is the most prominent advantage of polydopamine as compared with previous coating materials. However, the detailed mechanism of adhesive properties of poly(dopamine) is not yet known. With the help of atomic force microscopy (AFM), the adhesion mechanism of poly(dopamine) to organic surfaces depends on the oxidation of the catechol to quinones occurring in the alkaline environment, leading to covalent coupling to organic surfaces through Michael-type addition reactions or aryl−aryl coupling.[86]

4.2. Poly(dopamine)/GO hybrid materials

Reduction of graphene oxide (GO) is considered to be the most effective ways to synthesize high quality graphene with scalable production. Recently, the reduced graphene oxide (rGO) is generally produced by thermal annealing at high temperature or chemical reaction with reducing agents such as hydrazine, $NaBH_4$, and hydroquinone. However, the resultant rGO sheets are apt to agglomerate irreversibly due to the van der Waals interactions without additional stabilizer.

A new way for simultaneous mass production and stabilization of rGO in one step under mild conditions can be provided by the redox capacity of dopamine in the polymerization process. The first experiments were conducted in 2010,[87] and the experimental method was as follows: GO sheets were mixed with dopamine in Tris buffer, and the reaction was allowed to proceed at 60 °C under vigorous stirring. After 2 hr, the dark brown GO suspension gradually changed into a black solution, implying

the reduction of GO. It was noteworthy that this reaction was relatively fast, requiring only 2 hr to complete the whole reducing progress of GO, as identified by UV−vis and X-ray photoelectron spectroscopy (XPS) analysis (Figure 11).

Another striking merit of this procedure is that the polydopamine layer on the surface of rGO can facilitate the design of various rGO-based hybrid materials. On the one hand, poly(dopamine) on the surface of rGO supports the second modification by other molecules through Michael addition and/or Schiff-based reaction. For example, after modification with amino- or thiol-terminated PEG, the resultant poly(dopamine)-capped rGO can be easily dispersed in various solvents such as $CHCl_3$, DMF, THF, and water with long-term colloid stability, which is essential for the applications of rGO, particularly for bio applications. According to poly(dopamine) chemistry, in a very recent study, Feng and co-workers have further developed a facile method to prepare macroscopic GO papers by controlling the cross-linking reaction between polydopamine on the surface of GO sheets and polyetherimide.[88] As compared to previously reported filtration or liquid/air interface self-assembly methods for the preparation of GO papers, such a cross-linking reaction imparted interlayer interactions between the adjacent sheets, thus yielding GO papers with ultrahigh stiffness and higher strength; the Young's modulus increased by 550%, and the strength was twice that of noncross-linked GO papers.

Despite the simplicity and versatility of the reductive process, the details of the reduction mechanism still remain thus far. Possibly, the release of electrons during the polymerization of dopamine will attack the oxygen-containing species such as C=O in GO, and such an electron transfer process seems to be the key to the complete reduction of the GO. Some researchers have argued that the reduction process of GO at 60 ^{o}C follows two steps: S_N2 nucleophilic reactions and a subsequent thermal elimination of catechol groups. The first step involves the attack at the epoxy ring or hydroxyl on the GO by catechol groups of dopamine, coupled with release of one H_2O molecule. Thermal treatment would result in the elimination of catechol groups, leaving the sp^2 skeleton behind, as well as dopamine-quinone, which would further undergo self-polymerization on the surface of rGO.

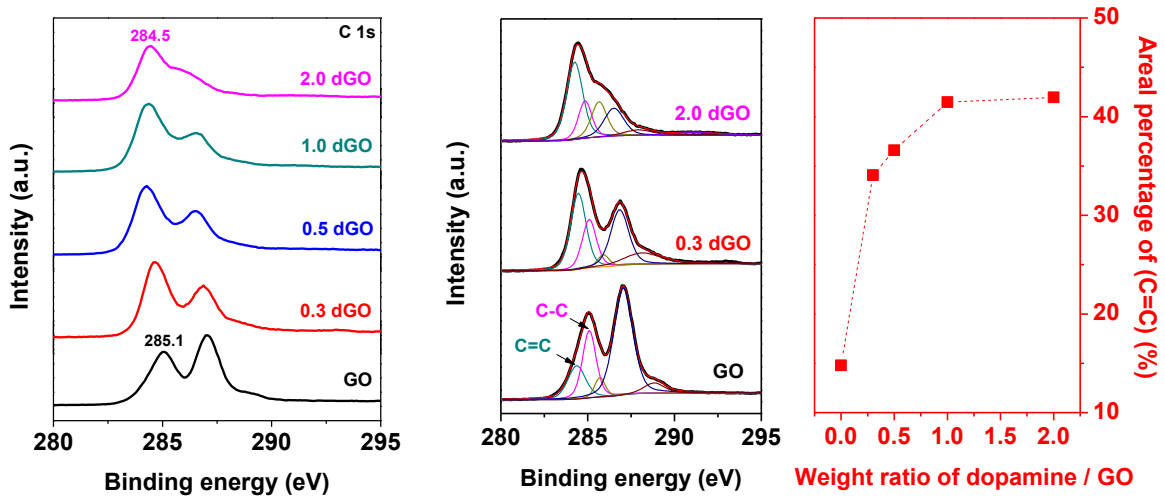

Figure 11. C 1s and deconvoluted XPS spectra of GO and dGO with different dopamine contents, and change of areal percentage of (C=C) peak.

5. References

1. Lu, X.; Yu, M.; Huang, H.; Ruoff, R. S., Tailoring graphite with the goal of achieving single sheets. *Nanotechnology* **1999,** *10* (3), 269.
2. Novoselov, K. S.; Geim, A. K.; Morozov, S. V.; Jiang, D.; Zhang, Y.; Dubonos, S. V.; Grigorieva, I. V.; Firsov, A. A., Electric field effect in atomically thin carbon films. *Science* **2004,** *306* (5696), 666-669.
3. Neto, A. C.; Guinea, F.; Peres, N. M.; Novoselov, K. S.; Geim, A. K., The electronic properties of graphene. *Reviews of modern physics* **2009,** *81* (1), 109.
4. Lothe, J. H. J.; Hirth, J. P., Theory of dislocations. *Wiley, New York* **1982**, 270.
5. Veprek, S., Structural Nanocrystalline Materials: Fundamentals and Applications. Cambridge University Press, Cambridge: 2007.
6. Zhu, T.; Li, J., Ultra-strength materials. *Progress in Materials Science* **2010,** *55* (7), 710-757.
7. Lee, C.; Wei, X.; Kysar, J. W.; Hone, J., Measurement of the elastic properties and intrinsic strength of monolayer graphene. *Science* **2008,** *321* (5887), 385-388.
8. Ni, Z.; Wang, H.; Kasim, J.; Fan, H.; Yu, T.; Wu, Y.; Feng, Y.; Shen, Z., Graphene thickness determination using reflection and contrast spectroscopy. *Nano Letters* **2007,** *7* (9), 2758-2763.
9. Smith, D.; Shiles, E.; Inokuti, M.; Palik, E., Handbook of optical constants of solids. *Handbook of Optical Constants of Solids* **1985,** *1*, 369-406.
10. Faugeras, C.; Faugeras, B.; Orlita, M.; Potemski, M.; Nair, R. R.; Geim, A., Thermal conductivity of graphene in corbino membrane geometry. *ACS Nano* **2010,** *4* (4), 1889-1892.
11. Jauregui, L. A.; Yue, Y.; Sidorov, A. N.; Hu, J.; Yu, Q.; Lopez, G.; Jalilian, R.; Benjamin, D. K.; Delkd, D. A.; Wu, W., Thermal transport in graphene nanostructures: Experiments and simulations. *ECS Transactions* **2010,** *28* (5), 73-83.
12. Seol, J. H.; Jo, I.; Moore, A. L.; Lindsay, L.; Aitken, Z. H.; Pettes, M. T.; Li, X.; Yao, Z.; Huang, R.; Broido, D., Two-dimensional phonon transport in supported graphene. *Science* **2010,** *328* (5975), 213-216.
13. Novoselov, K.; Jiang, D.; Schedin, F.; Booth, T.; Khotkevich, V.; Morozov, S.; Geim, A., Two-dimensional atomic crystals. *Proceedings of the National Academy of Sciences of the United States of America* **2005,** *102* (30), 10451-10453.
14. Park, S.; Ruoff, R. S., Chemical methods for the production of graphenes. *Nature Nanotechnology* **2009,** *4* (4), 217-224.
15. Hernandez, Y.; Nicolosi, V.; Lotya, M.; Blighe, F. M.; Sun, Z.; De, S.; McGovern, I.; Holland, B.; Byrne, M.; Gun'Ko, Y. K., High-yield production of graphene by liquid-phase exfoliation of graphite. *Nature Nanotechnology* **2008,** *3* (9), 563-568.
16. Wu, J.; Agrawal, M.; Becerril, H. A.; Bao, Z.; Liu, Z.; Chen, Y.; Peumans, P., Organic light-

emitting diodes on solution-processed graphene transparent electrodes. *ACS Nano* **2009,** *4* (1), 43-48.

17. Kim, K. S.; Zhao, Y.; Jang, H.; Lee, S. Y.; Kim, J. M.; Kim, K. S.; Ahn, J.-H.; Kim, P.; Choi, J.-Y.; Hong, B. H., Large-scale pattern growth of graphene films for stretchable transparent electrodes. *Nature* **2009,** *457* (7230), 706-710.
18. Reina, A.; Jia, X.; Ho, J.; Nezich, D.; Son, H.; Bulovic, V.; Dresselhaus, M. S.; Kong*, J., Layer area, few-layer graphene films on arbitrary substrates by chemical vapor deposition. *Nano Letters* **2009,** *9* (8), 3087-3087.
19. Li, X.; Cai, W.; An, J.; Kim, S.; Nah, J.; Yang, D.; Piner, R.; Velamakanni, A.; Jung, I.; Tutuc, E., Large-area synthesis of high-quality and uniform graphene films on copper foils. *Science* **2009,** *324* (5932), 1312-1314.
20. Yu, Q.; Lian, J.; Siriponglert, S.; Li, H.; Chen, Y. P.; Pei, S.-S., Graphene segregated on Ni surfaces and transferred to insulators. *Applied Physics Letters* **2008,** *93* (11), 113103.
21. Li, X.; Cai, W.; Colombo, L.; Ruoff, R. S., Evolution of graphene growth on Ni and Cu by carbon isotope labeling. *Nano Letters* **2009,** *9* (12), 4268-4272.
22. May, J. W., Platinum surface LEED rings. *Surface Science* **1969,** *17* (1), 267-270.
23. Shelton, J.; Patil, H.; Blakely, J., Equilibrium segregation of carbon to a nickel (111) surface: A surface phase transition. *Surface Science* **1974,** *43* (2), 493-520.
24. Eizenberg, M.; Blakely, J., Carbon interaction with nickel surfaces: Monolayer formation and structural stability. *The Journal of Chemical Physics* **1979,** *71* (8), 3467-3477.
25. Eizenberg, M.; Blakely, J., Carbon monolayer phase condensation on Ni (111). *Surface Science* **1979,** *82* (1), 228-236.
26. Hamilton, J.; Blakely, J., Carbon segregation to single crystal surfaces of Pt, Pd and Co. *Surface Science* **1980,** *91* (1), 199-217.
27. Berger, C.; Song, Z.; Li, T.; Li, X.; Ogbazghi, A. Y.; Feng, R.; Dai, Z.; Marchenkov, A. N.; Conrad, E. H.; First, P. N., Ultrathin epitaxial graphite: 2D electron gas properties and a route toward graphene-based nanoelectronics. *The Journal of Physical Chemistry B* **2004,** *108* (52), 19912-19916.
28. Berger, C.; Song, Z.; Li, X.; Wu, X.; Brown, N.; Naud, C.; Mayou, D.; Li, T.; Hass, J.; Marchenkov, A. N., Electronic confinement and coherence in patterned epitaxial graphene. *Science* **2006,** *312* (5777), 1191-1196.
29. De Heer, W. A.; Berger, C.; Wu, X.; First, P. N.; Conrad, E. H.; Li, X.; Li, T.; Sprinkle, M.; Hass, J.; Sadowski, M. L., Epitaxial graphene. *Solid State Communications* **2007,** *143* (1), 92-100.
30. Emtsev, K. V.; Bostwick, A.; Horn, K.; Jobst, J.; Kellogg, G. L.; Ley, L.; McChesney, J. L.; Ohta, T.; Reshanov, S. A.; Röhrl, J., Towards wafer-size graphene layers by atmospheric

pressure graphitization of silicon carbide. *Nature Materials* **2009,** *8* (3), 203-207.

31. Huang, H.; Chen, W.; Chen, S.; Wee, A. T. S., Bottom-up growth of epitaxial graphene on 6H-SiC (0001). *ACS Nano* **2008,** *2* (12), 2513-2518.
32. Li, X.; Zhu, Y.; Cai, W.; Borysiak, M.; Han, B.; Chen, D.; Piner, R. D.; Colombo, L.; Ruoff, R. S., Transfer of large-area graphene films for high-performance transparent conductive electrodes. *Nano Letters* **2009,** *9* (12), 4359-4363.
33. Hofmann, U.; Holst, R., Über die Säurenatur und die Methylierung von Graphitoxyd. *Berichte der deutschen chemischen Gesellschaft (A and B Series)* **1939,** *72* (4), 754-771.
34. Ruess, G., Über das graphitoxyhydroxyd (graphitoxyd). *Monatshefte für Chemie und verwandte Teile anderer Wissenschaften* **1947,** *76* (3-5), 381-417.
35. Mermoux, M.; Chabre, Y.; Rousseau, A., FTIR and 13C NMR study of graphite oxide. *Carbon* **1991,** *29* (3), 469-474.
36. Dubois, M.; Giraudet, J.; Guérin, K.; Hamwi, A.; Fawal, Z.; Pirotte, P.; Masin, F., EPR and solid-state NMR studies of poly (dicarbon monofluoride)(C2F) n. *The Journal of Physical Chemistry B* **2006,** *110* (24), 11800-11808.
37. Scholz, W.; Boehm, H., Untersuchungen am graphitoxid. VI. Betrachtungen zur struktur des graphitoxids. *Zeitschrift für anorganische und allgemeine Chemie* **1969,** *369* (3-6), 327-340.
38. Nakajima, T.; Mabuchi, A.; Hagiwara, R., A new structure model of graphite oxide. *Carbon* **1988,** *26* (3), 357-361.
39. He, H.; Riedl, T.; Lerf, A.; Klinowski, J., Solid-state NMR studies of the structure of graphite oxide. *The Journal of physical chemistry* **1996,** *100* (51), 19954-19958.
40. Lerf, A.; He, H.; Forster, M.; Klinowski, J., Structure of graphite oxide revisited. *The Journal of Physical Chemistry B* **1998,** *102* (23), 4477-4482.
41. Rodriguez, A. M.; Jimenez, P. V., Some new aspects of graphite oxidation at 0 C in a liquid medium. A mechanism proposal for oxidation to graphite oxide. *Carbon* **1986,** *24* (2), 163-167.
42. Brodie, B., Sur le poids atomique du graphite. *Ann. Chim. Phys* **1860,** *59* (466), e472.
43. Staudenmaier, L., Verfahren zur darstellung der graphitsäure. *Berichte der deutschen chemischen Gesellschaft* **1898,** *31* (2), 1481-1487.
44. Hummers Jr, W. S.; Offeman, R. E., Preparation of graphitic oxide. *Journal of the American Chemical Society* **1958,** *80* (6), 1339-1339.
45. Boehm, H.; Eckel, M.; Scholz, W., Untersuchungen am Graphitoxid V. Über den Bildungsmechanismus des Graphitoxids. *Zeitschrift für anorganische und allgemeine Chemie* **1967,** *353* (5-6), 236-242.
46. Paredes, J.; Villar-Rodil, S.; Martínez-Alonso, A.; Tascon, J., Graphene oxide dispersions in organic solvents. *Langmuir* **2008,** *24* (19), 10560-10564.
47. Jang, B. Z.; Zhamu, A., Processing of nanographene platelets (NGPs) and NGP nanocomposites:

a review. *Journal of Materials Science* **2008,** *43* (15), 5092-5101.

48. McAllister, M. J.; Li, J.-L.; Adamson, D. H.; Schniepp, H. C.; Abdala, A. A.; Liu, J.; Herrera-Alonso, M.; Milius, D. L.; Car, R.; Prud'homme, R. K., Single sheet functionalized graphene by oxidation and thermal expansion of graphite. *Chemistry of Materials* **2007,** *19* (18), 4396-4404.
49. Liang, J.; Huang, Y.; Zhang, L.; Wang, Y.; Ma, Y.; Guo, T.; Chen, Y., Molecular-level dispersion of graphene into poly (vinyl alcohol) and effective reinforcement of their nanocomposites. *Advanced Functional Materials* **2009,** *19* (14), 2297-2302.
50. Salavagione, H. J.; Martínez, G.; Gómez, M. A., Synthesis of poly (vinyl alcohol)/reduced graphite oxide nanocomposites with improved thermal and electrical properties. *Journal of Materials Chemistry* **2009,** *19* (28), 5027-5032.
51. Ramanathan, T.; Abdala, A.; Stankovich, S.; Dikin, D.; Herrera-Alonso, M.; Piner, R.; Adamson, D.; Schniepp, H.; Chen, X.; Ruoff, R., Functionalized graphene sheets for polymer nanocomposites. *Nature Nanotechnology* **2008,** *3* (6), 327-331.
52. Steurer, P.; Wissert, R.; Thomann, R.; Mülhaupt, R., Functionalized graphenes and thermoplastic nanocomposites based upon expanded graphite oxide. *Macromolecular Rapid Communications* **2009,** *30* (4-5), 316-327.
53. Wang, S.; Tambraparni, M.; Qiu, J.; Tipton, J.; Dean, D., Thermal expansion of graphene composites. *Macromolecules* **2009,** *42* (14), 5251-5255.
54. Rafiee, M.; Rafiee, J.; Yu, Z.-Z.; Koratkar, N., Buckling resistant graphene nanocomposites. *Applied Physics Letters* **2009,** *95* (22), 223103.
55. Stankovich, S.; Dikin, D. A.; Dommett, G. H.; Kohlhaas, K. M.; Zimney, E. J.; Stach, E. A.; Piner, R. D.; Nguyen, S. T.; Ruoff, R. S., Graphene-based composite materials. *nature* **2006,** *442* (7100), 282-286.
56. Veca, L. M.; Lu, F.; Meziani, M. J.; Cao, L.; Zhang, P.; Qi, G.; Qu, L.; Shrestha, M.; Sun, Y.-P., Polymer functionalization and solubilization of carbon nanosheets. *Chemical Communications* **2009,** (18), 2565-2567.
57. Ganguli, S.; Roy, A. K.; Anderson, D. P., Improved thermal conductivity for chemically functionalized exfoliated graphite/epoxy composites. *Carbon* **2008,** *46* (5), 806-817.
58. Hu, H.; Wang, X.; Wang, J.; Wan, L.; Liu, F.; Zheng, H.; Chen, R.; Xu, C., Preparation and properties of graphene nanosheets–polystyrene nanocomposites via in situ emulsion polymerization. *Chemical Physics Letters* **2010,** *484* (4), 247-253.
59. Yang, Y.; Wang, J.; Zhang, J.; Liu, J.; Yang, X.; Zhao, H., Exfoliated graphite oxide decorated by PDMAEMA chains and polymer particles. *Langmuir* **2009,** *25* (19), 11808-11814.
60. Fang, M.; Wang, K.; Lu, H.; Yang, Y.; Nutt, S., Covalent polymer functionalization of graphene nanosheets and mechanical properties of composites. *Journal of Materials Chemistry* **2009,** *19* (38), 7098-7105.

61. Wakabayashi, K.; Pierre, C.; Dikin, D. A.; Ruoff, R. S.; Ramanathan, T.; Brinson, L. C.; Torkelson, J. M., Polymer-graphite nanocomposites: effective dispersion and major property enhancement via solid-state shear pulverization. *Macromolecules* **2008,** *41* (6), 1905-1908.

62. Kalaitzidou, K.; Fukushima, H.; Drzal, L. T., A new compounding method for exfoliated graphite–polypropylene nanocomposites with enhanced flexural properties and lower percolation threshold. *Composites Science and Technology* **2007,** *67* (10), 2045-2051.

63. Wei, T.; Luo, G.; Fan, Z.; Zheng, C.; Yan, J.; Yao, C.; Li, W.; Zhang, C., Preparation of graphene nanosheet/polymer composites using in situ reduction–extractive dispersion. *Carbon* **2009,** *47* (9), 2296-2299.

64. Vickery, J. L.; Patil, A. J.; Mann, S., Fabrication of Graphene–Polymer Nanocomposites With Higher-Order Three-Dimensional Architectures. *Advanced Materials* **2009,** *21* (21), 2180-2184.

65. Hong, T.-K.; Lee, D. W.; Choi, H. J.; Shin, H. S.; Kim, B.-S., Transparent, flexible conducting hybrid multilayer thin films of multiwalled carbon nanotubes with graphene nanosheets. *ACS Nano* **2010,** *4* (7), 3861-3868.

66. Zheng, Q.; Zhang, B.; Lin, X.; Shen, X.; Yousefi, N.; Huang, Z.-D.; Li, Z.; Kim, J.-K., Highly transparent and conducting ultralarge graphene oxide/single-walled carbon nanotube hybrid films produced by Langmuir–Blodgett assembly. *Journal of Materials Chemistry* **2012,** *22* (48), 25072-25082.

67. Peng, L.; Feng, Y.; Lv, P.; Lei, D.; Shen, Y.; Li, Y.; Feng, W., Transparent, conductive, and flexible multiwalled carbon nanotube/graphene hybrid electrodes with two three-dimensional microstructures. *The Journal of Physical Chemistry C* **2012,** *116* (8), 4970-4978.

68. Li, Y.; Peng, Z.; Larios, E.; Wang, G.; Lin, J.; Yan, Z.; Ruiz-Zepeda, F.; José-Yacamán, M.; Tour, J. M., Rebar Graphene from Functionalized Boron Nitride Nanotubes. *ACS Nano* **2014,** *9* (1), 532-538.

69. Yan, Z.; Peng, Z.; Casillas, G.; Lin, J.; Xiang, C.; Zhou, H.; Yang, Y.; Ruan, G.; Raji, A.-R. O.; Samuel, E. L., Rebar graphene. *ACS Nano* **2014,** *8* (5), 5061-5068.

70. Kim, Y.-S.; Kumar, K.; Fisher, F. T.; Yang, E.-H., Out-of-plane growth of CNT on graphene for supercapacitor applications. *Nanotechnology* **2011,** *23* (1), 015301.

71. Cui, X.; Lv, R.; Sagar, R. U. R.; Liu, C.; Zhang, Z., Reduced graphene oxide/carbon nanotube hybrid film as high performance negative electrode for supercapacitor. *Electrochimica Acta* **2015,** *169*, 342-350.

72. Shao, M.; Peles, A.; Shoemaker, K., Electrocatalysis on platinum nanoparticles: particle size effect on oxygen reduction reaction activity. *Nano Letters* **2011,** *11* (9), 3714-3719.

73. Guo, S.; Sun, S., FePt nanoparticles assembled on graphene as enhanced catalyst for oxygen reduction reaction. *Journal of the American Chemical Society* **2012,** *134* (5), 2492-2495.

74. Xin, Y.; Liu, J.-g.; Zhou, Y.; Liu, W.; Gao, J.; Xie, Y.; Yin, Y.; Zou, Z., Preparation and

characterization of Pt supported on graphene with enhanced electrocatalytic activity in fuel cell. *Journal of Power Sources* **2011,** *196* (3), 1012-1018.

75. Li, Y.; Li, Y.; Zhu, E.; McLouth, T.; Chiu, C.-Y.; Huang, X.; Huang, Y., Stabilization of high-performance oxygen reduction reaction Pt electrocatalyst supported on reduced graphene oxide/carbon black composite. *Journal of the American Chemical Society* **2012,** *134* (30), 12326-12329.
76. Nardecchia, S.; Carriazo, D.; Ferrer, M. L.; Gutiérrez, M. C.; del Monte, F., Three dimensional macroporous architectures and aerogels built of carbon nanotubes and/or graphene: synthesis and applications. *Chemical Society Reviews* **2013,** *42* (2), 794-830.
77. Mao, S.; Lu, G.; Chen, J., Three-dimensional graphene-based composites for energy applications. *Nanoscale* **2015,** *7* (16), 6924-6943.
78. Luo, B.; Zhi, L., Design and construction of three dimensional graphene-based composites for lithium ion battery applications. *Energy & Environmental Science* **2015,** *8* (2), 456-477.
79. Cao, X.; Yin, Z.; Zhang, H., Three-dimensional graphene materials: preparation, structures and application in supercapacitors. *Energy & Environmental Science* **2014,** *7* (6), 1850-1865.
80. Zhu, C.; Guo, S.; Zhai, Y.; Dong, S., Layer-by-layer self-assembly for constructing a graphene/platinum nanoparticle three-dimensional hybrid nanostructure using ionic liquid as a linker. *Langmuir* **2010,** *26* (10), 7614-7618.
81. Sattayasamitsathit, S.; Gu, Y.; Kaufmann, K.; Jia, W.; Xiao, X.; Rodriguez, M.; Minteer, S.; Cha, J.; Burckel, D. B.; Wang, C., Highly ordered multilayered 3D graphene decorated with metal nanoparticles. *Journal of Materials Chemistry A* **2013,** *1* (5), 1639-1645.
82. Waite, J. H.; Tanzer, M. L., Polyphenolic substance of Mytilus edulis: novel adhesive containing L-dopa and hydroxyproline. *Science* **1981,** *212* (4498), 1038-1040.
83. Lee, H.; Dellatore, S. M.; Miller, W. M.; Messersmith, P. B., Mussel-inspired surface chemistry for multifunctional coatings. *Science* **2007,** *318* (5849), 426-430.
84. Ouyang, R.; Lei, J.; Ju, H.; Xue, Y., A molecularly imprinted copolymer designed for enantioselective recognition of glutamic acid. *Advanced Functional Materials* **2007,** *17* (16), 3223-3230.
85. Yu, F.; Chen, S.; Chen, Y.; Li, H.; Yang, L.; Chen, Y.; Yin, Y., Experimental and theoretical analysis of polymerization reaction process on the polydopamine membranes and its corrosion protection properties for 304 Stainless Steel. *Journal of Molecular Structure* **2010,** *982* (1), 152-161.
86. Lee, H.; Scherer, N. F.; Messersmith, P. B., Single-molecule mechanics of mussel adhesion. *Proceedings of the National Academy of Sciences* **2006,** *103* (35), 12999-13003.
87. Xu, L. Q.; Yang, W. J.; Neoh, K.-G.; Kang, E.-T.; Fu, G. D., Dopamine-induced reduction and functionalization of graphene oxide nanosheets. **2010**.

88. Tian, Y.; Cao, Y.; Wang, Y.; Yang, W.; Feng, J., Realizing ultrahigh modulus and high strength of macroscopic graphene oxide papers through crosslinking of mussel-inspired polymers. *Advanced Materials* **2013,** *25* (21), 2980-2983.

Chapter 2: Poly(vinyl alcohol) reinforced and toughened with poly(dopamine)-treated graphene oxide, and its use for humidity sensing

1. Introduction

Carbon/polymer nanostructure composites have been studied in part due to the possibility of achieving superior mechanical, electrical, and optical properties.[1-3] Carbon nanotubes (CNT) have been widely used as a filler in polymer matrices, but agglomeration, the presence of catalytic impurities, and relatively high cost have presented challenges. Chemically modified graphene has been studied as a new type of filler[4-7] due in part to its potential for imparting excellent mechanical, electrical, and optical properties in polymer composites.[1, 8-9] Graphene oxide (GO), *i.e.,* single layers of graphite oxide, can be obtained through simple dispersion in water, and because such individual layers can be readily achieved, it has been of interest to use chemically modified graphene as a filler in composite materials.[10-12] Oxygen-containing functional groups, including hydroxyl, epoxide, ketone, and carboxylic acid, render GO water dispersible.[10, 13-14] In certain cases, such functional groups may improve the interfacial bonding to the matrix as has been reported for some functionalized CNT.[15] Polymer composites containing functionalized grapheme are a relatively new area of composites research.[1] Some studies have indicated significant improvements in composite properties, with the degree of dispersion of the functionalized graphene in the polymer matrix reported as particularly important.[16-17] In some studies exceptional improvements were reported for very low filler loadings, and this was ascribed to the large surface area of graphene-based fillers.[8, 18] In addition to GO and related functionalized graphene sheets, expanded graphite and exfoliated graphite "nanoplatelets" have also been used as fillers to make conducting composites, sometimes also with improved mechanical, thermal, and optical properties. There have been many studies of polymer composites made with expanded or exfoliated graphite including epoxy, poly(methyl methacrylate) (PMMA), polypropylene, linear low density polyethylene (LLDPE), high density polyethylene (HDPE), polystyrene, polyphenylene sulfide (PPS), nylon, and silicone rubber.[19-25] These studies reported that expanded or exfoliated graphite as a filler can increase tensile modulus by 8-130 %; ultimate tensile strength, however, is reported in some studies to be increased and in others to be decreased. Stankovich *et al.* reported the preparation of chemically functionalized graphene/polymer composites and an electrical percolation threshold of only 0.1 vol %, specifically with polystyrene.[8] Ramanathan *et al.* studied the mechanical properties of chemically functionalized grapheme sheet/PMMA composites and reported substantially improved interaction between the host polymer and the chemically functionalized graphene compared to those containing expanded/exfoliated graphite or unmodified single-walled carbon nanotubes.[26] Oxygen-containing functional groups are reported to be well suited for composites with a polar polymer matrix, such as PMMA,

polyacrylonitrile (PAN) and poly(acrylic acid) (PAA), and "intimate" graphene/polymer interactions and a percolated interphase essential for mechanical enhancement have been reported.[26] Therefore, poly(vinyl alcohol) PVA filled with GO could be a good combination for achieving strong interfacial bonding, as PVA chains should strongly bind on the surface of GO by hydrogen bonding. On the basis of this rationale, PVA/GO composites have been explored both experimentally and theoretically, and the relationship between hydrogen bonding density and the mechanical properties of the composites has been studied. Zhang *et al.* and Wang *et al.* reported increased tensile modulus, strength, and strain-to-failure at GO loadings lower than 11.8 wt %.[27-28] Wang *et al.* reported that the yield strengths of GO/PVA composites increased linearly up to 11.01 MPa (a 136 % increase compared to neat PVA) as GO content was increased from 0 to 5 wt %; a maximum strain-to-failure of 210% (a 27 % increase) was reported at 1.5 wt % loading. Chemically functionalized graphene sheets covalently bonded to PVA were studied, and yield strength and strain-to-failure of 72 MPa and 191 %, respectively, were reported at 0.5 wt % loading.[27] Zhang *et al.*, reported tensile strength and strain-to-failure of 3.48 MPa (a 132 % increase) and 165 % (a 62 % increase) at 1 wt % loading for the same composite system. PVA/GO or chemically functionalized graphene/PVA composites are reported to show this unusual increase in toughness because of their "molecular level" dispersion and high density of hydrogen bonding. An ideal configuration would be when the edges of the sheets are joined together side by side. However, when a critical content is reached, *i.e.*, 11.8 wt %, the GO sheets begin to stack together driven by the strong van der Waals force, decreasing the efficiency of the mechanical reinforcement.[28]

Dopamine, which is a small molecule containing catechol and amine groups, is a kind of hormone and neurotransmitter, and its polymerized form, known as poly(dopamine), is similar to adhesive proteins of mussels. At a weak alkaline pH condition, dopamine self-polymerizes to produce an adherent poly(dopamine) coating on a wide range of substrates with the oxidation of catechol groups to the quinone form.[29-31] It binds strongly to most organic and inorganic surfaces, such as metals, metal oxides, and polymer surfaces. Also, the oxidized quinone form of catechol can undergo reactions with various functional groups, such as thiol, amine, and quinone itself, by Michael addition or the Schiff base reaction to form covalently grafted functional layers. Moreover, dopamine could be used to reduce GO during its polymerization on the GO surface.[32]

Here, we report a simple and practical approach to synthesize graphene-reinforced PVA composite films by combining graphene oxide (GO) with poly(dopamine), (dGO), in an aqueous solution with the simultaneous reduction of GO to reduced grapheme oxide sheets. The dGO/PVA composites obtained exhibited significant improvements in mechanical properties as a result of increased interfacial interactions produced by the combined mechanisms of hydrogen bonding between amine and hydroxyl groups of poly(dopamine) and abundant hydroxyl groups of PVA and polymer entanglement between PVA and poly(dopamine) (Figure 1).[33] Poly(dopamine) is also believed to play

a role of binding with GO sheets via hydrogen bonding between amine and hydroxyl groups of poly(dopamine) and hydroxyl groups of GO as well as π-π interaction between catechol and small graphitic domains of GO.[34] With the addition of dGO, we achieved simultaneous improvements in tensile modulus, strength, and strain-to-failure. We also demonstrated that dGO/PVA composite films can be used as structurally robust humidity sensors that use electrical conductivity to measure humidity.

2. Experimental section

2.1. Materials

Graphite (SP-1, Bay Carbon), H_2SO_4 (98%, Merck), P_2O_5 (99.99%, Aldrich), $K_2S_2O_8$ (99.0%, Sigma-Aldrich), $KMnO_4$ (99.0%, Sigma-Aldrich), H_2O_2 (30%, Daejung), dopamine hydrochloride (98.5%, Sigma) and tris-HCl (99.9%, Baker) were used as received without further purification.

2.2. Preparation of GO Solution.

Graphite oxide was prepared from purified natural graphite (SP-1, Bay Carbon) using the modified Hummers method. The graphite powder (2.0 g) was put into a solution of concentrated H_2SO_4 (3.0 mL), $K_2S_2O_8$ (1.0 g), and P_2O_5 (1.0 g) at 80 ^oC. The resultant dark blue mixture was allowed to cool to room temperature over a period of 6 hr and was then carefully diluted with distilled water, filtered, and washed on the filter until the pH of the rinse water became neutral. The product was dried in air at ambient conditions overnight. This pre-oxidized graphite was then subjected to oxidation by the Hummers method. The pre oxidized graphite powder (2.0 g) was added to concentrated H_2SO_4 (46 mL) and $KMnO_4$ (6.0 g) was added gradually with stirring and cooling, while the temperature of the mixture was maintained below 20 ^oC. The mixture was then stirred at 35 ^oC for 2 hr, and distilled water (92 mL) was added. After 15 min, the reaction was terminated by the addition of a large amount of distilled water (280 mL) and a 30% H_2O_2 solution (5.0 mL), after which the color of the mixture changed from black to bright yellow. The mixture was filtered and washed with a 1:10 HCl solution (500 mL) in order to remove metal ions. The graphite oxide product was suspended in distilled water to give a viscous, brown dispersion, which was subjected to dialysis to completely remove metal ions and acids. To obtain the GO dispersion, graphite oxide was exfoliated by treatment with a mechanical homogenizer at 15,000 rpm for 15 min, followed by sonication (ultrasonic cleaner, 100 W, Branson) for 15 min and then centrifugation at 4,000 rpm for 10 min.

2.3. Preparation of dGO Solution.

75 mg of dopamine hydrochloride was added into a 150 mL tris-HCl buffer solution (10 mM), and pH of the solution was tuned to 8.5 using 0.1 M NaOH solution. Then, this solution was mixed with

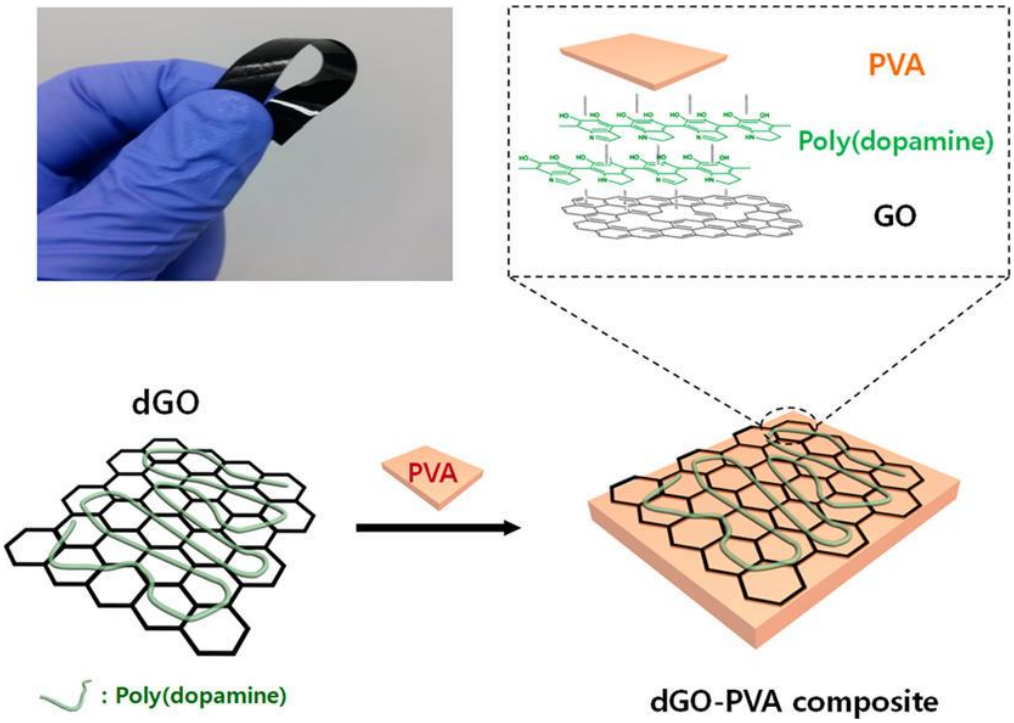

Figure 1. A photograph and proposed structure of a dGO/PVA composite film.

150 mL of the GO suspension (1.0 mg/mL) at ambient conditions and the mixture stirred for 2 hr at room temperature. Finally, the color of the solution turned to dark brown due to the pH-induced oxidative polymerization of dopamine hydrochloride and the reduction of GO.

2.4. Fabrication of dGO/PVA composite films.

The fabrication procedure for the dGO/PVA composite (GO loading = 0.5 wt %) was as follows: dGO was dispersed in distilled water (15 mL) in an ultrasonic bath for 60 min at room temperature. PVA (～2 g) was dissolved in distilled water (200 mL) at 90 °C. After the PVA-H_2O solution had cooled to around 60 °C, the dGO aqueous dispersion was gradually poured into the PVA solution and sonicated for an additional 15 min at room temperature. Finally, this homogeneous dGO/PVA solution was poured into a Teflon Petri-dish and kept at 60 °C for film formation until its weight equilibrated. The film was peeled from the substrate and was hot pressed at 200 °C in order to eliminate any remaining voids. A series of dGO/PVA composite films with various poly(dopamine):GO ratios (1:0, 0.5:1, 1:1) was similarly prepared. In all these samples, the GO content was kept constant at 0.5 wt %. For comparison, GO/PVA composite films were prepared according to the same procedure with a loading of 0.5 wt %. As a reference sample, a pure PVA film was prepared by the hot casting technique.

2.5. Characterization of dGO/PVA composite films.

Tensile properties, including modulus, strength, and strain-to-failure, of the films fabricated were measured using a dynamical mechanical analyzer (DMA Q800, TA Instruments), operated under a quasistatic, strain-controlled mode at a constant strain rate of 20 %/min. Specimens measuring 45 mm by 12 mm with a thickness of 80 μm were laser-cut (VersaLaser VLS 2.30, Universal Laser Systems) and installed in a film tensile fixture. Tensile tests were performed until the specimens ruptured. Load and elongation were measured simultaneously. The morphology of the fracture surfaces of tensile specimens was analyzed using a scanning electron microscope (SEM, FEI Nanonova 230). To assess the potential applicability of dGO/PVA composite films as humidity sensors, water uptake, quantified by swelling ratio, and humidity sensitivity were measured. Vacuum-dried film samples were immersed in distilled water until saturated and their weight became constant. The samples were then removed from the water, and their surfaces were blotted with a filter paper before being weighed. The swelling ratios of the films were calculated using the following formula:

$$Swelling\ ratio = \frac{W - W_0}{W_0} \times 100\ (\%)$$

where W_0 and W are the weights of the sample before and after immersing in water, respectively. A strip of a dGO/PVA composite film was installed in an inhouse-fabricated fixture devised to measure humidity sensitivity (Figure 2). The fixture was placed in a relative humidity (RH)-controlled chamber and soaked at a predefined RH until equilibrium was reached. RH was varied stepwise in a cyclic mode, while the change in film resistance was measured in situ, using a high-resistance digital multimeter (6517B, Keithley Instruments) at an applied voltage of 3 V.

3. Results and discussion

3.1. Characterization of dGO.

dGO was prepared by mixing an aqueous suspension of graphene oxide (GO) and a solution of dopamine hydrochloride in a buffer solution (10 mM Tris-HCl, pH 8.5). In a basic aqueous solution, poly(dopamine) is spontaneously formed by oxidative polymerization. The solutions were prepared with different GO/poly(dopamine) ratios such as 0.25:1, 0.5:1, and 1:1 (w/w). It was confirmed from scanning electron microscopy (SEM) images that the dGO sheets were well-dispersed in deionized water. The increase in thickness of the GO sheets by coating them with poly(dopamine) was determined by atomic force microscopy (AFM). Figure 3 shows the morphology and thickness of GO and dGO sheets. The thickness of as-prepared GO sheets was around 0.89 nm, which is thicker than pristine graphene due to the functional groups on the grapheme surfaces produced by the oxidation (Figure 3(a,b)).[35-36] On the other hand, the average thickness of dGO was around 2.24 nm (Figure 3(c,d)), indicating that the increase in thickness of 1.35 nm is due to the presence of poly(dopamine) on the GO sheets. Note that poly(dopamine) has a very similar structure to eumelanin, which is characterized by an interconnected layered structure along the *z*-axis with a graphite-like stacking spacing of 3.4-3.8 Å.[37-40]

The poly(dopamine) coating on the GO sheets was also proved by X-ray photoelectron spectroscopy (XPS). XPS survey spectra of GO and dGO samples in Figure 4(a) showed that a N 1s peak at 398 eV was observed in only the dGO sample. The N 1s peak originates from amine groups of the poly(dopamine) layer on GO sheets. From the XPS spectrum of the dGO sample, the nitrogen/carbon atomic ratio (N/C) was calculated to be 0.095 (Table in Figure 5). It has been reported that the theoretical value of N/C in dopamine is 0.125 and the N/C value in poly(dopamine) layers on different substrates is between 0.1and 0.13.[83] So, if we consider the GO layer as a substrate, the N/C value of 0.095 in our sample is quite reasonable. Figure 4(b) shows that in the C 1s binding region a peak due to oxygen-containing groups between 286 and 290 eV in the GO sample has been mostly removed in the dGO sample, indicating partial reduction of GO by the adsorption and polymerization of dopamine. Indeed, it has been known that GO can be reduced by released electrons during oxidative polymerization of catecholeamines such as dopamine and and norepinephrine.[32]

Figure 2. Sample holder and experimental setup for humidity sensing: (upper right) inhouse-fabricated sample fixture with embedded wires for in situ electrical resistance measurement; (lower right) inside view of the environmentally controlled chamber showing the sample in fixture and RH meter.

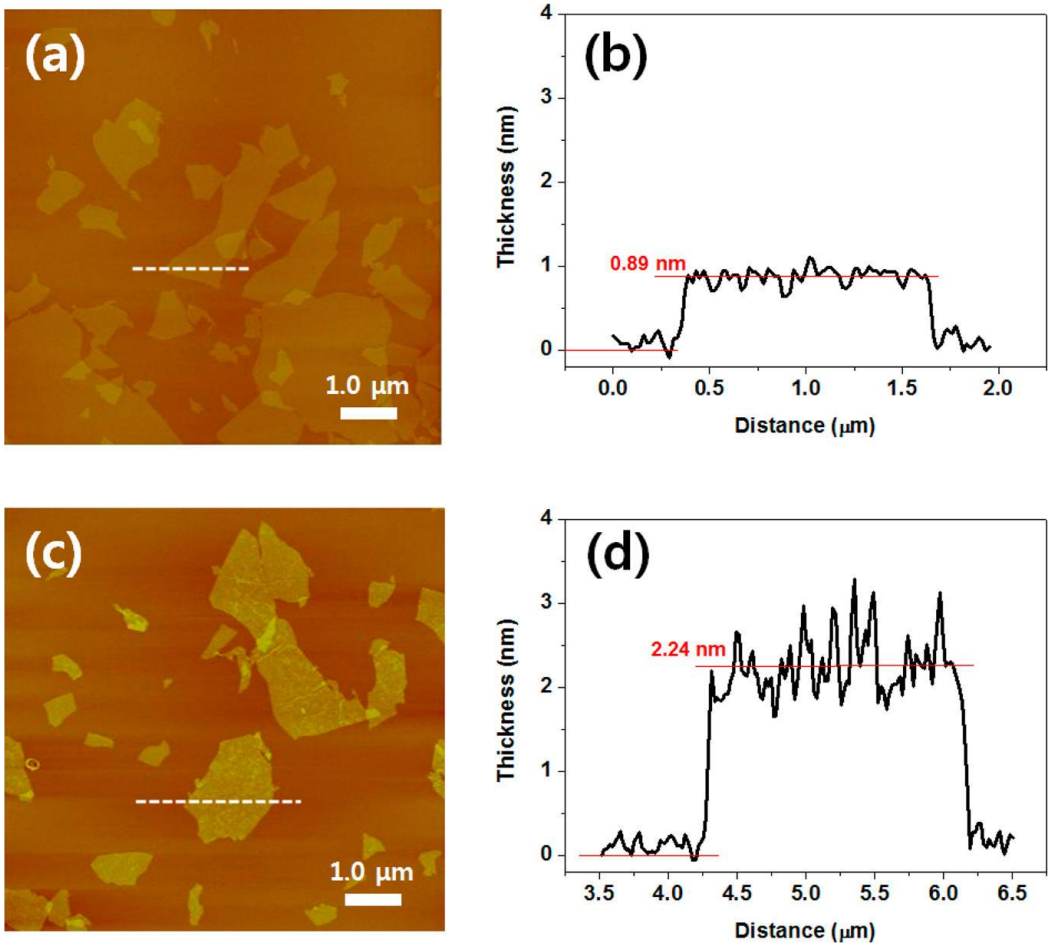

Figure 3. (a and b) AFM image and height profile of GO. (c and d) AFM image and height profile of dGO. GO and dGO (dopamine:GO = 0.5:1) samples were spin-coated on a Si wafer for AFM measurements.

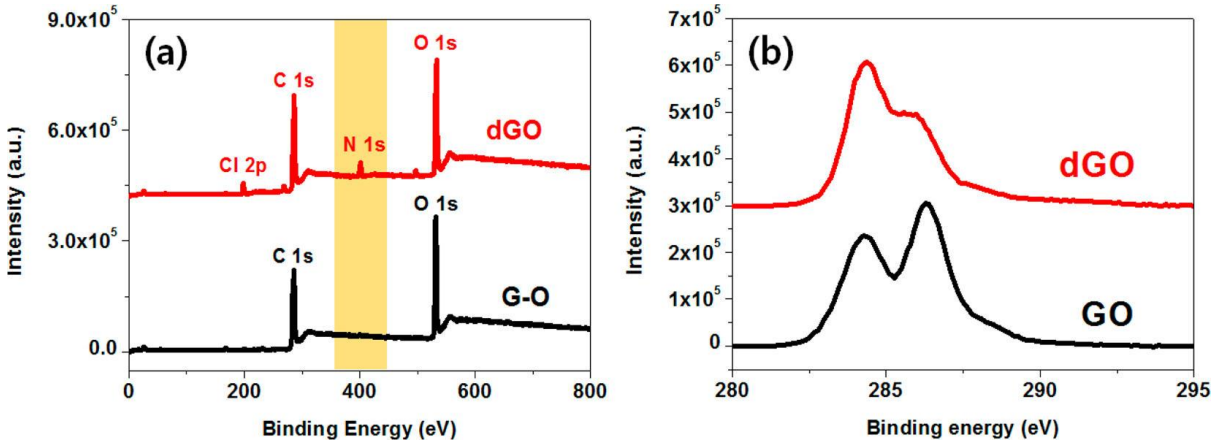

Figure 4. (a) XPS survey spectra and (b) C 1s binding energy region of GO and dGO spin-coated on a Si wafer. An additional Cl 2p peak in (a) originates from dopamine hydrochloride (HCl), which was used as the precursor of poly(dopamine).

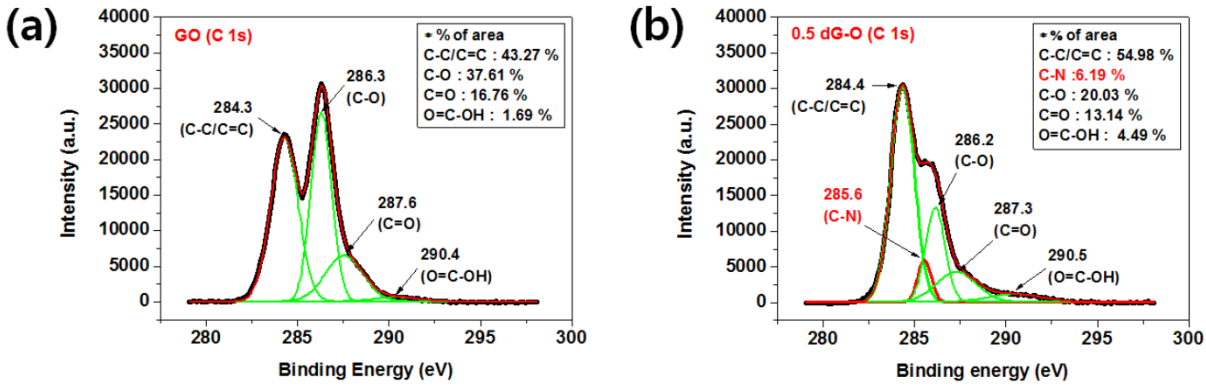

Samples	Elements	At. %	N/C atomic ratio
GO	C 1s	67.45	N/A
	O 1s	30.37	
	N 1s	-	
	Cl 2p	-	
dGO	C 1s	63.16	0.095
	O 1s	25.87	
	N 1s	6.57	
	Cl 2p	3.00	

Figure 5. Deconvoluted C 1s peaks of (a) GO, (b) dGO and atomic ratios (%) and N/C ratio of GO and dGO determined from XPS spectra

We measured attenuated total reflectance Fourier transform infrared (ATR-FT-IR) spectra of GO and dGO as shown in Figure 6.The typical FT-IR spectrum of GO shows OH stretching vibrations in the region of 3,000 to 3,400 cm^{-1}, C=O stretching vibrations from carbonyl and carboxylic groups at 1,720 cm^{-1}, skeletal vibrations from unoxidized graphitic domains at 1,620 cm^{-1}, C-OH stretching vibrations at 1,160 cm^{-1}, and C-O stretching vibrations at 1,040 cm^{-1}.[36, 41] On the other hand, the FT-IR spectrum of the dGO sample showed a newly developed peak at 1,500 cm^{-1}, corresponding to the N-H bending mode of aromatic secondary amine in dGO.[42] This result confirms that the poly(dopamine) on the GO sheets possesses aromatic, nitrogenous species, such as the indole- or indoline- type structures widely proposed in poly(dopamine) and eumelanins.[40] Note that the region between 3,000 and 3,400 cm^{-1} could not be used to identify the N-H stretching mode of secondary amine due to the broad band in the region possibly caused by strong hydrogen bonds between poly(dopamine) and oxygen-containing groups in GO sheets.

3.2. Mechanical properties of dGO/PVA films.

The mechanical properties of a composite reflect the state of its homogeneity and the interfacial interactions between its constituents. Typical stress-strain behaviors of dGO/PVA composites with different poly(dopamine): GO ratios and dGO contents are shown in Figure 7(a and b) and summarized in Tables 1 and 2. Previous research confirmed that GO has a significant effect on the mechanical properties of PVA composites.[36] In particular, Wang *et al.* showed that PVA is toughened by GO and rGO at very low loadings (～0.5 wt %).[28] Figure 7(a) shows both reinforcement and toughening. From Table 1, the average tensile modulus increases from 2.1 GPa for neat PVA to 3.31 GPa for a 0.5 wt % GO/PVA composite. In addition, the tensile strength also increases from 41.48 to 53.37 MPa, and the maximum strain-to-failure increases from 97.15 to 161.28%. It is obvious that dGO is a more effective reinforcement for PVA compared to as-synthesized GO. Table 1 shows that the addition of 0.5 wt % dGO to poly(dopamine): GO with a weight ratio of 0.5:1 results in the highest tensile strength of 82.9 MPa and a strain-to-failure of 184%. At a poly(dopamine): GO ratio of 1:1, the mechanical properties of the material were slightly decreased compared to that for the 0.5:1 ratio; however, they were still higher than the those of the as-prepared PVA/GO composite at the same loading. As the amount of poly(dopamine) layer becomes “excessive,” the heterogeneity between poly(dopamine) and PVA begins to generate a miscibility issue, thus adversely affecting the interfacial bonding and load transfer.

Figure 7(b) and Table 2 show that when dGO content in poly(dopamine): GO = 0.5:1 increases above 0.5 wt %, the ultimate tensile strength and maximum strain-to-failure decrease while the tensile modulus increases. This may be attributed to the fact that at dGO contents above 0.5 wt %, dGO restacking begins to dominate over the reinforcing effect, which adversely affects these parameters. As described by Wang *et al.*, several possible arrangements are available for graphene nanosheets in

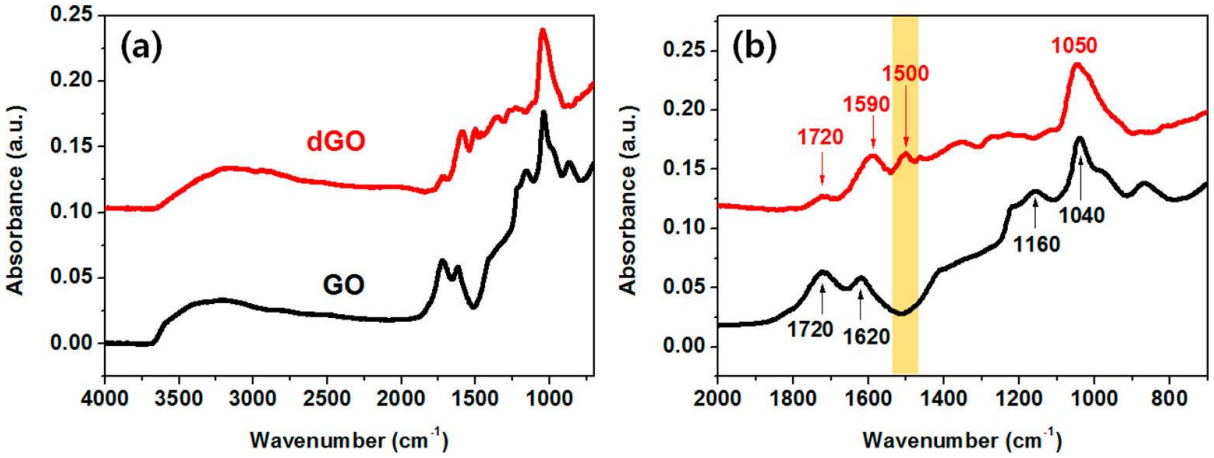

Figure 6. (a) ATR-FT-IR spectra of GO and dGO samples in the region between 4,000 and 700 cm^{-1} and (b) magnified wavenumber range of 2,000 to 700 cm^{-1} of GO and dGO. To obtain a thick film of GO and dGO for ATR-FT-IR measurement, each solution was repeatedly coated onto a Si wafer by drop casting.

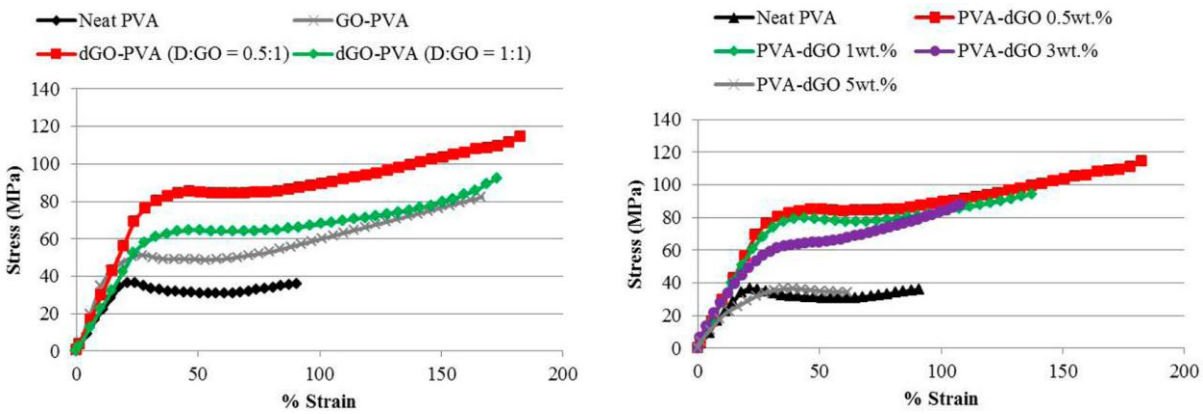

Figure 7. Stress-strain curves of (a) neat PVA, GO/PVA, dGO/PVA composite films at 0.5 wt % GO or dGO loading and (b) dGO/PVA composite films with various dGO loadings (poly(dopamine): GO = 0.5:1).

Table 1. Tensile properties of GO/PVA and dGO/PVA composites (at 0.5 wt % GO Loading)

Film type	Neat PVA	G-O/PVA	dG-O/PVA (D:G-O=0.5:1)	dG-O/PVA (D:G-O=1:1)
E (GPa)	2.10	3.31	2.92	2.48
UTS (MPa)	41.48	53.37	82.92	62.47
Strain-to-failure (%)	97.15	161.28	183.68	172.75

Table 2. Tensile properties of dGO/PVA composites (Poly(dopamine):GO = 0.5:1)

dG-O content (wt %)	0	0.5	1	3	5
E (GPa)	2.10	2.92	3.12	3.34	1.95
UTS (MPa)	41.48	82.92	80.92	80.92	39.12
Strain-to-failure (%)	97.15	183.68	132.51	119.95	52.82

the polymer matrix, among which side-by-side joining represents the ideal condition.[27] When a critical content is reached, grapheme sheets begin to restack together as the distance between two sheets become so small and the van der Waals force becomes substantial.[43] On the other hand, the tensile modulus increases because it is more dependent on the wt % of dGO and is much less sensitive to interfacial bonding.

3.3. Water resistance of dGO/PVA films.

To measure the effect of dGO on the swelling behavior of PVA films, water uptake of the composite films was measured as a function of time. As shown in Figure 8(a), the general observation is that all the samples show a relatively drastic increase in water adsorption up to ~5 hr, where it begins to level off. It is evident that the extent of water uptake decreases with increasing dGO content, indicative of dGO serving as a moisture barrier. GO is hydrophilic and contains numerous hydroxyl groups, which accelerate water adsorption when exposed to moisture. However, GO provides nanodispersed sites whose interactions with the surrounding PVA molecules restrain the swelling of GO/PVA composites, leading to a lower swelling ratio. Zhang *et al.* reported a critical maximum swelling ratio of ~170 % at 0.6 wt % GO.[28] However, our dGO/PVA composites show a lower maximum swelling ratio (around 120% at 3 or 5 wt % dGO) compared to a neat PVA film. Hence, it is believed that strong adhesion of poly(dopamine) to PVA chains can prevent swelling of the composites. Thus, a larger interfacial area was physically cross-linked by dGO in PVA films as shown in Figure 1. Also, water-dipping tests for the composite films in Figure 8 (b and c) show interesting results in that composites with 3 and 5 wt % of dGO exhibited no weight loss after 12 hr, whereas the neat PVA film dissolved in water and essentially disappeared.

3.4. Humidity sensing performance of dGO/PVA composite films.

PVA films with a dGO filler can serve as an effective humidity sensor due to their ability to absorb moisture to a moderate level while maintaining their structural integrity, with dGO serving as a moisture barrier as shown in Figure 8. The swelling of the polymer matrix due to moisture absorption leads to an increase in electrical resistance as the electrical conductive network formed by dGO nanosheets becomes disrupted. Electrical resistance versus RH is plotted for 3 and 5 wt % dGO/PVA films in Figure 9 (a and b). On the basis of the compositions of the composites, the mechanism behind the change in resistance when subjected to humidity can be explained as follows. In dGO/PVA composites, PVA acts as an insulating matrix. Meanwhile, polymerization of poly(dopamine) facilitates partial chemical reduction of GO, which imparts electrical conductivity in dGO/PVA composite films. When the surface of a dGO/PVA film is exposed to water molecules, adsorption occurs and capillary condensation of water produces a proton (H^+) as shown in equation (1).

$$H_2O = H^+ + OH^- \cdots\cdots (1)$$

This proton can be a carrier for the improvement of electrical conduction in dGO/PVA films, and more protons are produced when the sensing material is exposed to more humidity in the testing system.[44] In Figure 9 (a), the resistance of dGO/PVA films is plotted with stepwise dehumidification from a RH of 94.5 to 41.2%. From a comparison of 3 and 5 wt % dGO/PVA composite films, it is clear that the 3 wt % film shows a more drastic increase in resistance below 50% RH. This is attributed to the fact that at 3 wt % the loosely interconnected dGO conductive network is more susceptible to proton removal by dehumidification, compared to the 5 wt % material. In both stepwise dehumidification and continuous humidification cases, nonlinear resistance changes with respect to RH were observed, and the samples were more moisture-sensitive at lower RH values. This may be due to the fact that proton saturation for conduction is more readily reached in low humidity regions and is in good agreement with other reported results from PVA-based humidity sensors.[45-46] To characterize the repeatability and response of dGO/PVA films, dynamic adsorption-desorption cycles between 40 and 60% RH were used. Figure 10 shows the time response and recovery curve of a 5 wt % dGO/PVA film subjected to humidification-dehumidification cycles with a period of 10 min. The sample showed excellent sensing repeatability, and the difference in maximum resistance was less than 1% over 4 cycles. It is expected that the humidity sensing repeatability under cyclic input will be valid outside the range of 4060% RH, although the sensitivity will be lower above 60% RH.

Barkauskas showed the extremely narrow humidity sensing range of PVA (between 98 and 99 % RH, or 1.17% ΔRH) could be widened to 43.4% ΔRH by using different substrates, aging and the addition of carbon black.[47] To overcome this issue of a limited sensing range, Li *et al.* used polyaniline as a main sensor material, which was combined with PVA for water absorption.[45] Yang *et al.* added electrolytes, such as sodium chloride (NaCl) to a PVA matrix to increase both the sensitivity and sensitivity range of the PVA films.[48] Both approaches suffer from limitations in long-term stability and mechanical properties because of electrolyte loss and oxidation. However, we broadened the sensitivity range of PVA-based humidity sensors to 58.3% ΔRH without sacrificing structural integrity and long-term performance.

4. Conclusions

A simple approach was used to produce GO modified with poly(dopamine) in aqueous solution followed by spontaneous reduction of GO during the polymerization of dopamine to yield dGO. A combination of hydrogen bonding, strong adhesion of poly(dopamine) at the interface of PVA and GO, and reinforcing effects of GO resulted in simultaneous increases in tensile modulus, ultimate tensile strength, and strain-to-failure of 39, 100, and 89%, respectively, at a 0.5 wt % dGO loading. It was also demonstrated that dGO can serve as an effective moisture barrier in inherently water-soluble PVA

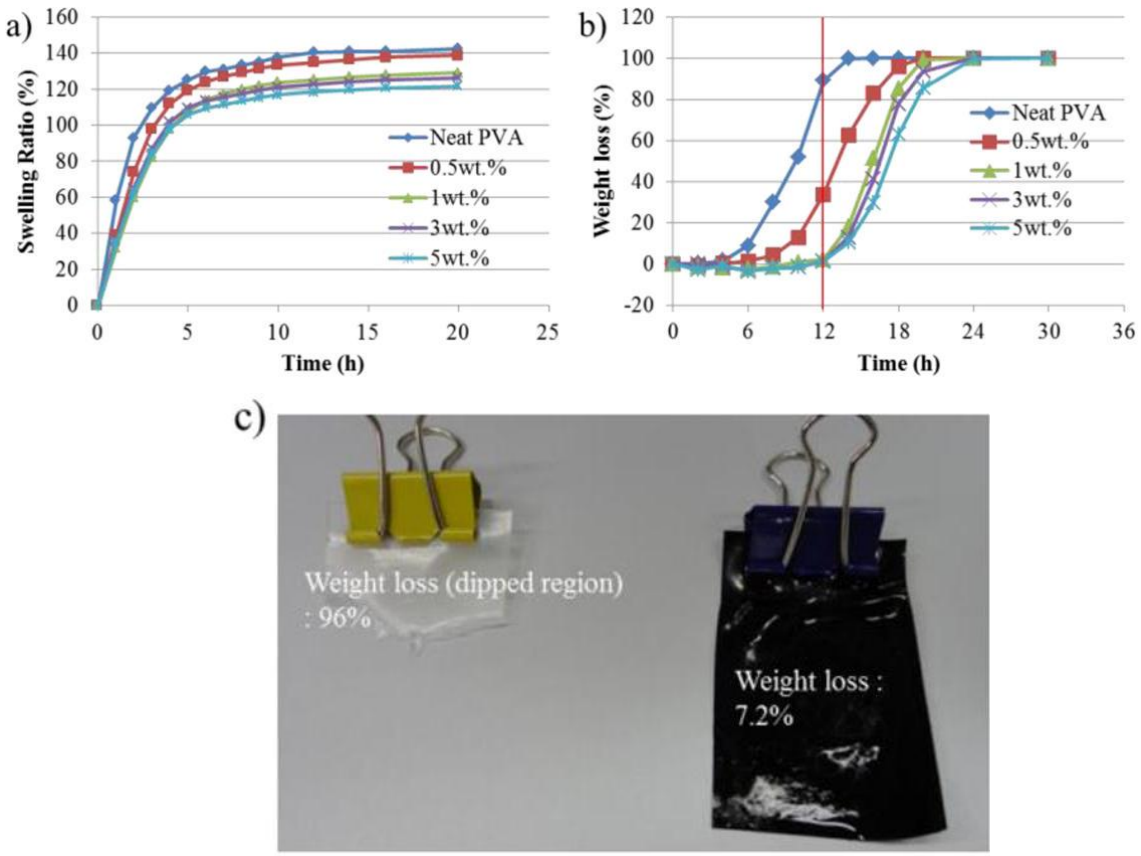

Figure 8. (a) Swelling ratio, (b) weight losses measured from water-dipping tests performed on dried dGO/PVA (poly(dopamine):GO = 0.5:1) composite films with various GO contents. (c) Optical photograph shows difference in weight loss between neat PVA and dGO/PVA films after 12 h of dipping in water at room temperature.

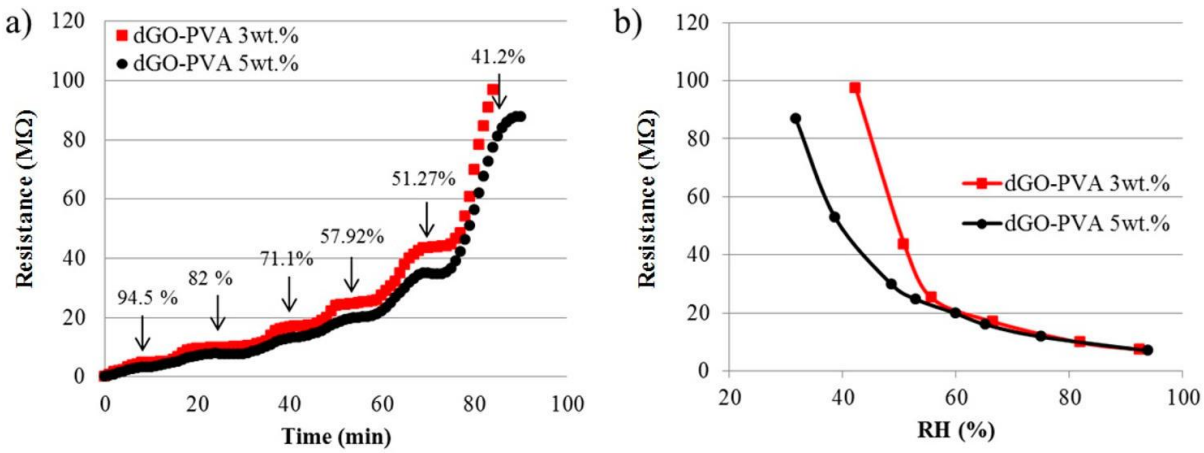

Figure 9. Variation of resistance with respect to (a) stepwise dehumidification and (b) linear humidification for different dGO loadings.

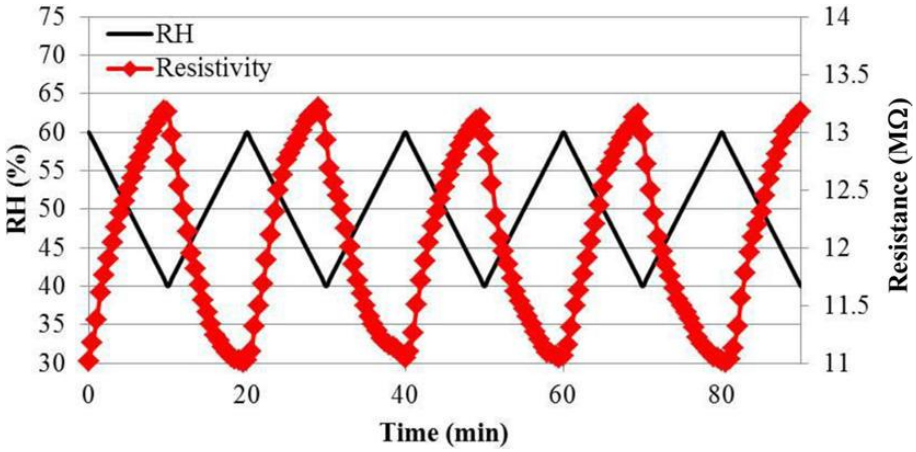

Figure 10. Resistance reversibility in the response of a 5 wt % dGO/PVA film at 30 °C.

and enables dGO/PVA composite films to be used as robust, cost-effective, easy-to-use humidity sensors over the relative humidity range of 40-100%. It was shown that the dGO concentration in PVA, which governs proton generation, can serve as an effective parameter to control the moisture sensitivity and that the composite films are robust under cyclic humidification-dehumidification conditions. Although PVA is a water-soluble polymer and, therefore, its detectable humidity range is quite narrow, the addition of a small amount of dGO, which acts as an effective moisture barrier, can extend the sensing range significantly, prolong the continuous sensing time, and improve the physical stability with a reduction in moisture-induced aging.

5. References

1. Kuilla, T.; Bhadra, S.; Yao, D.; Kim, N. H.; Bose, S.; Lee, J. H., Recent advances in graphene based polymer composites. *Progress in Polymer Science* **2010,** *35* (11), 1350-1375.
2. Hussain, F.; Hojjati, M.; Okamoto, M.; Gorga, R. E., Review article: polymer-matrix nanocomposites, processing, manufacturing, and application: an overview. *Journal of composite materials* **2006,** *40* (17), 1511-1575.
3. Breuer, O.; Sundararaj, U., Big returns from small fibers: a review of polymer/carbon nanotube composites. *Polymer Composites* **2004,** *25* (6), 630-645.
4. Kotov, N. A., Materials science: carbon sheet solutions. *Nature* **2006,** *442* (7100), 254-255.
5. Avouris, P.; Chen, Z.; Perebeinos, V., Carbon-based electronics. *Nature Nanotechnology* **2007,** *2* (10), 605-615.
6. Dikin, D. A.; Stankovich, S.; Zimney, E. J.; Piner, R. D.; Dommett, G. H.; Evmenenko, G.; Nguyen, S. T.; Ruoff, R. S., Preparation and characterization of graphene oxide paper. *Nature* **2007,** *448* (7152), 457-460.
7. Novoselov, K. S.; Geim, A. K.; Morozov, S. V.; Jiang, D.; Zhang, Y.; Dubonos, S. V.; Grigorieva, I. V.; Firsov, A. A., Electric field effect in atomically thin carbon films. *science* **2004,** *306* (5696), 666-669.
8. Stankovich, S.; Dikin, D. A.; Dommett, G. H.; Kohlhaas, K. M.; Zimney, E. J.; Stach, E. A.; Piner, R. D.; Nguyen, S. T.; Ruoff, R. S., Graphene-based composite materials. *nature* **2006,** *442* (7100), 282-286.
9. Huang, X.; Qi, X.; Boey, F.; Zhang, H., Graphene-based composites. *Chemical Society Reviews* **2012,** *41* (2), 666-686.
10. Chen, D.; Feng, H.; Li, J., Graphene oxide: preparation, functionalization, and electrochemical applications. *Chemical reviews* **2012,** *112* (11), 6027-6053.
11. Green, A. A.; Hersam, M. C., Solution phase production of graphene with controlled thickness via density differentiation. *Nano Letters* **2009,** *9* (12), 4031-4036.
12. Boukhvalov, D.; Katsnelson, M., Chemical functionalization of graphene. *Journal of Physics: Condensed Matter* **2009,** *21* (34), 344205.
13. Tang, L.; Li, X.; Ji, R.; Teng, K. S.; Tai, G.; Ye, J.; Wei, C.; Lau, S. P., Bottom-up synthesis of large-scale graphene oxide nanosheets. *Journal of Materials Chemistry* **2012,** *22* (12), 5676-5683.
14. Kim, J.; Cote, L. J.; Kim, F.; Yuan, W.; Shull, K. R.; Huang, J., Graphene oxide sheets at interfaces. *Journal of the American Chemical Society* **2010,** *132* (23), 8180-8186.
15. Sahoo, N. G.; Rana, S.; Cho, J. W.; Li, L.; Chan, S. H., Polymer nanocomposites based on functionalized carbon nanotubes. *Progress in Polymer Science* **2010,** *35* (7), 837-867.
16. Song, Y. S.; Youn, J. R., Influence of dispersion states of carbon nanotubes on physical properties

of epoxy nanocomposites. *Carbon* **2005,** *43* (7), 1378-1385.

17. Zhao, J.; Morgan, A. B.; Harris, J. D., Rheological characterization of polystyrene–clay nanocomposites to compare the degree of exfoliation and dispersion. *Polymer* **2005,** *46* (20), 8641-8660.
18. Gojny, F.; Wichmann, M.; Köpke, U.; Fiedler, B.; Schulte, K., Carbon nanotube-reinforced epoxy-composites: enhanced stiffness and fracture toughness at low nanotube content. *Composites Science and Technology* **2004,** *64* (15), 2363-2371.
19. Pan, Y. X.; Yu, Z. Z.; Ou, Y. C.; Hu, G. H., A new process of fabricating electrically conducting nylon 6/graphite nanocomposites via intercalation polymerization. *Journal of Polymer Science Part B: Polymer Physics* **2000,** *38* (12), 1626-1633.
20. Wakabayashi, K.; Pierre, C.; Dikin, D. A.; Ruoff, R. S.; Ramanathan, T.; Brinson, L. C.; Torkelson, J. M., Polymer-graphite nanocomposites: effective dispersion and major property enhancement via solid-state shear pulverization. *Macromolecules* **2008,** *41* (6), 1905-1908.
21. Kalaitzidou, K.; Fukushima, H.; Drzal, L. T., Mechanical properties and morphological characterization of exfoliated graphite–polypropylene nanocomposites. *Composites Part A: Applied Science and Manufacturing* **2007,** *38* (7), 1675-1682.
22. Kalaitzidou, K.; Fukushima, H.; Drzal, L. T., A new compounding method for exfoliated graphite–polypropylene nanocomposites with enhanced flexural properties and lower percolation threshold. *Composites Science and Technology* **2007,** *67* (10), 2045-2051.
23. Wang, W. p.; Liu, Y.; Li, X. x.; You, Y. z., Synthesis and characteristics of poly (methyl methacrylate)/expanded graphite nanocomposites. *Journal of Applied Polymer Science* **2006,** *100* (2), 1427-1431.
24. Zheng, W.; Wong, S.-C., Electrical conductivity and dielectric properties of PMMA/expanded graphite composites. *Composites Science and Technology* **2003,** *63* (2), 225-235.
25. Yasmin, A.; Luo, J.-J.; Daniel, I. M., Processing of expanded graphite reinforced polymer nanocomposites. *Composites Science and Technology* **2006,** *66* (9), 1182-1189.
26. Ramanathan, T.; Abdala, A.; Stankovich, S.; Dikin, D.; Herrera-Alonso, M.; Piner, R.; Adamson, D.; Schniepp, H.; Chen, X.; Ruoff, R., Functionalized graphene sheets for polymer nanocomposites. *Nature Nanotechnology* **2008,** *3* (6), 327-331.
27. Wang, J.; Wang, X.; Xu, C.; Zhang, M.; Shang, X., Preparation of graphene/poly (vinyl alcohol) nanocomposites with enhanced mechanical properties and water resistance. *Polymer International* **2011,** *60* (5), 816-822.
28. Zhang, L.; Wang, Z.; Xu, C.; Li, Y.; Gao, J.; Wang, W.; Liu, Y., High strength graphene oxide/polyvinyl alcohol composite hydrogels. *Journal of Materials Chemistry* **2011,** *21* (28), 10399-10406.
29. Yang, L.; Phua, S. L.; Teo, J. K. H.; Toh, C. L.; Lau, S. K.; Ma, J.; Lu, X., A biomimetic approach

to enhancing interfacial interactions: polydopamine-coated clay as reinforcement for epoxy resin. *ACS Applied Materials & Interfaces* **2011,** *3* (8), 3026-3032.

30. Lee, H.; Scherer, N. F.; Messersmith, P. B., Single-molecule mechanics of mussel adhesion. *Proceedings of the National Academy of Sciences* **2006,** *103* (35), 12999-13003.
31. Lee, H.; Dellatore, S. M.; Miller, W. M.; Messersmith, P. B., Mussel-inspired surface chemistry for multifunctional coatings. *science* **2007,** *318* (5849), 426-430.
32. Kang, S. M.; Park, S.; Kim, D.; Park, S. Y.; Ruoff, R. S.; Lee, H., Simultaneous Reduction and Surface Functionalization of Graphene Oxide by Mussel-Inspired Chemistry. *Advanced Functional Materials* **2011,** *21* (1), 108-112.
33. Shin, M.; Kim, H. K.; Lee, H., Dopamine-loaded poly (D,L-lactic-co-glycolic acid) microspheres: New strategy for encapsulating small hydrophilic drugs with high efficiency. *Biotechnology Progress* **2014,** *30* (1), 215-223.
34. Ryu, S.; Lee, Y.; Hwang, J. W.; Hong, S.; Kim, C.; Park, T. G.; Lee, H.; Hong, S. H., High-strength carbon nanotube fibers fabricated by infiltration and curing of mussel-inspired catecholamine polymer. *Advanced Materials* **2011,** *23* (17), 1971-1975.
35. Yamaguchi, H.; Eda, G.; Mattevi, C.; Kim, H.; Chhowalla, M., Highly uniform 300 mm wafer-scale deposition of single and multilayered chemically derived graphene thin films. *ACS Nano* **2010,** *4* (1), 524-528.
36. Li, D.; Mueller, M. B.; Gilje, S.; Kaner, R. B.; Wallace, G. G., Processable aqueous dispersions of graphene nanosheets. *Nature Nanotechnology* **2008,** *3* (2), 101-105.
37. Kong, J.; Yee, W. A.; Yang, L.; Wei, Y.; Phua, S. L.; Ong, H. G.; Ang, J. M.; Li, X.; Lu, X., Highly electrically conductive layered carbon derived from polydopamine and its functions in SnO_2-based lithium ion battery anodes. *Chemical Communications* **2012,** *48* (83), 10316-10318.
38. Guo, L.; Liu, Q.; Li, G.; Shi, J.; Liu, J.; Wang, T.; Jiang, G., A mussel-inspired polydopamine coating as a versatile platform for the in situ synthesis of graphene-based nanocomposites. *Nanoscale* **2012,** *4* (19), 5864-5867.
39. Dreyer, D. R.; Miller, D. J.; Freeman, B. D.; Paul, D. R.; Bielawski, C. W., Elucidating the structure of poly(dopamine). *Langmuir* **2012,** *28* (15), 6428-6435.
40. d'Ischia, M.; Napolitano, A.; Pezzella, A.; Meredith, P.; Sarna, T., Chemical and Structural Diversity in Eumelanins: Unexplored Bio-Optoelectronic Materials. *Angewandte Chemie International Edition* **2009,** *48* (22), 3914-3921.
41. Paredes, J.; Villar-Rodil, S.; Martínez-Alonso, A.; Tascon, J., Graphene oxide dispersions in organic solvents. *Langmuir* **2008,** *24* (19), 10560-10564.
42. Centeno, S. A.; Shamir, J., Surface enhanced Raman scattering (SERS) and FTIR characterization of the sepia melanin pigment used in works of art. *Journal of Molecular Structure* **2008,** *873* (1), 149-159.

43. Zhao, X.; Zhang, Q.; Chen, D.; Lu, P., Enhanced mechanical properties of graphene-based poly(vinyl alcohol) composites. *Macromolecules* **2010,** *43* (5), 2357-2363.
44. Wang, H.; Feng, C.-D.; Sun, S.-L.; Segre, C. U.; Stetter, J. R., Comparison of conductometric humidity-sensing polymers. *Sensors and Actuators B: Chemical* **1997,** *40* (2), 211-216.
45. Li, Y.; Ying, B.; Hong, L.; Yang, M., Water-soluble polyaniline and its composite with poly (vinyl alcohol) for humidity sensing. *Synthetic Metals* **2010,** *160* (5), 455-461.
46. Fuke, M. V.; Adhyapak, P.; Mulik, U.; Amalnerkar, D.; Aiyer, R., Electrical and humidity characterization of m-NA doped Au/PVA nanocomposites. *Talanta* **2009,** *78* (2), 590-595.
47. Barkauskas, J., Investigation of conductometric humidity sensors. *Talanta* **1997,** *44* (6), 1107-1112.
48. Yang, M.-R.; Chen, K.-S., Humidity sensors using polyvinyl alcohol mixed with electrolytes. *Sensors and Actuators B: Chemical* **1998,** *49* (3), 240-247.

Chapter 3: Mechanical properties of poly(dopamine)-coated graphene oxide and poly(vinyl alcohol) composite fibers coated with reduced graphene oxide and their use for piezoresistive sensing

1. Introduction

Many attempts have been made to develop high strength polymer composite fibers that are reinforced using carbon-based nanofillers. Currently, although high-strength composite fibers using carbon-based materials are dominated by carbon nanotubes (CNT), the intrinsic aggregation by inter-tubular interactions,[1-5] impurities from catalysts, and high cost have been hampering their application. Theoretical and experimental studies show that monolayer graphene is the strongest material developed thus far.[6-7] Due to its extraordinary mechanical properties, composite materials based on graphene derivatives like graphene oxide (GO) and graphite nanoplatelets have recently attracted tremendous attentions.[8-10]

Pristine graphene, *i.e.* prepared by exfoliation of graphite or growth by chemical vapor deposition (CVD), does not produce strong interactions with polymer because of its chemical inertness. In order to facilitate good interactions between graphene and polymer matrices, chemical modification or surface functionalization of graphene has been widely developed.[11-13] Chemically converted graphene can be produced from GO, which is prepared by oxidative exfoliation of graphite.[14-16] GO possesses oxygen-containing functional groups including hydroxyls, epoxides, diols, ketones, and carboxyls on the edge side and basal plane of graphene; thus GO exhibits hydrophilic properties.[17] Therefore, aqueous processing for the fabrication of reinforced polymer composite materials can readily achieve the dispersion of GO. Moreover, functional groups on GO sheets can improve interfacial bonding between the GO and polymer matrix, as has been reported for functionalized CNT-based composite materials.[4, 18-20] Specifically, oxygen-containing functional groups of GO have been reported as a suitable component for composite materials with polar polymers such as poly(methyl methacrylate) (PMMA), polyacrylonitrile (PAN), poly(acrylic acid) (PAA), and poly(vinyl alcohol) (PVA).[21] Among these polymers, PVA is widely used to fabricate films for food and drug packages and gas barrier membranes due to its non-toxicity and high resistance to gas permeability.[22-23] In addition, PVA fibers are considered as one of the most suitable polymeric fibers for the reinforcement of engineered cementitious composites (ECC) because of their good fiber-forming ability and outstanding mechanical properties.[24-25] PVA, in combination with GO, may be an effective means of producing high performance polymer composite materials because of the abundant hydroxyl groups and water dispersivity. From theoretical results, it has been estimated that the elastic modulus of perfectly aligned PVA chains could reach up to 250 GPa,[26] which has the potential to produce a high performance composite fiber in terms of the resulting mechanical properties. On the basis of this theoretical rationale, the mechanical properties of PVA/GO composite fibers have been experimentally explored. Wang *et al.* reported PVA/GO composite fibers by electrospinning, and

found that a small loading of 0.02 wt% GO increased the tensile strength of fibers from 0.22 MPa to 9.37 MPa.[27] Reduced graphene oxide (rGO) has been also used for high strength PVA fibers. Li et al. reported the fabrication of a reinforced PVA composite fiber with rGO, and the tensile strength of the 2.0 wt% rGO composite fiber was increased to 244 % that of the neat PVA fiber.[28] Li *et al.* have successfully fabricated meter-long scale PVA/rGO fibers by gel spinning, which allows the fibers to reach a high extension with fewer chain entanglements and a high degree of chain alignment. The tensile strength of this PVA/rGO composite fiber was increased by 20.9%, from 1.8 to 2.2 GPa.[29] Tan *et al.* reported the effect of loading and reduction time of rGO, and their results revealed that the 1 wt% of GO/rGO mixture, in which GO was were used as a surfactant-like role, significantly improved the fibrous uniformity and thermal stability of the PVA composite fiber.[30] Despite previous research efforts, a method for making high strength PVA/GO composite fibers by controlling the interfacial interaction between GO and PVA remains a great challenge.

Mussel-inspired strong protein-based adhesives, *i.e.,* dopamine, provide a new insight into the development of a molecular binder. Dopamine, which is a small molecule containing catechol-amine groups, is a hormone and neurotransmitter, and its polymerized form, known as poly(dopamine), is similar to the adhesive proteins of mussels.[31-32] It has excellent adhesion with many organic and inorganic surfaces, such as metals, metal oxides, and polymer surfaces.[31] Moreover, dopamine has been used to enhance both mechanical and electrical properties of GO during its polymerization on the GO surface.[33-34] According to a previous study, a single molecule of 3,4-dihydroxy-L-phenylalanine (DOPA) has higher adhesion force than the covalent bonding force.[32] Therefore, its polymerized form can provide a good adhesion force on GO sheets. Employing such excellent adhesive properties, poly(dopamine)-coated GO can be used as an effective mechanical reinforcing nanofiller for high-strength polymer composite fibers.

In this work, we fabricated high strength PVA composite fibers with poly(dopamine)-coated GO (dGO) through gel spinning. The PVA/dGO composite fibers showed significant enhancement in mechanical properties because of increased interfacial interactions between PVA and dGO formed by strong hydrogen bonding of poly(dopamine) layers. Moreover, the effect of GO sheet size on the mechanical properties of PVA composite fibers was systematically investigated. We also demonstrate that exterior rGO coatings can complement the mechanical strength on PVA/dGO composite fibers by providing additional interfacial shear strength (ISS) from rGO sheets. To demonstrate their feasibility as strain sensor, fabricated rGO-coated PVA/dGO fibers were subjected to characterizations for their piezo-resistive sensitivity.

2. Experimental section

2.1. Materials

Graphite (SP-1, Baycarbon), H_2SO_4 (98 %, Merck), $KMnO_4$ (99 %, Sigma), dopamine hydrochloride (98.5 %, Sigma), dimethyl sulfoxide (DMSO, 99.9 %, Acros Organics) and poly(vinyl alcohol) (PVA, MW 89000-98000, 99 % hydrolyzed, Aldrich) were used as received without further purification.

2.2. Preparation of size-controlled GO sheets.

Graphite oxide was prepared from purified natural graphite (SP-1, Bay Carbon) using the modified Hummers method.[35] Graphite powder (2.0 g) was added to concentrated H_2SO_4 (46 mL), and $KMnO_4$ (6.0 g) was added gradually with stirring and cooling, while the temperature of the mixture was maintained below 20 ^oC. The mixture was then stirred at 35 ^oC for 2 hr, and distilled water (92 mL) was added. After 15 min, the reaction was terminated by the addition of a large amount of distilled water (280 mL) and a 30 % H_2O_2 solution (5.0 mL), after which the color of the mixture changed from black to bright yellow. The mixture was centrifuged at 4000 rpm and washed with a 1:10 HCl solution (500 mL) in order to remove metal ions. The graphite oxide product was suspended in distilled water producing a viscous, brown dispersion, which was subjected to dialysis to completely remove metal ions and acids. To obtain the GO dispersion, the graphite oxide was exfoliated by ultrasonication (Sonic Dismembrator Model 500, Fisher Scientific) at 100 W for 15 min and then centrifugation at 4000 rpm for 10 min. GO sheets were produced with a range of sizes by further treatment with ultrasonication for 10 min at different output powers, ranging from 50 W to 350 W.

2.3. Preparation of dGO sheets.

50 mL of GO (0.6 mg/mL) suspension was tuned to a pH around 9.0 using a 1.0 M NaOH aqueous solution. Then, 0.3 mL of dopamine hydrochloride aqueous solution (10 mg/mL) was added to the GO suspension and the mixture was stirred over 2 hr at room temperature. Finally, the color of the solution turned to dark brown due to the pH-induced oxidative polymerization of dopamine hydrochloride and the reduction of GO.

2.4. Fabrication of rGO-coated PVA/dGO composite fibers.

The well-dispersed PVA/dGO spinning dope (GO loading = 0.1 wt%) was prepared as follows: 1.25 mg of dGO was dispersed in 11.25 g of DMSO/H_2O (a volume ratio of 4:1) and sonicated for 1 min in water to ensure a homogeneous dispersion. To obtain the PVA/dGO mixture, 1.25 g of PVA powder was slowly added into dGO/DMSO/H_2O dispersion, and the mixture was stirred with mild rotation at 90 ^oC, then deaerated in a vacuum desiccator for 1 hr prior to spinning. In this way, 10 wt% PVA/DMSO/H_2O solutions with 0.1 wt% dGO were prepared as spinning dope. The composite fibers were fabricated by wet spinning with a needle (Nano NC, inner diameter: 0.25 mm) and coagulation in methanol. The fibers were subsequently drawn at 150 ^oC with a ratio of 30.

rGO-coated PVA/dGO fibers were prepared by spray coating of with an rGO solution. The rGO solution was obtained by reduction of GO solution using hydrazine, as described in detail elsewhere.[15] Prior to spraying, the rGO solution (0.5 mg/mL) was diluted with the same volume of ethanol. A commercial airbrush gun (Hyup Sung W-33 spray gun) was used to uniformly spray the rGO solution onto PVA/dGO fibers. The fibers were kept at elevated temperature to assist evaporation of sprayed solution, and a surface temperature of 160 ^{o}C was chosen in order to avoid melting the polymer fiber. A typical spray distance was about 15 cm and the optimal volume of sprayed rGO solution was 30 mL for the full coverage.

2.5. Characterizations.

The morphology of the GO and dGO sheets, and the surface of the rGO-coated PVA/dGO fibers were analyzed using atomic force microscopy (AFM, Veeco Dimension 3100) and scanning electron microscopy (SEM, FEI VERIOS 460). Raman spectra were measured using an Alpha 300 micro Raman spectrometer (WItec) equipped with a 532 nm laser. Infrared spectra characterizations were performed at ambient temperature with a FTIR microscope and spectrometer (Agilent Cary 600 series). Chemical structures of GO and dGO were identified by X-ray photoelectron spectroscopy (XPS) using ESCALAB 250Xi (Thermo Scientific) equipped with a monochromatic Al K-Alpha source. Tensile properties, including modulus, strength, and strain-to-failure ratio, of composite fibers were measured using a dynamical mechanical analyzer (DMA Q800, TA Instruments) with an initial length of specimens of 10 mm. Tensile tests were performed until the specimens ruptured. Load and elongation were measured simultaneously.

To assess the potential feasibility of rGO-coated PVA/dGO composite fibers as strain sensors, the electrical response as a function of the strain rate was measured. Copper electrodes were connected to each end of the rGO-coated PVA/dGO fiber with the help of silver paste and the electrical properties of the fiber were verified by a source meter (S-2400, Keithley).

3. Results and discussion

The graphene oxide (GO) used in this work was prepared from the oxidative exfoliation of graphite by the modified Hummers method, as described our previous work.[35-36] GO sheets were prepared with different exfoliation conditions, sonication output powers ranging from 50 W to 350 W, prior to making poly(dopamine)-coated GO (dGO) and its composite fibers. By changing the ultrasonication output power, it is possible to control the size of sheets, which were characterized using scanning electron microscopy (SEM) and atomic force microscopy (AFM). Although GO sheets were prepared by different exfoliation conditions, all GO sheets were well dispersed in a single layer (Figure 1). The average lateral size of the initial GO (GO1) was ~2.29 μm. The average lateral size

of GO decreased to 1.20 μm (GO2) after 10 minutes of treatment at 50 W, to ~0.71 μm (GO3) at 150 W, to ~0.41 μm (GO4) at 250 W, and finally to ~0.29 μm (GO5) at 350 W. The size of dGO sheets (dGO1-5) also showed the same value after the poly(dopamine) coating (Figure 2(a and b)). The AFM analysis confirms the morphology and thickness of GO and dGO sheets. The thickness of GO1 sheets were around 1.09 nm, which is thicker than pristine graphene due to the functional groups on the graphene surface produced by the oxidation process. Although the average sheet size was decreased during the sonication treatment, the thickness was not changed (Figure 1(c and d)). On the other hand, the average thickness of dGO was around 2.31 nm, indicating that the increase in thickness by 1.22 nm is due to the presence of poly(dopamine) on the GO sheets. It is well known that polymerized catecholamine, such as poly(dopamine) and poly(norepinephrine), has an interconnected layered structure with a graphite-like stacking spacing of 3.4-3.8 Å.[37-38] Therefore, the 1.22 nm thickness of poly(dopamine) is consistent with 3-4 layers. Note that while the average lateral size of dGO sheets were changed by sonication treatment, the thickness difference between dGO1 and dGO5 is negligible (Figure 2(e and f)).

Further characterizations by X-ray photoelectron spectroscopy (XPS) and Fourier transform infrared (FT–IR) spectroscopy were performed to investigate surface functionalization and the chemical structure of GO and dGO. XPS spectra of GO and dGO, shown in Figure 3(a), reveal that the N 1s peak at 398 eV is observed only in the dGO sample. The N 1s peak originates from amine groups of poly(dopamine) layers on GO sheets. The reduction of GO was also probed by XPS analysis. In Figure 2(b), a significant decrease of the XPS signal at 286–289 eV, which corresponds to C–O and C=O groups, indicates the simultaneous reduction and surface functionalization of GO by the polymerization of dopamine. In fact, it has been shown previously that GO can be reduced by released electrons during oxidative polymerization of catecholamine, such as dopamine and norepinephrine.[33-34] FT-IR was employed to analyze the presence of poly(dopamine) and the reduction of GO, as shown in Figure 3(c-d). The typical FT-IR spectrum of GO shows the O-H stretching vibrations in the region of 3,000 to 3,400 cm^{-1}, C=O stretching vibrations from carbonyl and carboxylic groups at 1,725 cm^{-1}, skeletal vibrations from unoxidized graphitic domains at 1,620 cm^{-1} and C-O stretching vibrations at 1,040 cm^{-1}. On the other hand, the FT-IR spectrum of the dGO sample shows a newly developed peak at 1,508 cm^{-1}, corresponding to the N-H bending mode of the aromatic secondary amine in dGO. These results confirms that the poly(dopamine) on the GO sheets possesses aromatic, nitrogenous species, such as the indole- or indoline-type structures widely proposed in poly(dopamine) and eumelanins.[37] Note that the region between 3,000 and 3,400 cm^{-1} could not be used to identify the N-H stretching mode of secondary amine due to the broad absorption band in the region, possibly caused by strong hydrogen bonds between poly(dopamine) and oxygen-containing groups in the GO sheets.

Figure 4(a) depicts a schematic illustration of the proposed structure of rGO-coated PVA/dGO fiber.

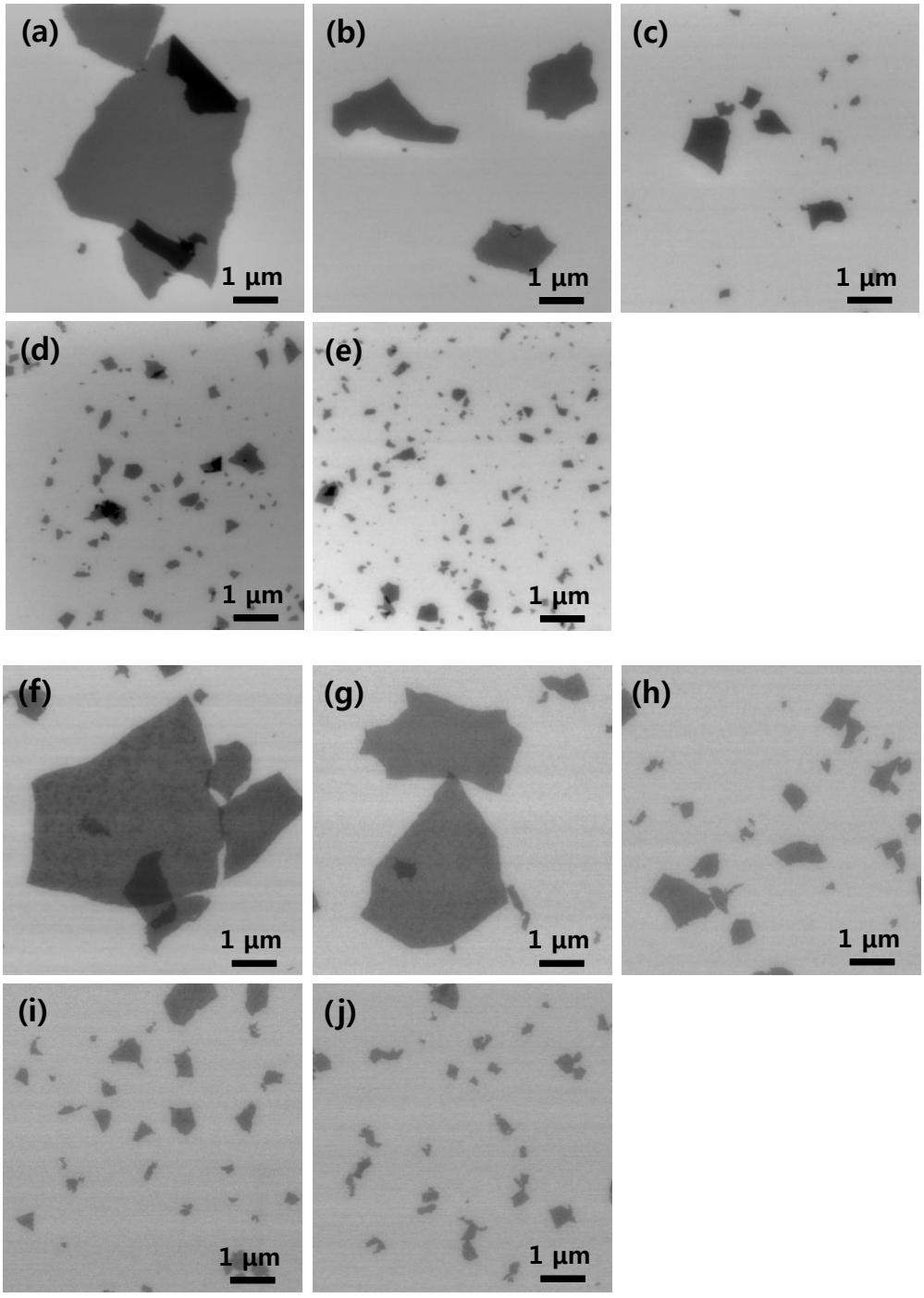

Figure 1. SEM images of GO1-5 (a-e) and dGO1-5 (f-j) sheets exfoliated at different sonication output power from 50 W to 350 W.

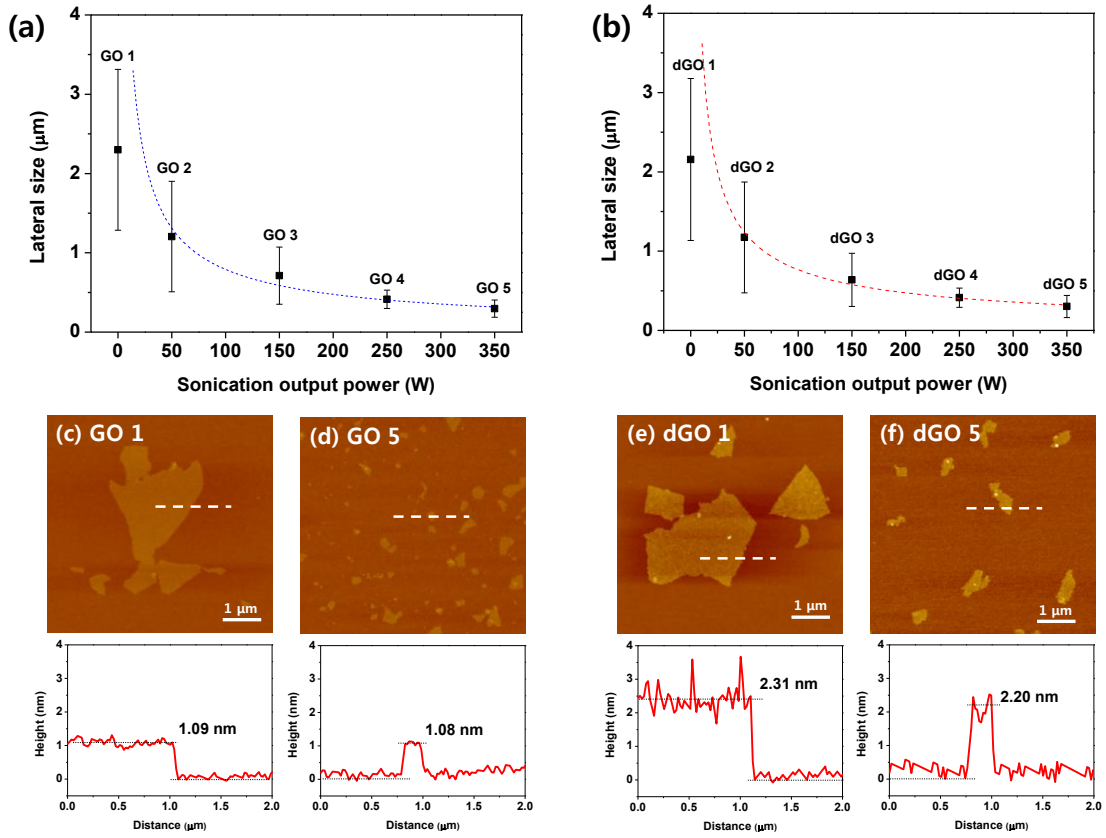

Figure 2. (a and b) Mean size of the GO and dGO sheets as a function of sonication output power, determined from SEM images. Each sample was designated as GO1, GO2, GO3, GO4 and GO5. AFM images and height profile of (c and d) GO and (e and f) dGO (GO/dopamine = 1:0.5). Samples were spin-coated on a Si wafer for AFM measurements.

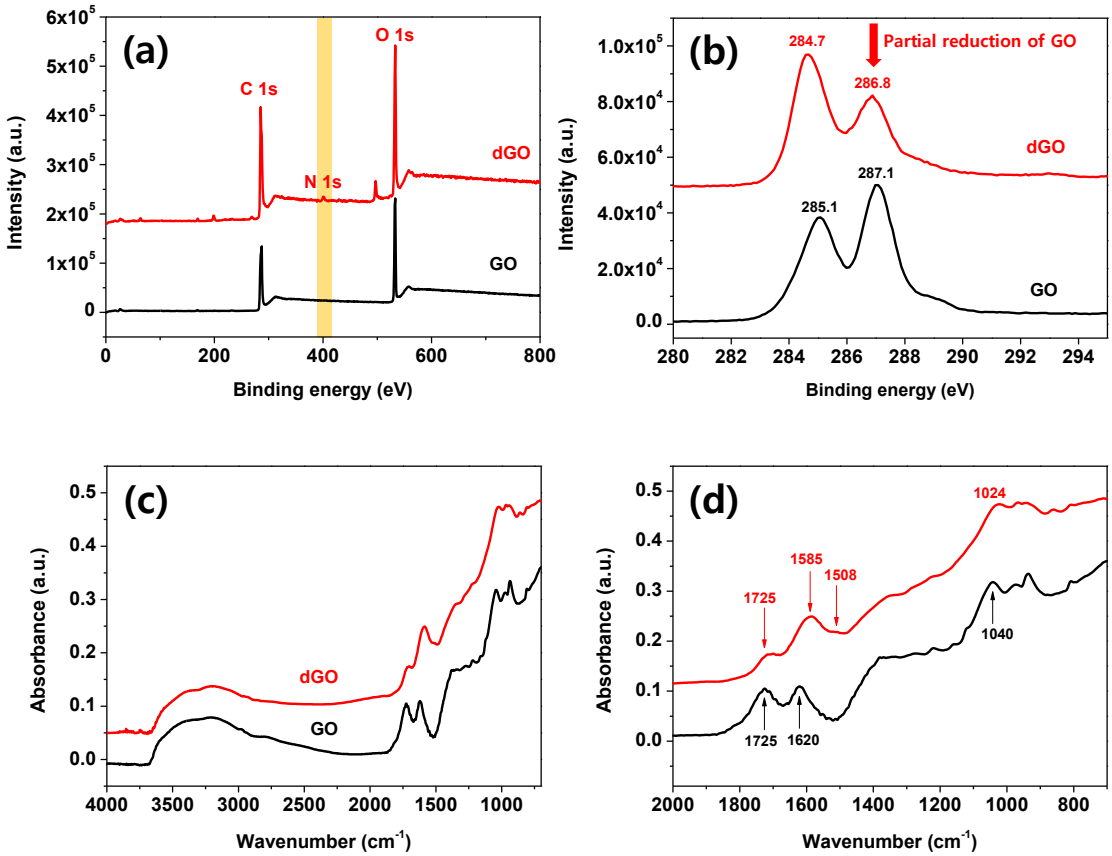

Figure 3. (a and b) XPS survey spectra, C 1s binding energy region, (c and d) ATR FT-IR spectra and magnified wavenumber range from 2,000 to 700 cm^{-1} spectra of GO (black) and dGO (red). For measurements, each solution was repeatedly coated on a Si wafer by drop casting. Additional Cl 2p and Na 1s Auger peaks in (a) originate from dopamine hydrochloride (HCl) and NaOH, which were used as the precursor of poly(dopamine) and pH tuning solution.

For gel spinning of PVA/dGO fiber, a mixture of DMSO/water (at a volume ratio of 4:1) and methanol were selected as solvent and coagulant, respectively, due to their frequent use in high strength PVA-based composite fiber.[3, 29, 39] The fabricated PVA/dGO fiber was subsequently coated by rGO layers through the spray coating method (see Experimental Section for details). The surface of the rGO-coated PVA/dGO fiber was examined by SEM, as shown in Figure 4(b and c). SEM images show that rGO layers prepared by the spray coating method on PVA/dGO fiber have a wrinkled morphology (Figure 4(c)). The capillary force generated by evaporation of solvent during the spray process can produce a confining force on rGO sheets. The confining force, when applied to rGO sheets, initially forms ridges that can grow until folds and wrinkles, and three-dimensional crumpled conformations are formed.[40] Figure 4(d) shows the Raman spectra of neat PVA, PVA/dGO and rGO-coated PVA/dGO fiber. The neat PVA has a distinct Raman peak at 2,908 cm^{-1} without any peaks in the range of 1,000–2,000 cm^{-1}. By comparison, the characteristic peaks at 1,342 and 1,588 cm^{-1} appear, corresponding to the D band and G band, for PVA/dGO and rGO-coated PVA/dGO. The D band and G band in the Raman spectrum of PVA/dGO originate from dGO sheets used as filler, while in the Raman spectrum of rGO-coated PVA/dGO, they came from the rGO layers on the outside.[41] The distinctive Raman peak of PVA at 2,908 cm^{-1} completely disappears in the rGO-coated PVA/dGO fiber, which means that it was fully covered by rGO sheets under this spray condition (30 mL of sprayed rGO solution was used). For the PVA/dGO fibers spray-coated with rGO solutions, with volumes ranging from 1 to 40 mL, the electrical resistance along the fiber axis was found to gradually decrease with an increase of rGO coating volume. The electrical resistance of rGO-coated PVA/dGO composite fiber decreased from 3.76×10^{6} to 2.01×10^{2} kΩ along with the sprayed volume of rGO solution from 1 to 40 mL (Figure 4(e), and Figure 5 for detailed measurements). Although the electrical resistance of 40 mL of rGO-coated PVA/dGO fiber was the lowest, 30 mL of rGO was chosen as the optimum sample preparation condition because the resulting fiber showed the highest mechanical properties in terms of tensile strength (Figure6).

We systemically evaluated the mechanical properties of neat PVA, PVA/GO, PVA/dGO and rGO-coated PVA/dGO composite fibers using dynamic mechanical analysis (DMA), and the stress-strain curves are displayed in Figure 7(a and b), with details of the results summarized in Tables 1 and 2. Compared with neat PVA fibers, the mechanical properties of PVA/GO composite fibers are improved. As shown in Figure 7(a), the mechanical properties of PVA/GO composite fibers increased and the maximum ultimate tensile strength and Young's modulus were 1.46 and 22.4 GPa, respectively, when GO sheets were exfoliated at 350 W (GO5 with smallest lateral size) and loading was 0.1 wt%. Compared to neat PVA fiber, improvements in tensile strength and Young's modulus by 55.3 % and 62.3 % were observed. Since PVA is a semicrystalline polymer, its mechanical properties strongly depend on the degree of its crystallinity.[10, 42-44] According to the results of XRD, distinctive differences were not found between neat PVA and PVA/GO composite fibers (Figure 8). Therefore, the enhanced

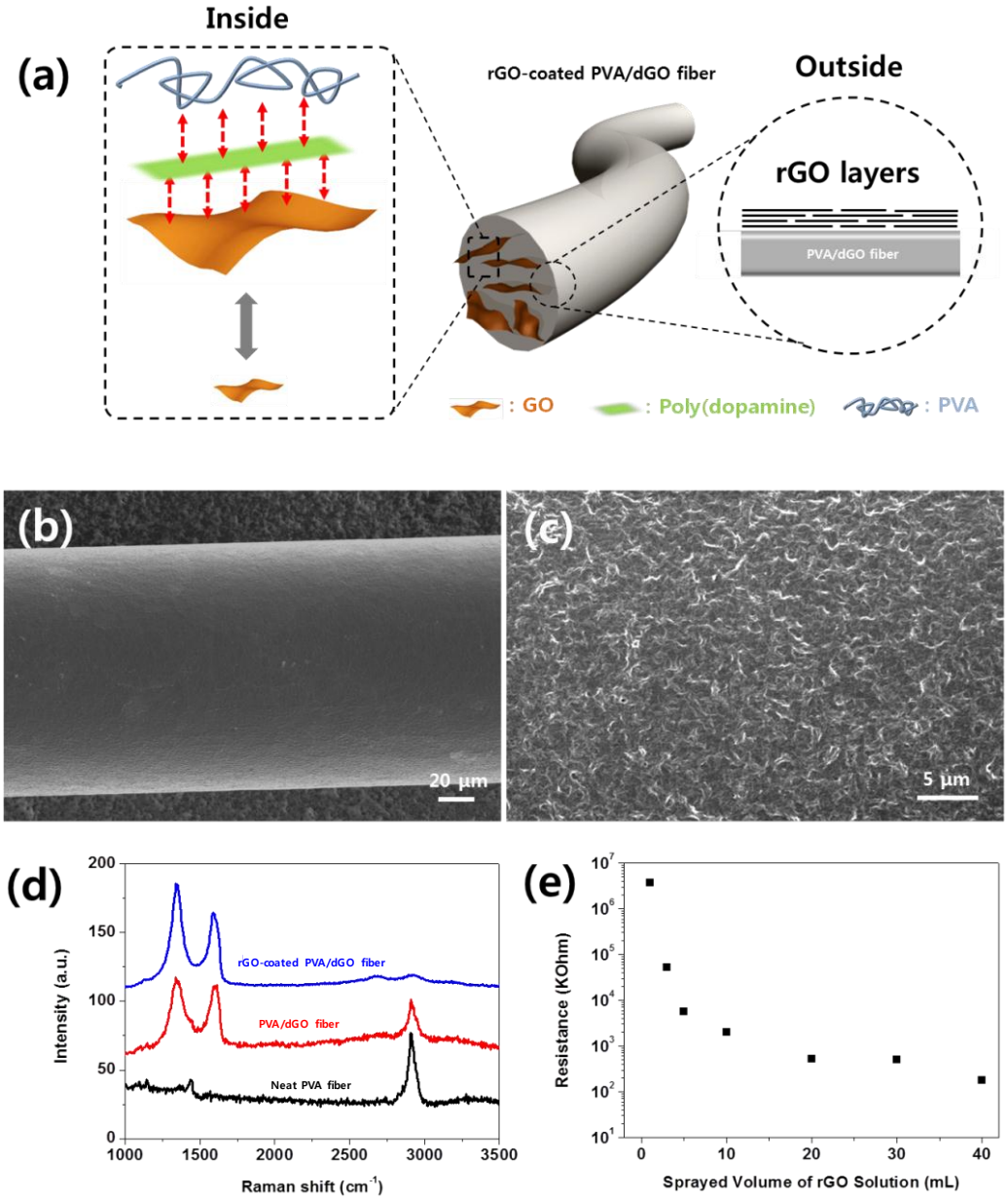

Figure 4. (a) Schematic illustration of rGO-coated PVA/dGO fiber. (b and c) SEM images of PVA/dGO fiber and magnified surface after rGO coating (with 30 mL of sprayed solution). (d) Micro-Raman spectra of neat PVA (black), PVA/dGO (red) and rGO-coated PVA/dGO (blue) fibers. (e) electrical resistance of rGO-coated PVA/dGO fibers at varying spray volumes of rGO solution.

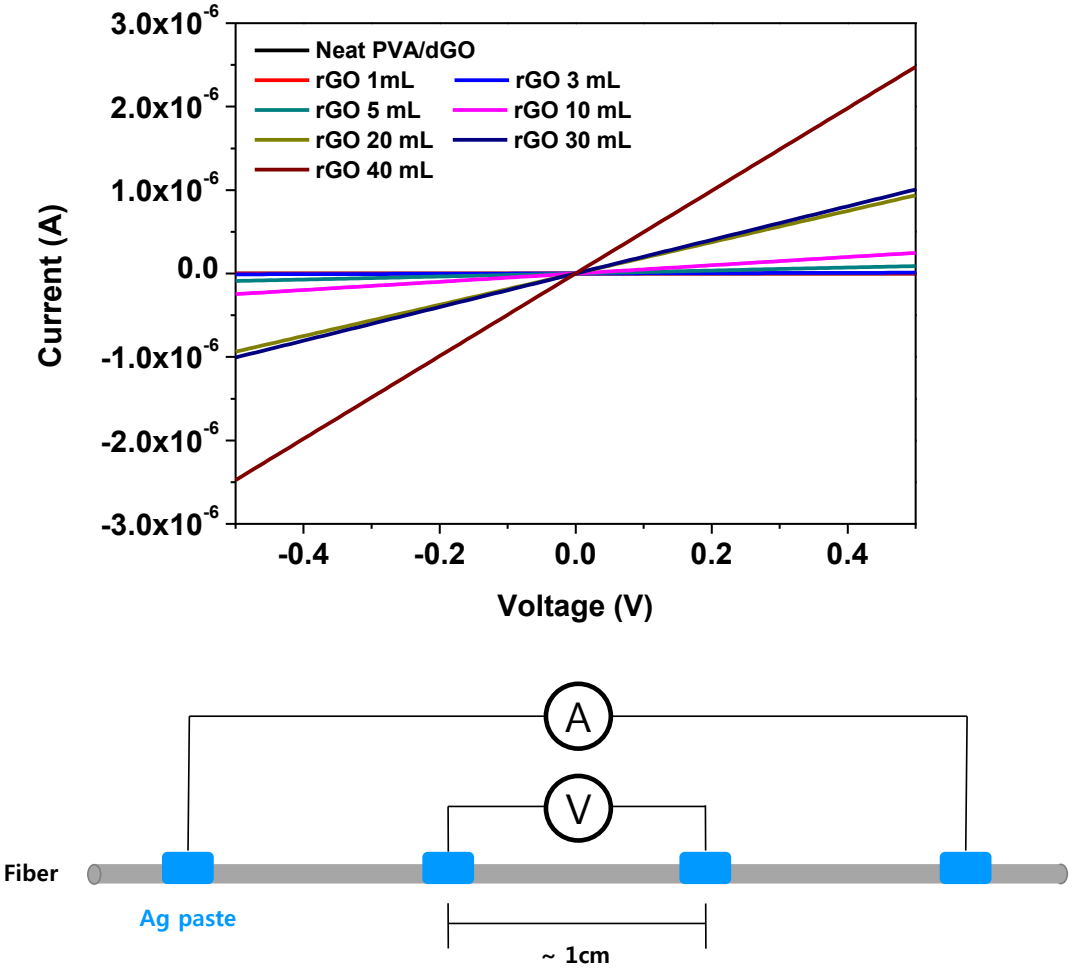

Figure 5. I-V curves of neat PVA/dGO and rGO-coated PVA/dGO fibers with different rGO coating volumes from 1 mL to 40 mL.

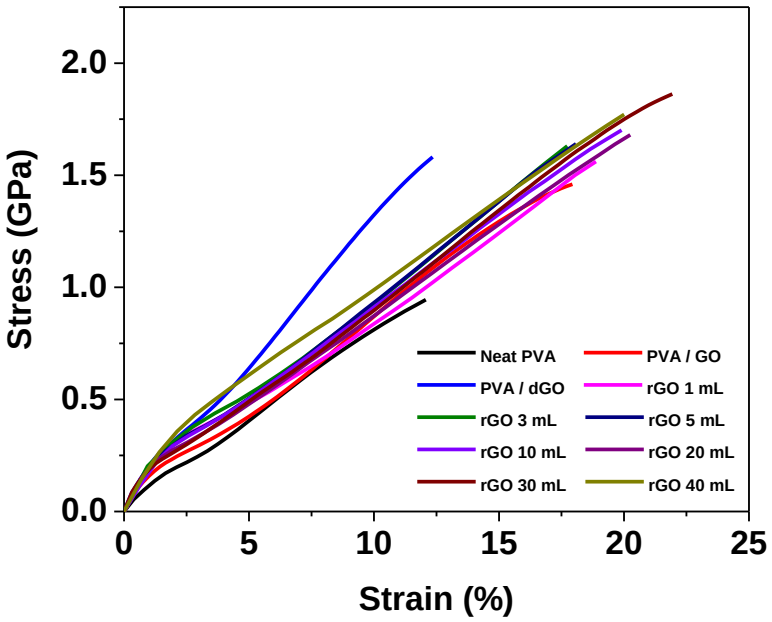

	E (GPa)	UTS (GPa)	Strain (%)	R (KOhm)
PVA	13.8	0.94	12.1	-
PVA / GO 5	22.4	1.46	17.9	
PVA / dGO 5	27.2	1.58	12.3	-
rGO 1 mL	26.6	1.56	18.9	3,672,388
3 mL	26.5	1.63	17.7	52,207
5 mL	25.4	1.64	18.1	5,540
10 mL	27.3	1.70	19.9	2,020
20 mL	26.1	1.72	20.3	533
30 mL	27.3	1.86	21.9	496
40 mL	26.8	1.77	20.0	201

Figure 6. Stress-strain curves of neat PVA, PVA/GO, PVA/dGO and rGO-coated PVA/dGO composite fibers with different rGO coating volume from 1 to 40 mL.

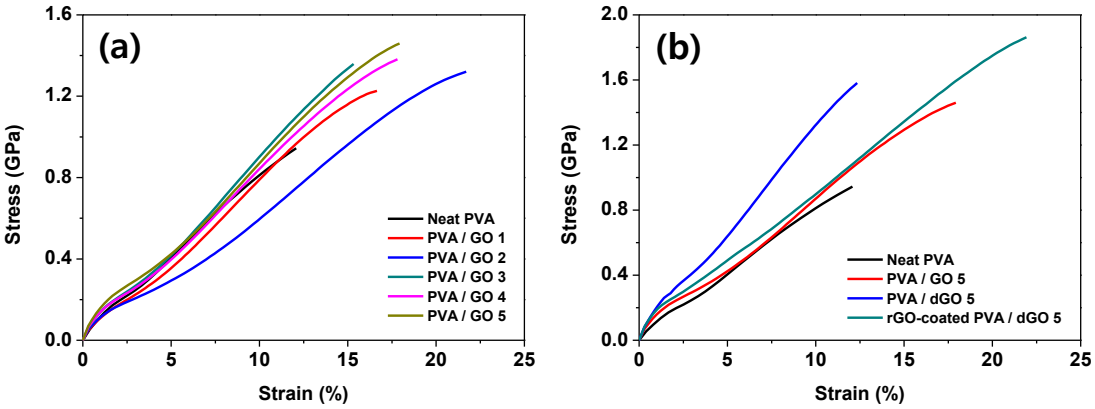

Figure 7. Stress-strain curves of (a) neat PVA and PVA/GO. For PVA/GO composite fibers, GO sheets were prepared with various sizes using different sonication output powers, from 0 (GO1) to 350 W (GO5). Stress-strain curves of (b) neat PVA, PVA/GO PVA/dGO and rGO-coated PVA/dGO composite fibers.

Table 1. Tensile properties of PVA/GO composite fibers at 0.1 wt% GO loading

	E (GPa)	UTS (GPa)	Strain (%)
Neat PVA	13.8	0.94	12.1
PVA / GO1	15.8	1.23	16.7
PVA / GO2	16.8	1.32	21.7
PVA / GO3	19.5	1.36	15.3
PVA / GO4	20.3	1.38	17.8
PVA / GO5	22.4	1.46	17.9

Table 2. Tensile properties of neat PVA, PVA/GO, PVA/dGO and rGO-coated PVA/dGO composite fibers

	E (GPa)	UTS (GPa)	Strain (%)
Neat PVA	13.8	0.94	12.1
PVA / GO5	22.4	1.46	17.9
PVA / dGO5	27.2	1.58	12.3
rGO-coated PVA / dGO5	27.3	1.86	21.9

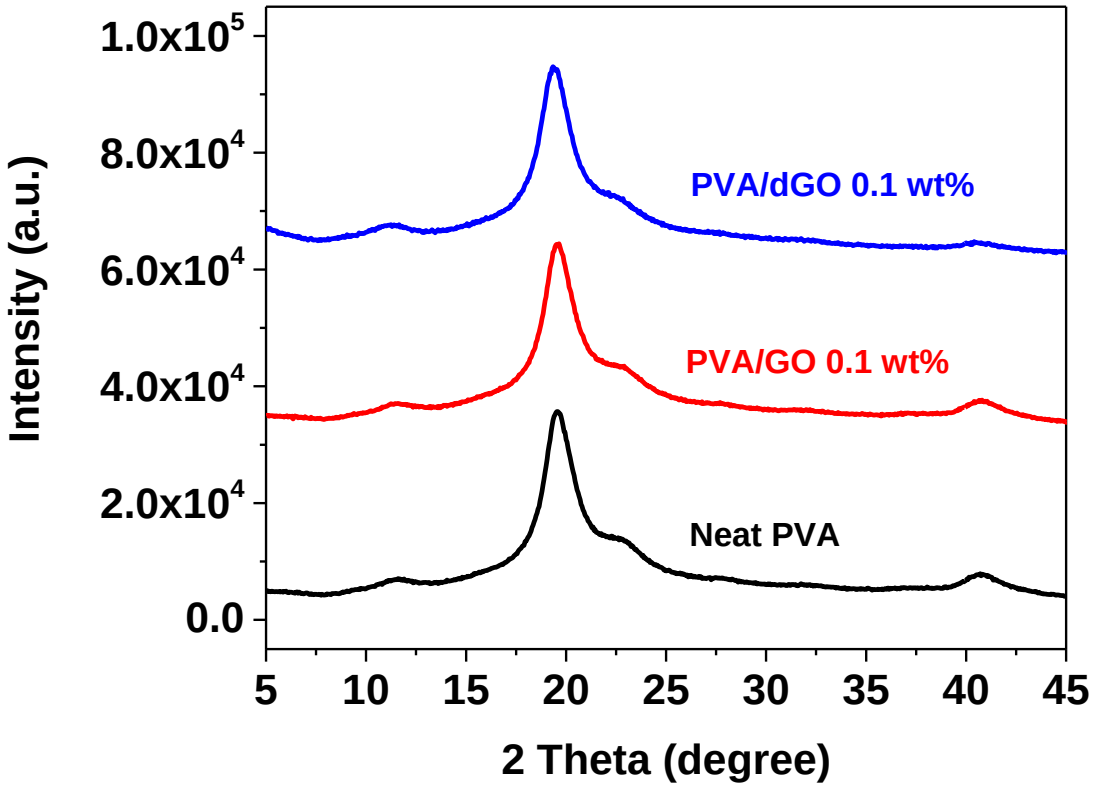

Figure 8. XRD spectra of neat PVA, PVA/GO and PVA/dGO (0.1 wt%) composite fibers.

mechanical properties of the PVA/GO composite fibers cannot be attributed to changes in crystallinity. They may be ascribed to the interfacial interaction between homogeneously dispersed GO sheets and PVA matrix. Figure 7(a) and Table 1 also show that the mechanical properties of PVA/GO fibers tended to increase with a decrease in the GO sheet size. As described in previous reports,[45-48] the mechanical properties, especially the strength, of the polymer composite materials depend on the size of the fillers. When the filler size becomes smaller, then it may significantly enhance the strength as well as modulus of the composite materials.[49] It has been proposed that the surface area of filler increases with a decrease in its size. Such an increase in the surface area causes an increase in the interaction between polymer matrix and filler. Therefore, the size reduction of the GO allowed for efficient stress transfer between the PVA matrix and GO, resulting in improved strength of the composite fiber. Unlike strength and modulus, the engineering strain of PVA composite fiber has a greater correlation with its diameter than filler size.[50] However, we were not able to find a correlation between the engineering strain and the size of the filler because the diameter of each fiber was not constant. The optimal content of GO was determined to be 0.1 wt% because the tensile strength of PVA composite fiber with GO 0.1 wt% increased from 0.94 to 1.46 GPa compared to neat PVA. However, as the GO loading went up to 0.3 wt%, the strength decrease to 1.05 GPa, which suggests agglomeration or inhomogeneous dispersion of GO sheets in the composite fibers (Figure 9).

The influence of interfacial adhesion of poly(dopamine) on the mechanical properties and the reinforcement with rGO coating layers were further studied, with the content of GO in PVA fixed at 0.1 wt%, and the results are shown in Figure 7(b) and summarized in Table 2. It is obvious that poly(dopamine) used as an adhesive layer has a significant influence on the mechanical properties. The ultimate tensile strength and Young's modulus of PVA/dGO5 fibers were 1.58 and 27.2 GPa, and 68.1% and 97.1% higher than neat PVA fiber. In addition, there was an 8.2% and 21.4% increase relative to that of PVA/GO5 composite fiber with same GO loading level, which implies that the adhesive characteristic of poly(dopamine) were effective in increasing the mechanical properties. Since the adhesion force of poly(dopamine) is based on strong hydrogen bonding from abundant amine and hydroxyl groups, it can provide a strong interfacial interaction between the GO and PVA matrix.[32, 34, 36] Note that the PVA/dGO5 composite fiber exhibited higher mechanical properties than PVA/dGO1 composite fiber, showing the same tendency as PVA/GO fibers. Moreover, the tensile strength of rGO-coated PVA/dGO composite fiber was increased as compared to that of the PVA/dGO fiber. The tensile strength of rGO-coated PVA/dGO was increased by 17.7 % from 1.58 to 1.86 GPa. We believe that the reinforcement was due to the additional interfacial shear strength (ISS) of exterior rGO layers.[51-52] Our results cannot be directly compared to other literature reports because the molecular weight and the diameter of the PVA fibers are different. Therefore, the relative increase has to be considered instead of absolute values. In this regard, our results show an excellent improvement, as summarized in Table 3.

The piezoresistive properties of rGO-coated PVA/dGO fiber were investigated by tracing the relative electrical resistance variation ($\Delta R/R_0$) under strain loading by maintaining constant voltage across the fiber. Figure 10(a) shows that $\Delta R/R_0$ of the rGO-coated PVA/dGO fiber gradually increased with increase in strain due to a disconnection between rGO sheets. The gauge factor, defined as $(\Delta R/R_0)/(\Delta L/L_0)$, where R is resistance and L is length of fiber under applied strain, implies an electrical sensitivity to strain, and the value for the rGO-coated PVA/dGO fiber was calculated to be 2.3 with a 1 % strain. Although rGO-coated PVA/dGO fibers showed a narrow strain range because of the inelastic characteristics of PVA, their sensitivity was compatible with strain sensors made of conventional metal ($(\Delta R/R_0)/(\Delta L/L_0) = 2.0$ under 5 % strain) and CNT film ($(\Delta R/R_0)/(\Delta L/L_0) = 0.82$ under 0-40 % strain).[53-54] Also, the immediate strain sensing response and strain detection limit of this fiber was determined by applying a gradually increasing step strain (Figure 10 (b)). Benefitting from the high sensitivity at small strain range, the detection limit could be as low as 0.2 %, accompanied by a superior long term stability (inset in Figure 10(b)). Moreover, the resistance variation and gauge factor were highly reproducible and coincident even after the 1,800th stretching, with a 1% strain (Figure 10(c)).

4. Conclusions

In conclusion, we fabricated high-strength PVA composite fiber by incorporating the use of poly(dopamine)-coated GO (dGO) as a filler and an exterior rGO coating on fibers. We found that the mechanical properties of PVA/dGO composite fibers were strongly dependent on the GO sheet size and interfacial adhesion force, which were generated by strong hydrogen bonding of poly(dopamine) layers. The mechanical properties of rGO-coated PVA/dGO fiber were much improved compared to that of PVA/dGO fiber, which indicates that the interfacial shear strength of rGO layers could provide additional tensile strength on PVA/dGO fiber. It was also demonstrated that rGO layers enables rGO-coated PVA/dGO fibers to offer piezoresistive sensitivity. The outstanding mechanical properties and piezoresistive sensitivity of rGO-coated PVA/dGO fibers demonstrate the great potential for use in the development of wearable strain sensors.

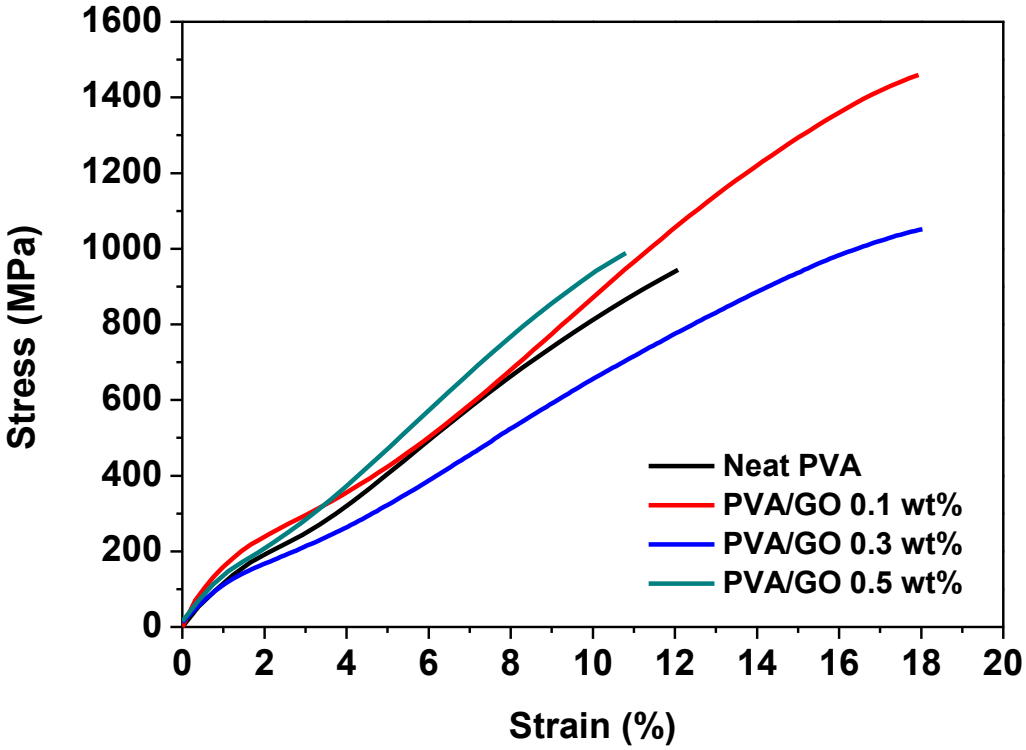

	E (GPa)	UTS (GPa)	Strain (%)
PVA	13.8	0.94	12.1
PVA / GO 0.1 wt%	22.4	1.46	17.9
PVA / GO 0.3 wt%	11.3	1.05	18.0
PVA / GO 0.5 wt%	14.0	0.99	10.8

Figure 9. Stress-strain curves of neat PVA and PVA/GO composite fibers with different GO loading at 0.1, 0.3 and 0.5 wt%.

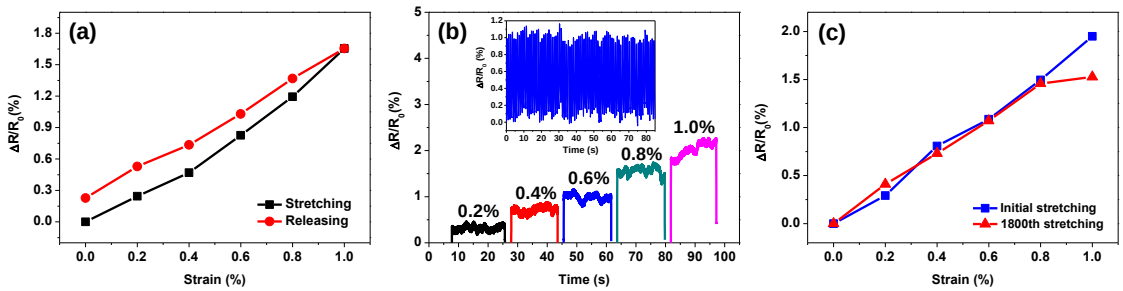

Figure 10. Electrical resistance changes of the rGO-coated PVA/dGO fiber during various imposed conditions; (a) Resistance changes during stretching and releasing within 1% strain. (b) Resistance changes under each step strain from 0.2 % to 1 %. The inset shows the consecutive response signal as function of time with 1 Hz, 1 % strain. (c) Resistance changes of initial and 1,,800th stretching.

Table 3. Comparison of mechanical properties of PVA composite fibers in other reports

Sample type	Sample name	Tensile strength (GPa)	Young's modulus (GPa)	Strain (%)	Ref.
Single fiber	Neat PVA fiber	0.94	13.8	12.1	Our work
	PVA/GO fiber	1.46 (55.3% ↑)	22.4 (62.3% ↑)	17.9 (47.9% ↑)	
	PVA/dGO fiber	1.58 (68.1% ↑)	27.2 (97.1% ↑)	12.3 (1.65% ↑)	
	rGO-coated PVA/dGO fiber	1.86 (97.9% ↑)	27.3 (97.8% ↑)	21.9 (81.0% ↑)	
Single fiber	Neat PVA fiber	0.3	5.6	12	28
	PVA/rGO fiber	0.9 (300% ↑)	15.9 (284.9% ↑)	6 (50% ↓)	
Single fiber	Neat PVA fiber	1.82	30.2	6.5	29
	PVA/rGO fiber	2.2 (20.9% ↑)	36.5 (20.9% ↑)	5.7 (14.0% ↓)	
Single fiber	Neat PVA fiber	1.7	28	11	3
	PVA/SWNT fiber	1.9 (11.8% ↑)	33 (17.9% ↑)	10 (9.1% ↓)	
Single fiber	Neat PVA fiber	0.33	14	14	4
	PVA/MWNT fiber	0.64 (93.9% ↑)	18 (28.6% ↑)	7.5 (46.4% ↓)	

5. References

1. Sreekumar, T. V.; Liu, T.; Min, B. G.; Guo, H.; Kumar, S.; Hauge, R. H.; Smalley, R. E., Polyacrylonitrile single-walled carbon nanotube composite fibers. *Advanced Materials* **2004,** *16* (1), 58-61.
2. Ruan, S.; Gao, P.; Yu, T., Ultra-strong gel-spun UHMWPE fibers reinforced using multiwalled carbon nanotubes. *Polymer* **2006,** *47* (5), 1604-1611.
3. Xu, X.; Uddin, A. J.; Aoki, K.; Gotoh, Y.; Saito, T.; Yumura, M., Fabrication of high strength PVA/SWCNT composite fibers by gel spinning. *Carbon* **2010,** *48* (7), 1977-1984.
4. Zhang, P.; Qiu, D.; Chen, H.; Sun, J.; Wang, J.; Qin, C.; Dai, L., Preparation of MWCNT grafted with polyvinyl alcohol through Friedel–Crafts alkylation and their composite fibers with enhanced mechanical properties. *Journal of Materials Chemistry A* **2015,** *3* (4), 1442-1449.
5. Song, Q.; Li, K.-z.; Li, H.-l.; Li, H.-j.; Ren, C., Grafting straight carbon nanotubes radially onto carbon fibers and their effect on the mechanical properties of carbon/carbon composites. *Carbon* **2012,** *50* (10), 3949-3952.
6. Liu, F.; Ming, P.; Li, J., Ab initio calculation of ideal strength and phonon instability of graphene under tension. *Physical Review B* **2007,** *76* (6), 064120.
7. Lee, C.; Wei, X.; Kysar, J. W.; Hone, J., Measurement of the elastic properties and intrinsic strength of monolayer graphene. *Science* **2008,** *321* (5887), 385-388.
8. Stankovich, S.; Dikin, D. A.; Dommett, G. H.; Kohlhaas, K. M.; Zimney, E. J.; Stach, E. A.; Piner, R. D.; Nguyen, S. T.; Ruoff, R. S., Graphene-based composite materials. *Nature* **2006,** *442* (7100), 282-286.
9. Dikin, D. A.; Stankovich, S.; Zimney, E. J.; Piner, R. D.; Dommett, G. H.; Evmenenko, G.; Nguyen, S. T.; Ruoff, R. S., Preparation and characterization of graphene oxide paper. *Nature* **2007,** *448* (7152), 457-460.
10. Liang, J.; Huang, Y.; Zhang, L.; Wang, Y.; Ma, Y.; Guo, T.; Chen, Y., Molecular-level dispersion of graphene into poly (vinyl alcohol) and effective reinforcement of their nanocomposites. *Advanced Functional Materials* **2009,** *19* (14), 2297-2302.
11. Choi, E.-K.; Jeon, I.-Y.; Bae, S.-Y.; Lee, H.-J.; Shin, H. S.; Dai, L.; Baek, J.-B., High-yield exfoliation of three-dimensional graphite into two-dimensional graphene-like sheets. *Chemical Communications* **2010,** *46* (34), 6320-6322.
12. Jeon, I.-Y.; Shin, Y.-R.; Sohn, G.-J.; Choi, H.-J.; Bae, S.-Y.; Mahmood, J.; Jung, S.-M.; Seo, J.-M.; Kim, M.-J.; Chang, D. W., Edge-carboxylated graphene nanosheets via ball milling. *Proceedings of the National Academy of Sciences* **2012,** *109* (15), 5588-5593.
13. Xu, Y.; Bai, H.; Lu, G.; Li, C.; Shi, G., Flexible graphene films via the filtration of water-soluble noncovalent functionalized graphene sheets. *Journal of the American Chemical Society* **2008,**

130 (18), 5856-5857.

14. Stankovich, S.; Dikin, D. A.; Piner, R. D.; Kohlhaas, K. A.; Kleinhammes, A.; Jia, Y.; Wu, Y.; Nguyen, S. T.; Ruoff, R. S., Synthesis of graphene-based nanosheets via chemical reduction of exfoliated graphite oxide. *Carbon* **2007,** *45* (7), 1558-1565.
15. Li, D.; Mueller, M. B.; Gilje, S.; Kaner, R. B.; Wallace, G. G., Processable aqueous dispersions of graphene nanosheets. *Nature Nanotechnology* **2008,** *3* (2), 101-105.
16. Niyogi, S.; Bekyarova, E.; Itkis, M. E.; McWilliams, J. L.; Hamon, M. A.; Haddon, R. C., Solution properties of graphite and graphene. *Journal of the American Chemical Society* **2006,** *128* (24), 7720-7721.
17. Si, Y.; Samulski, E. T., Synthesis of water soluble graphene. *Nano Letters* **2008,** *8* (6), 1679-1682.
18. Zhang, W. D.; Shen, L.; Phang, I. Y.; Liu, T., Carbon nanotubes reinforced nylon-6 composite prepared by simple melt-compounding. *Macromolecules* **2004,** *37* (2), 256-259.
19. Liu, L.; Barber, A. H.; Nuriel, S.; Wagner, H. D., Mechanical Properties of Functionalized Single-Walled Carbon-Nanotube/Poly (vinyl alcohol) Nanocomposites. *Advanced Functional Materials* **2005,** *15* (6), 975-980.
20. Coleman, J. N.; Cadek, M.; Blake, R.; Nicolosi, V.; Ryan, K. P.; Belton, C.; Fonseca, A.; Nagy, J. B.; Gun'ko, Y. K.; Blau, W. J., High performance nanotube-reinforced plastics: Understanding the mechanism of strength increase. *Advanced Functional Materials* **2004,** *14* (8), 791-798.
21. Ramanathan, T.; Abdala, A.; Stankovich, S.; Dikin, D.; Herrera-Alonso, M.; Piner, R.; Adamson, D.; Schniepp, H.; Chen, X.; Ruoff, R., Functionalized graphene sheets for polymer nanocomposites. *Nature Nanotechnology* **2008,** *3* (6), 327-331.
22. Huang, H.-D.; Ren, P.-G.; Chen, J.; Zhang, W.-Q.; Ji, X.; Li, Z.-M., High barrier graphene oxide nanosheet/poly (vinyl alcohol) nanocomposite films. *Journal of Membrane Science* **2012,** *409*, 156-163.
23. Kim, H. M.; Lee, J. K.; Lee, H. S., Transparent and high gas barrier films based on poly (vinyl alcohol)/graphene oxide composites. *Thin Solid Films* **2011,** *519* (22), 7766-7771.
24. Li, V. C.; Wang, S.; Wu, C., Tensile strain-hardening behavior of polyvinyl alcohol engineered cementitious composite (PVA-ECC). *ACI Materials Journal* **2001,** *98* (6), 483-492.
25. Hou, T.-C.; Lynch, J. P. In *Monitoring strain in engineered cementitious composites using wireless sensors*, Prc. Int. Conf. Fract., 2005.
26. Satcurada, I.; Ito, T.; Nakamae, K., Elastic moduli of the crystal lattices of polymers. *Journal of Polymer Science Part C: Polymer Symposia* **1967,** *15* (1), 75-91.
27. Wang, C.; Li, Y.; Ding, G.; Xie, X.; Jiang, M., Preparation and characterization of graphene oxide/poly (vinyl alcohol) composite nanofibers via electrospinning. *Journal of Applied Polymer Science* **2013,** *127* (4), 3026-3032.
28. Li, Y.; Sun, J.; Wang, J.; Qin, C.; Dai, L., Preparation of well-dispersed reduced graphene oxide

and its mechanical reinforcement in polyvinyl alcohol fibre. *Polymer International* **2016,** *65*, 1054-1062.

29. Li, J.; Shao, L.; Zhou, X.; Wang, Y., Fabrication of high strength PVA/rGO composite fibers by gel spinning. *RSC Advances* **2014,** *4* (82), 43612-43618.
30. Tan, Y.; Song, Y.; Zheng, Q., Hydrogen bonding-driven rheological modulation of chemically reduced graphene oxide/poly (vinyl alcohol) suspensions and its application in electrospinning. *Nanoscale* **2012,** *4* (22), 6997-7005.
31. Lee, H.; Dellatore, S. M.; Miller, W. M.; Messersmith, P. B., Mussel-inspired surface chemistry for multifunctional coatings. *Science* **2007,** *318* (5849), 426-430.
32. Lee, H.; Scherer, N. F.; Messersmith, P. B., Single-molecule mechanics of mussel adhesion. *Proceedings of the National Academy of Sciences* **2006,** *103* (35), 12999-13003.
33. Kang, S. M.; Park, S.; Kim, D.; Park, S. Y.; Ruoff, R. S.; Lee, H., Simultaneous Reduction and Surface Functionalization of Graphene Oxide by Mussel-Inspired Chemistry. *Advanced Functional Materials* **2011,** *21* (1), 108-112.
34. Lee, W.; Lee, J. U.; Jung, B. M.; Byun, J.-H.; Yi, J.-W.; Lee, S.-B.; Kim, B.-S., Simultaneous enhancement of mechanical, electrical and thermal properties of graphene oxide paper by embedding dopamine. *Carbon* **2013,** *65*, 296-304.
35. Hummers, W. S.; Offeman, R. E., Preparation of graphitic oxide. *Journal of the American Chemical Society* **1958,** *80* (6), 1339-1339.
36. Hwang, S.-H.; Kang, D.; Ruoff, R. S.; Shin, H. S.; Park, Y.-B., Poly (vinyl alcohol) reinforced and toughened with poly (dopamine)-treated graphene oxide, and its use for humidity sensing. *ACS Nano* **2014,** *8* (7), 6739-6747.
37. d'Ischia, M.; Napolitano, A.; Pezzella, A.; Meredith, P.; Sarna, T., Chemical and Structural Diversity in Eumelanins: Unexplored Bio-Optoelectronic Materials. *Angewandte Chemie International Edition* **2009,** *48* (22), 3914-3921.
38. Dreyer, D. R.; Miller, D. J.; Freeman, B. D.; Paul, D. R.; Bielawski, C. W., Elucidating the structure of poly (dopamine). *Langmuir* **2012,** *28* (15), 6428-6435.
39. Cha, W. I.; Hyon, S. H.; Ikada, Y., Gel spinning of poly (vinyl alcohol) from dimethyl sulfoxide/water mixture. *Journal of Polymer Science Part B: Polymer Physics* **1994,** *32* (2), 297-304.
40. Ma, X.; Zachariah, M. R.; Zangmeister, C. D., Crumpled nanopaper from graphene oxide. *Nano Letters* **2011,** *12* (1), 486-489.
41. Kudin, K. N.; Ozbas, B.; Schniepp, H. C.; Prud'Homme, R. K.; Aksay, I. A.; Car, R., Raman spectra of graphite oxide and functionalized graphene sheets. *Nano Letters* **2008,** *8* (1), 36-41.
42. Xu, Y.; Hong, W.; Bai, H.; Li, C.; Shi, G., Strong and ductile poly (vinyl alcohol)/graphene oxide composite films with a layered structure. *Carbon* **2009,** *47* (15), 3538-3543.

43. Cadek, M.; Coleman, J.; Barron, V.; Hedicke, K.; Blau, W., Morphological and mechanical properties of carbon-nanotube-reinforced semicrystalline and amorphous polymer composites. *Applied Physics Letters* **2002,** *81* (27), 5123-5125.
44. Zhang, L.; Pu, J.; Wang, L.; Xue, Q., Synergistic Effect of Hybrid Carbon Nanotube–Graphene Oxide as Nanoadditive Enhancing the Frictional Properties of Ionic Liquids in High Vacuum. *ACS Applied Materials & Interfaces* **2015,** *7* (16), 8592-8600.
45. Pukanszky, B.; VÖRÖS, G., Mechanism of interfacial interactions in particulate filled composites. *Composite Interfaces* **1993,** *1* (5), 411-427.
46. Nakamura, Y.; Yamaguchi, M.; Okubo, M.; Matsumoto, T., Effects of particle size on mechanical and impact properties of epoxy resin filled with spherical silica. *Journal of Applied Polymer Science* **1992,** *45* (7), 1281-1289.
47. Reynaud, E.; Jouen, T.; Gauthier, C.; Vigier, G.; Varlet, J., Nanofillers in polymeric matrix: a study on silica reinforced PA6. *Polymer* **2001,** *42* (21), 8759-8768.
48. Zhang, Q.; Tian, M.; Wu, Y.; Lin, G.; Zhang, L., Effect of particle size on the properties of Mg (OH) 2-filled rubber composites. *Journal of Applied Polymer Science* **2004,** *94* (6), 2341-2346.
49. Fu, S.-Y.; Feng, X.-Q.; Lauke, B.; Mai, Y.-W., Effects of particle size, particle/matrix interface adhesion and particle loading on mechanical properties of particulate–polymer composites. *Composites Part B: Engineering* **2008,** *39* (6), 933-961.
50. Young, K.; Blighe, F. M.; Vilatela, J. J.; Windle, A. H.; Kinloch, I. A.; Deng, L.; Young, R. J.; Coleman, J. N., Strong dependence of mechanical properties on fiber diameter for polymer−nanotube composite fibers: differentiating defect from orientation effects. *ACS Nano* **2010,** *4* (11), 6989-6997.
51. Daly, M.; Cao, C.; Sun, H.; Sun, Y.; Filleter, T.; Singh, C. V., Interfacial Shear Strength of Multilayer Graphene Oxide Films. *ACS Nano* **2016,** *10* (2), 1939-1947.
52. Wang, L.-F.; Ma, T.-B.; Hu, Y.-Z.; Wang, H., Atomic-scale friction in graphene oxide: an interfacial interaction perspective from first-principles calculations. *Physical Review B* **2012,** *86* (12), 125436.
53. Dobie, W.; Isaac, P. C., ELECTRIC RESISTANCE STRAIN GAUGES. **1948**.
54. Yamada, T.; Hayamizu, Y.; Yamamoto, Y.; Yomogida, Y.; Izadi-Najafabadi, A.; Futaba, D. N.; Hata, K., A stretchable carbon nanotube strain sensor for human-motion detection. *Nature Nanotechnology* **2011,** *6* (5), 296-301.

Chapter 4: Fabrication of three-dimensional and porous reduced graphene oxide/carbon nanotube spheres for supercapacitor electrode

1. Introduction

Two-dimensional (2D) graphene oxide (GO) nanosheets are attracting tremendous interest due to their exceptional properties emanating from their unique morphology.[1-3] Theoretically, graphene nanosheets have a high specific surface area of over 2,500 m^2/g,[4] making them highly desirable for use as a 2D support for many applications. These nanosheets display high flexibility, enabling the possibility of encapsulation for drug delivery, photocatalysis, solar cells, and electrical energy storage systems.[4-7] One issue is the tendency to aggregate and restack due to strong intersheet interaction (Van der Waals attraction).[8] Restacking of these nanosheets reduces their accessible surface area and hence the negatively affects to the properties and subsequent applications. One possible solution is to turn the two-dimensional (2D) sheets into three-dimensional (3D) structure like crumpled balls and hollow spheres. Unlike flat sheets, the 3D structure of GO have high free volume and excellent compressive properties, and can tightly pack without significantly reducing the accessible surface area.[9] At a crumpled equilibrium, approximately 58.6% of the accessible surface area, *i.e.*, over 1,500 m^2/g is maintained,[10] which is still much larger than those of conventional laminar or porous materials. Crumpled sheet materials represent a new class of structures attracting a great interest because of their unique mechanical and physical properties. Such materials seem to be very promising for applications in the fields where extremely large specific surface area is required,[11] which is in its turn governed by the morphology of crumpled configuration.[12] These applications are ranged from virus capsids and polymerized membranes to folded engineering materials and geological formations.[13]

Adsorption occurring at the surface of solids is a fundamental phenomenon that is essential to a wide range of applications, such as electrochemical energy storage, gas capture, molecular separation, and environmental remediation.[14-16] For both electrochemical and chemical systems, the specific adsorption capacity is the most critical parameter for evaluation of adsorbent performance. Except in some cases, the capacity is proportional to the accessible surface area, and thus, can be improved by increasing the surface area, accomplished either by creating microporosity or by reducing the particle size.[17-18] Physical and chemical activation is a conventional technology to achieve microporosity in porous carbons by enlarging the surface area.[19] Such existing techniques have been revisited in the nanotechnology and graphene literature since dramatic capacitance enhancements in KOH-activated graphenes were demonstrated, due to increased available surface area.[20-21] Nevertheless, microporous graphene neither exhibit fast mass and ion transport kinetics nor provide easy access to adsorption sites. Given that three-dimensional interconnected macroporosity is needed to resolve these issues,[22-24] hierarchical porosity is hypothesized to be an ideal texture for high performance capacitive materials.

Moreover, porous materials need to be assembled into a monolithic form on a bulk level for most practical applications.

Here, we introduce such a simple, facile and scalable approach to fabricate three-dimensional rGO and rGO/CNT with crumpled and spherical structure using spray drying followed by microwave treatment. Furthermore, porous surfaces were achieved by CO_2 activation. This porous and three-dimensional rGO-based architecture will provide better ion transport channels. In addition, CNT are used to inhibit the aggregation of rGO sheets, which will significantly raise the electrolyte-accessible surface area, and able to bridge the gap between rGO sheets to form a conductive network, providing pathway for electron conduction in composites. Hence, porous and three-dimensional rGO-based electrode with good electrochemical capacitive performance can be obtained by designing and tailoring CNT.

2. Experimental section

2.1. Materials

Grphaite (SP-1, Baycarbon), H_2SO_4 (98 %, Merck), $KMnO_4$ (99 %, Sigma), and carbon nanotubes (Muli-wall carbon nanotube, Hanwha chemical) were used as received without further purification.

2.2. Preparation of GO

Graphite oxide was prepared from purified natural graphite (SP-1, Bay Carbon) using the modified Hummers method. Graphite powder (2.0 g) was added to concentrated H_2SO_4 (46 mL) and$KMnO_4$ (6.0 g) was added gradually with stirring and cooling, while the temperature of the mixture was maintained below20 ^oC. The mixture was then stirred at 35 ^oC for 2 h, and distilled water (92 mL) was added. After 15 min, the reaction was terminated by the addition of a large amount of distilled water (280 mL) and a 30 % H_2O_2 solution (5.0 mL), after which the color of the mixture changed from black to bright yellow. The mixture was filtered and washed with a 1:10 HCl solution (500 mL) in order to remove metal ions. The graphite oxide product was suspended in distilled water to give a viscous, brown dispersion, which was subjected to dialysis to completely remove metal ions and acids. To obtain the GO dispersion, graphite oxide was exfoliated by treatment with a mechanical homogenizer at 15000 rpm for 15 min, followed by sonication (ultrasonic cleaner, 100 W, Branson) for 15 min and then centrifugation at 4000 rpm for 10 min.

2.3. Preparation of water-dispersible CNT

In order to fabricate three-dimensional rGO/CNT architecture, two types of water dispersible CNT were prepared through oxidation and surfactant. Firstly, oxidized CNT was prepared by refluxing in concentrated H_2SO_4/HNO_3 (3/1 v/v, 96 % and 70 %, respectively) at 70 ^oC for 24 hr. After that,

MWNT were functionalized by carboxylic acid (MWNT-COOH), and then washed with deionized water several times using anodisc membrane filter (0.2 μm).[25]

Surfactant-assisted CNT was prepared by followed: An aqueous solution containing 1% by the weight of sodium dodecyl benzene sulfonate (SDBS) in deionized water was made up. An amount of 250 mg of as-prepared MWNT was added to 50 mL of the SDBS solution. The MWNT/SDBS solution was tip-sonicated for 15 min at 20 % of the power output. Then, this sample was washed with deionized water several times by centrifugation.[26]

2.4. Fabrication of three-dimensional and porous rGO/CNT sphere

GO dispersions were processed in a spray dryer (Buchi B-90 spray dryer) to yield crumpled nanosheets. In this process, micrometer-sized droplets of dispersion were produced by the atomizer (Nozzel with 7.0 μm) of the spray dryer. The droplets were carried away and dried by hot air to produce powder particles. The dry powders were settled by a cyclone separator and the air was discharged from the separator along with small particles. The atomizer pressure was about 30 mbar and the hot air temperature was 120 ^{o}C. Temperature and pressure were changed in various experiments to assess the effect of these parameters on the final morphology of the product. In all experiments, 30-40 % of the spray rate was used for spraying the dispersions.

2.5. Electrochemical test

The cyclic voltammetry and galvanostatic charge–discharge measurements were carried out using a three-electrode configuration. Each sample was used as a working electrode, Ag/AgCl as a reference electrode, and Pt plate as a counter electrode. 1 M of aqueous H_2SO_4 solution was used as an electrolyte. All potentials were referred to the Ag/AgCl reference electrode.

2.6. Characterizations

The morphology of the GO sheets, crumpled rGO and rGO sphere was analyzed using and scanning electron microscope (SEM, FEI VERIOS 460). Raman spectra of rGO/CNT hybrid were measured using an Alpha 300 micro Raman spectrometer (Witec) equipped with 532 nm laser. Atomic resolution microscopy was performed with high-resolution transmission electron microscope (TEM, JEOL JEM-2100F). Chemical structures of the samples were identified by X-ray photoelectron spectroscopy (XPS) using ESCALAB250Xi (Thermo Scientific) equipped with monochromatic Al K-Alpha source. The electrochemical characteristics were evaluated using a ZIVE SP2 Electrochemical Workstation (ZIVE Lab, Korea) at room temperature.

3. Results and discussion

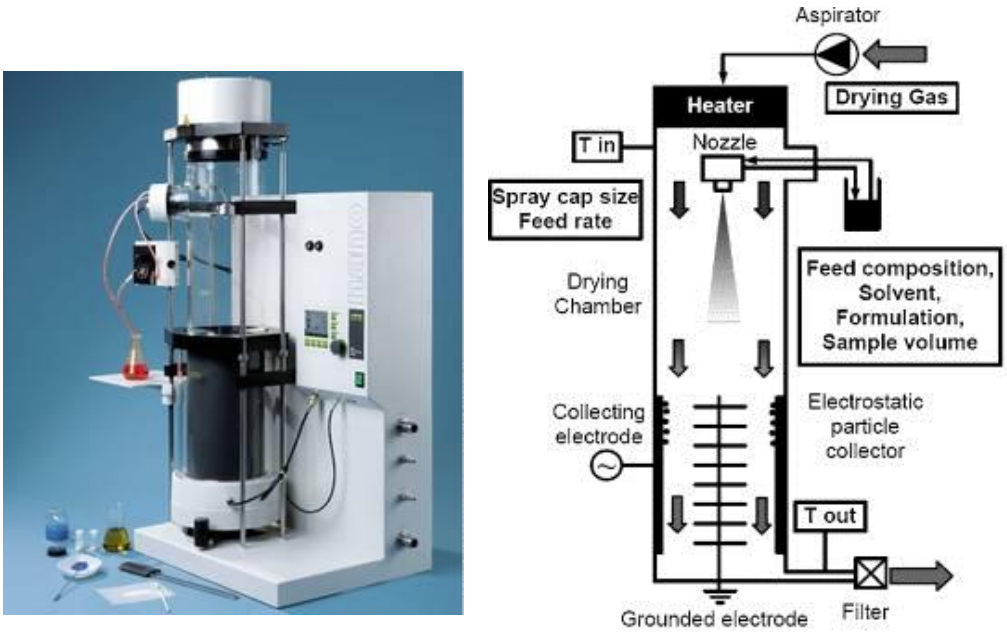

Figure 1. Photograph and schematic description of spray dry system (Buchi B-90)

3.1. Optimizing the fabrication process for crumpled GO and rGO spheres

Three-dimensional crumpled GO were prepared by spray drying processing of graphene oxide (GO), and the photograph of equipment and schematic description of operating systems were displayed in Figure 1. Injected solutions were sprayed by vibrated nozzle that has micron-sized holes (7.0 μm), and subsequently dried by inflow warm air (120 ^{o}C) and collected onto collecting electrode by electrostatic force. Therefore, sprayed materials such as GO should be well dispersed in water and ethanol to avoid unexpected nozzle clogging. Aqueous dispersion of GO was prepared by modified Hummers' methods and used as a starting material for crumpled GO. All GO sheets were dispersed in a single layer with an average lateral size of 2.29 μm as represented in Figure 2(a). In contrast to crumpled GO in Figure 2(b), GO sheets does not show any ripples and wrinkles. It means that GO suspension is a very stable state in water due to inserted functional groups which are mainly the epoxy group on the basal plane and hydroxyl and carboxylic groups on the edge side. The concentration of GO suspension was 0.5 mg/mL and dried at the temperature of 120 ^{o}C with varied nozzle diameter from 4.0 to 7.0 μm. Figure 2(b) shows SEM and photograph (inset) images of crumpled GO powders. The mechanism and force involved in GO crumpling can be understood from microscale systems of noninteracting sheet. On the nanoscale, the confining force applied to the nanosheet is capillary force during the drying process. The confining force applied to GO sheets initially form ridges which can grow until it folds, wrinkles and three-dimensional crumpled conformations. We found that the collection yields of crumpled GO powder and consumed volume of GO solutions were increased with increasing the size of the nozzle. However, even if the size of the nozzle varied, the difference of the surface area and morphologies of crumpled GO powders were negligible after being dried. Figure 3 shows Brunauer–Emmett–Teller (BET) surface area analysis and the statistical size distribution of crumpled GO powder. Crumpled GO powder shows the mesoporous solid structure (type IV) with the surface area and the total pore volume of 109.24 m^2/g and 0.15 cm^3/g, and polydispersed particle size distribution in the range of 1.33 ± 0.625 μm. Particle size polydispersity originated from both the original GO sheet size polydispersity and droplet size variation. In recent years, many studies on the synthesis and applications of crumpled graphene have been conducted, and the results reported that the crumpled structure of graphene can have a much higher surface area than that of the flat structure because crumpled structure may contain a number of pores. In contrast to previous reports, our experimental results showed a relatively low surface area. Generally, although the single layer graphene shows a surface area of higher than 2,500 m^2/g, the surface area of the graphene powder is drastically reduced with an increase in the number of layers. Thus, it is thought that fabricated crumpled GO powders have formed a large number of layers in the current manufacturing conditions (0.5 mg/mL of suspension concentration).

In order to produce a three-dimensional graphene having a high specific surface area, microwave assisted exfoliation method was introduced in our experiments. As a convenient and rapid heating

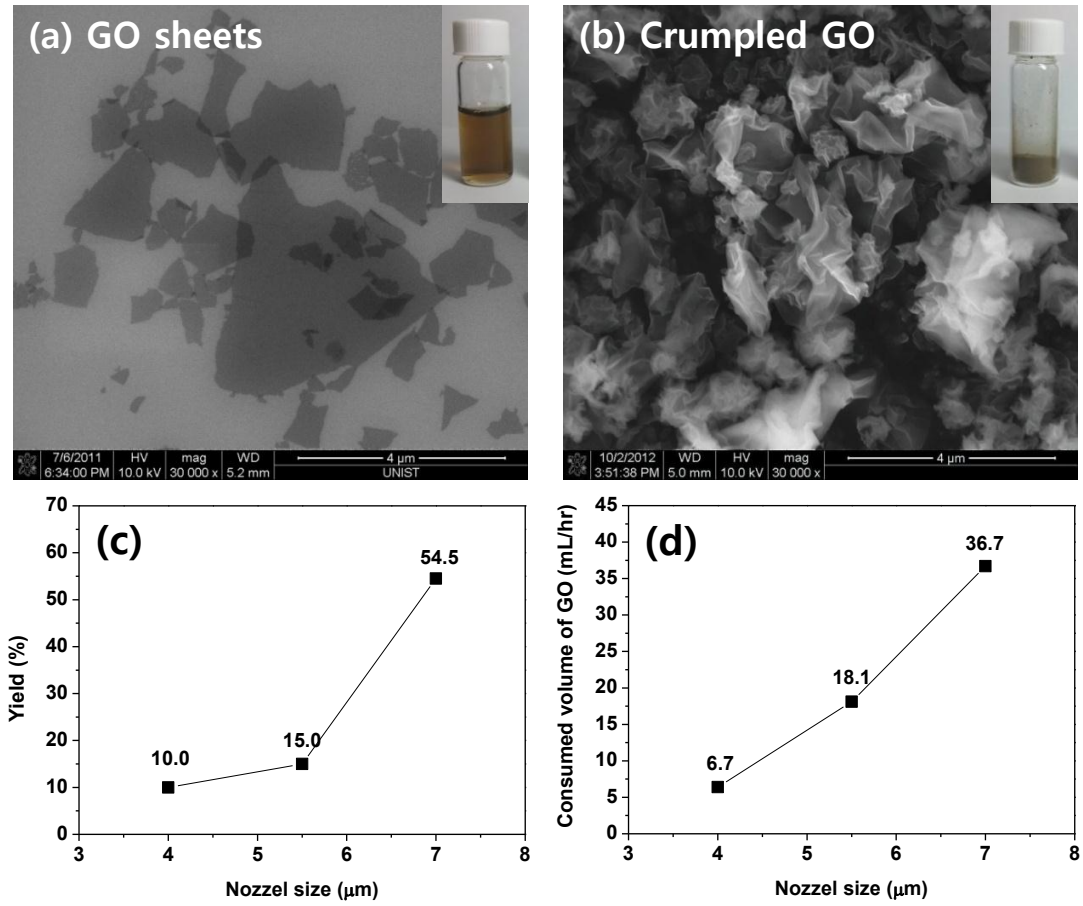

Figure 2. SEM image of (a) GO sheets and (b)crumpled GO. Plots of powder yield (%) and consumed volume of GO solution per hour *vs.* spray nozzle size.

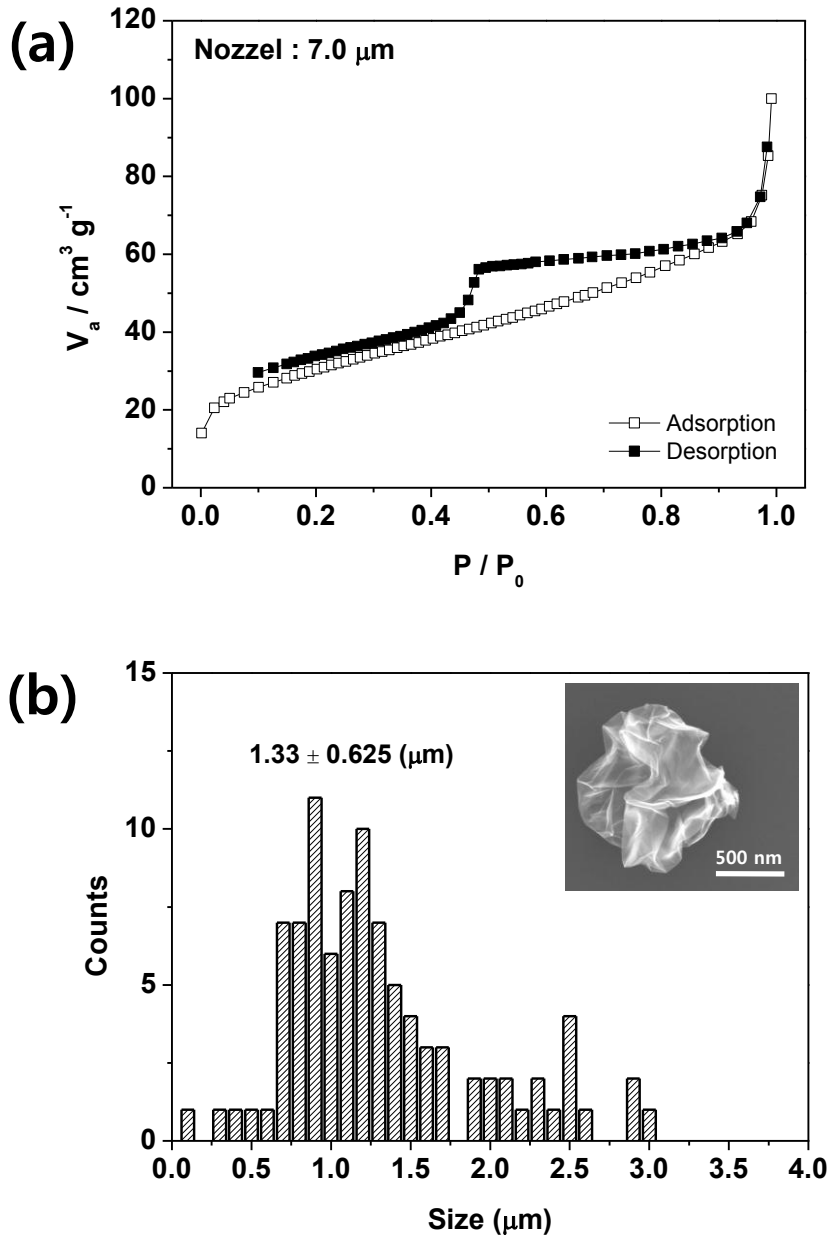

Figure 3. Characterization of crumpled GO. (a) N_2 adsorption and desorption isotherms and (b) histogram of size distribution of crumpled GO.

source, microwave irradiation has been used to prepare exfoliated graphite from a wide range of graphite intercalation compounds. Recently microwave assisted chemical reduction of graphene oxide has been realized by heating its suspensions in aqueous or organic media. From reported results, microwave assisted exfoliated graphene oxide (as known as MEGO) showed a specific surface area of 463 m^2/g, which was 6-9 times higher than the typical values (50-77 m^2/g) obtained from exfoliated graphite prepared by treatment of graphite intercalation compounds with microwave irradiation. Fabricated crumpled GO powders were treated in a microwave oven (LG electronics, model: MW-203LW) in ambient conditions at 700 W for 60 sec. Upon microwave irradiation, a large volume expansion of the crumpled GO powders, accompanied by fuming and spark was observed. Additionally, microwave-treated crumpled GO powder has dramatically expanded yielding a black and fluffy powder, which means that crumpled GO powders were reduced by microwave-induced heat. It should be noticed that a proper amount of crumpled GO powders and an appropriately sized container with ventilation are suggested to minimize the dangers, and carrying out the experiments in a chemical hood is preferred to avoid possible inhalation of graphene powder and released gas. SEM images in Figure 4(a and b) shows that microwave-treated crumpled GO powders turned into a sphere-like morphology (starting at this point, it is now designated as “rGO sphere”), similar to the graphene spheres obtained by coating rGO sheets on PS beads or silica spheres. Transmission electron microscopy (TEM) was used to assess rGO sphere, which was first dispersed in ethanol and then vacuum dried on a TEM grid. A typical TEM images in Figure 4 (c-d) shows that rGO sphere is transparent to the electron beam and a hollow structure with many wrinkled and folded layers. A high-resolution TEM (HR-TEM) image (Figure 4(d)) from the same sample displayed that the edge of rGO sphere contained few irregularly stacked layers with approximately 5 nm of thickness. These were corresponded to 14-15 layers of graphene. A possible mechanism of rGO sphere prepared by microwave treatment is illuminated in Figure 5. The polar oxygen-containing functional groups and intercalated water molecules in crumpled GO can interact with irradiated microwave, and that generates localized heat. This microwave-induced heat may provide sufficient energy to reduce the functional group. The large amount of gases, such as CO and CO_2, instantaneously generated by the reduction is not allowed to pass through the rGO sheets, and it makes a dramatic increase of internal pressure.

X-ray photoelectron spectroscopy (XPS) was performed on the as-prepared crumpled GO and rGO sphere and the C 1s spectra were displayed in Figure 6(a-c), with that of the GO sheets for reference. Typically, the peaks between 294.0 and 295.5 eV were assigned to C-C and C=C bonding. Plus, between 286.0 and 289.0 eV were assigned to oxygen-containing functional groups such as epoxide, hydroxyl and carboxyl groups in GO. For crumpled GO powder, although two characteristic peaks of GO were retained, the peak at 286.68 eV corresponding to the oxygen-containing functional groups was slightly reduced than that of GO sheets. The results suggested that crumpled GO powders were

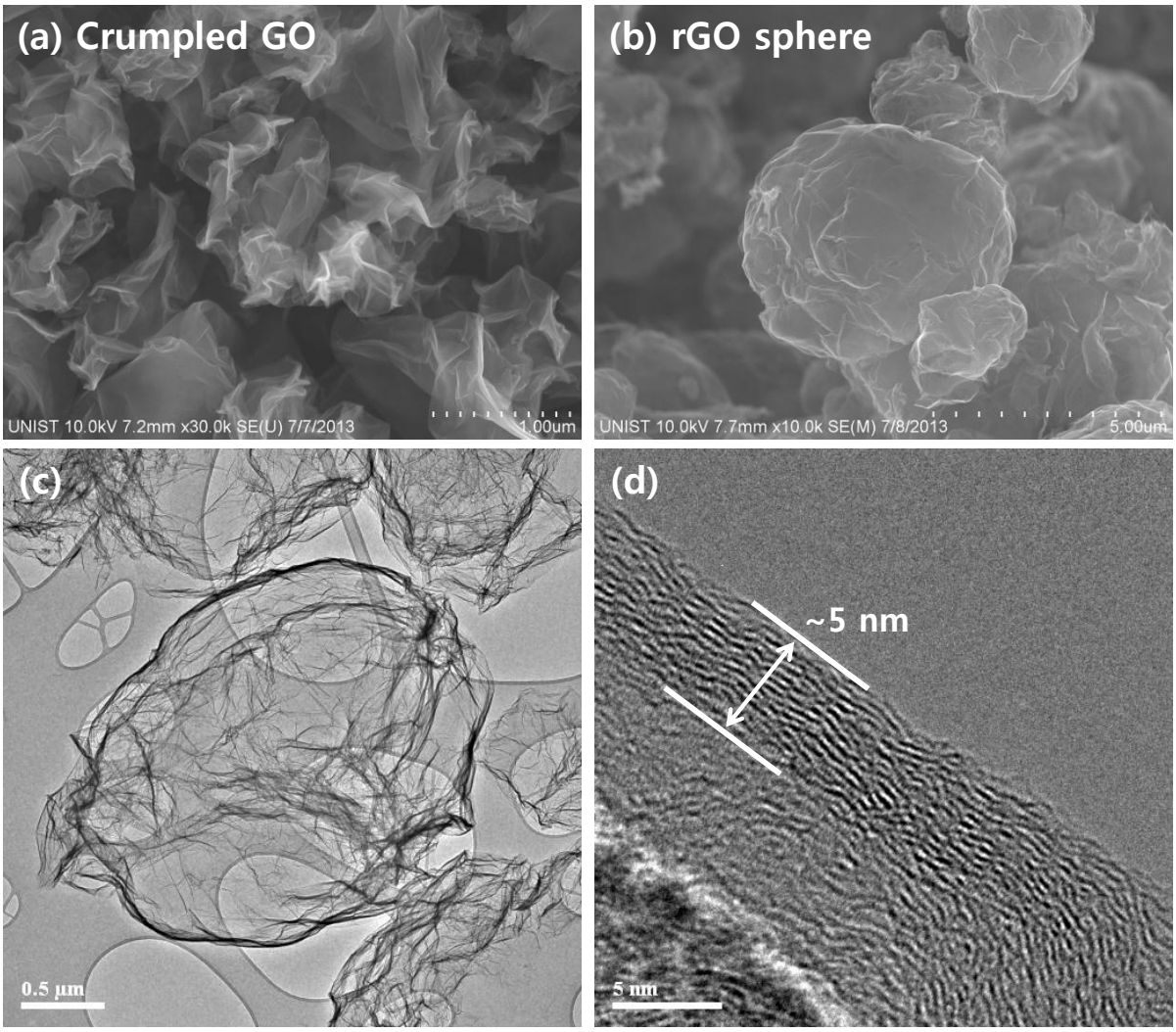

Figure 4. SEM image of crumpled (a) GO and (b) rGO sphere prepared by microwave treatment. (c) Low and (d) High-magnified HR-TEM image of rGO sphere.

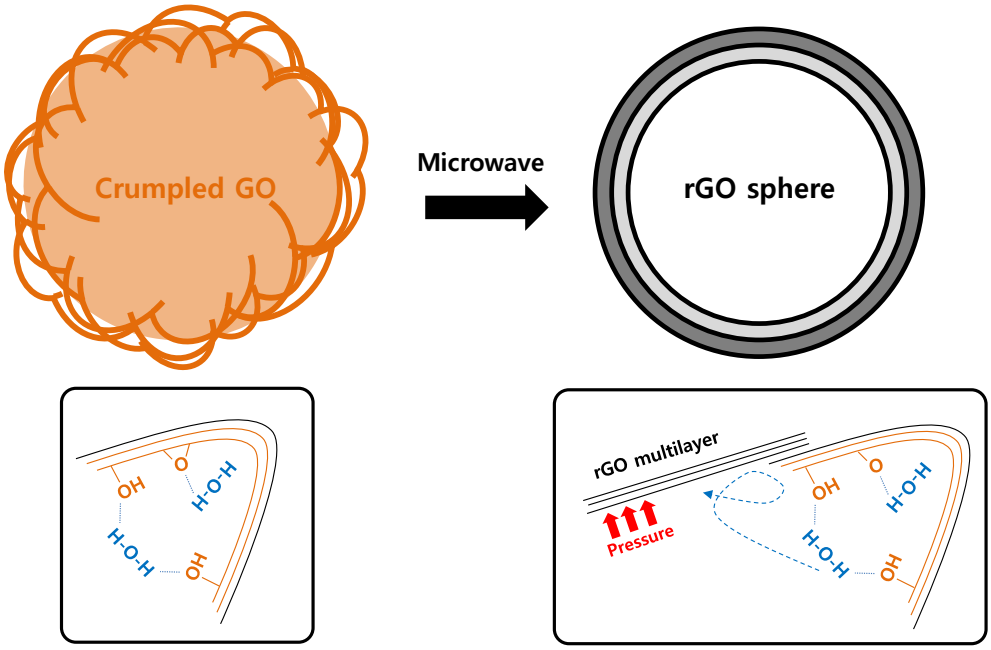

Figure 5. Schematic description of the proposed formation mechanism of rGO sphere.

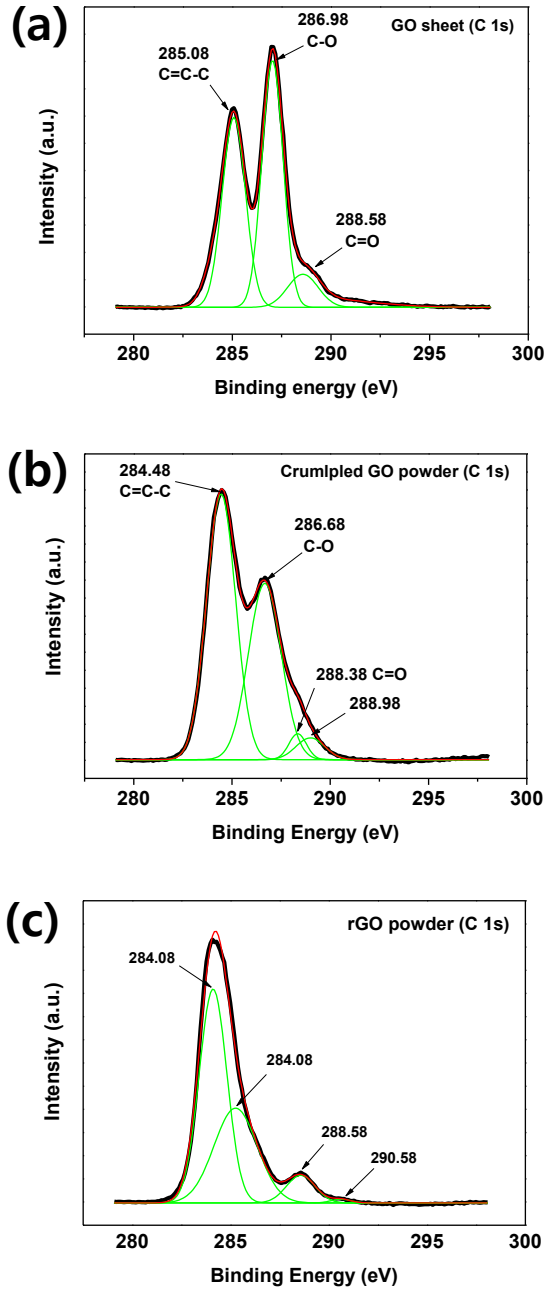

Figure 6. XPS spectrum of (a) GO sheets, (b) crumpled GO and (c) rGO sphere.

partially reduced during the spray process with inflow warm air (120 °C). On the other hand, peaks located between 286.0 and 289.0 eV were almost diminished in rGO sphere powders, which means that rGO sphere powders were sufficiently reduced by microwave treatment.

3.2. Fabrication of porous rGO/CNT sphere

Three-dimensional crumpled GO and rGO sphere structure have been considered as an alternative way for making a high specific surface area carbon material. In addition, the insertion of spacer and a variety of activation methods have been studied in order to produce a carbon material with higher specific surface area.

3.2.1. Effect of CNT as a spacer on surface area of rGO/CNT sphere

The fabrication procedure for the three-dimensional rGO/CNT hybrid is schematically displayed in Figure. 7. Graphene oxide (GO) was synthesized in the same manner as in the previous crumpled GO studies. In parallel, the water-dispersible CNT were initially prepared from the oxidation of MWNT in the presence of strong acids to afford MWNT functionalized with carboxylic acids (See Experimental section 2.3). Prepared GO sheets and CNT were water-dispersible and homogeneously mixed by simple sonication. The surface morphologies of GO/CNT mixture were examined and observed from SEM as shown in Figure 8. The SEM images indicated that the CNT were located between the GO sheets in the hybrid film. The layer stacking of GO sheets, similar to graphite, should show a lower surface area in comparing with its theoretical value. Therefore, CNT existing between GO layers in hybrid film served as a physical spacer that discouraged restacking of GO sheets and created a well-defined porous structure by providing sufficient gaps between the microscopically wrinkled GO sheets.

We systemically evaluated the effect of CNT as a spacer on surface area of a three-dimensional crumpled GO/CNT and rGO/CNT sphere by using BET analysis, and the details of results were summarized in Figure 9. Comparing to crumpled GO, the specific surface area of crumpled GO/CNT were gradually increased with increasing CNT contents, and saturated at about 200 m^2/g. On the other hand, rGO/CNT sphere prepared by microwave irradiation showed an optimal condition in terms of specific surface area. rGO/CNT sphere, which contain 0.05 weight ratio of CNT/GO, showed the highest surface area with 381 m^2/g, and the specific surface area tended to gradually decrease with the increase of CNT content. This result indicates that when the small amount of CNT was inserted between graphene sheets, CNT impede the restacking of graphene sheets and enlarges the space between graphene sheets effectively, leading to a porous architecture. In addition, excess CNT are ineffective nanospacers for inhibiting the restacking of graphene sheets since crumpled GO/CNT maintains their typical crumpled structure after microwave treatment with agglomerates (Figure 10). This phenomenon is attributed to the excess CNT favorable for the formation of CNT bundles by

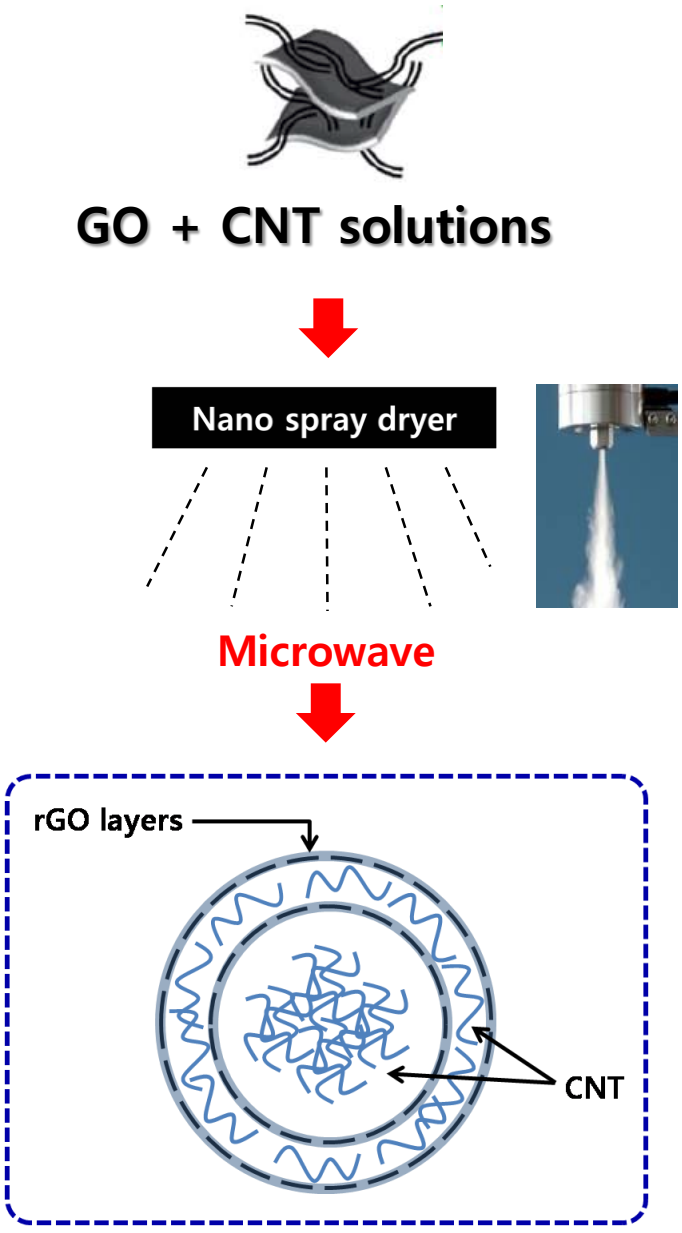

Figure 7. Schematic illustration of preparation of rGO/CNT sphere through spray drying and microwave treatment.

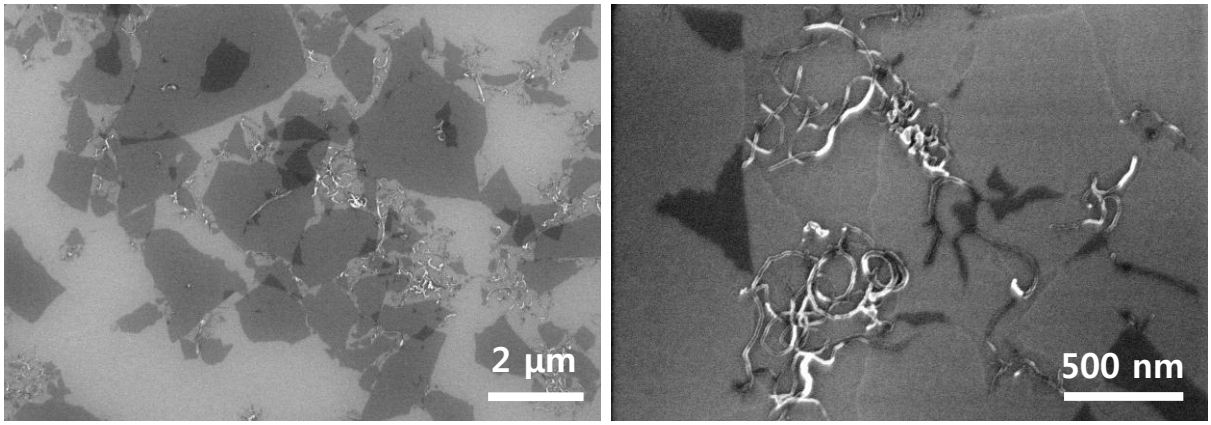

Figure 8. SEM images of GO/CNT. Sample was prepared by spin coating on Si wafer.

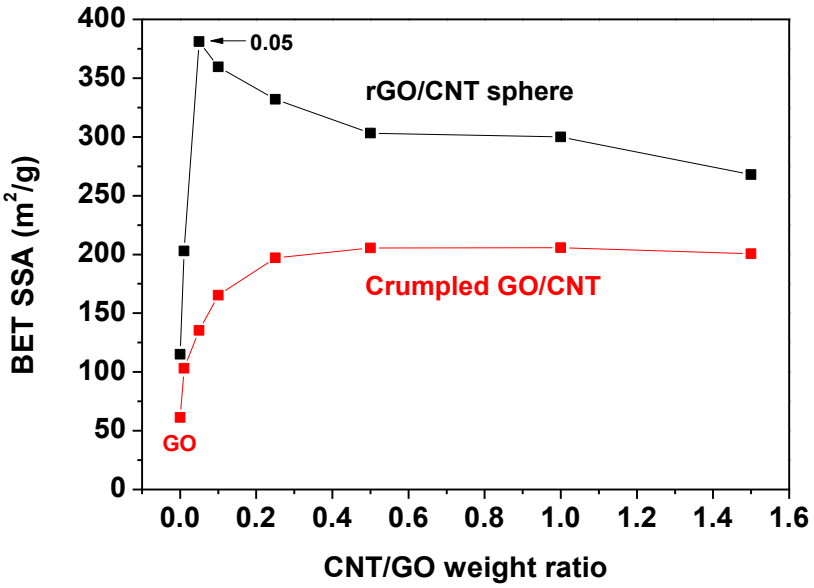

Weight ratio	GO	1	1	1	1	1	1	1
	CNT	0.01	0.05	0.1	0.25	0.5	1.0	1.5
GO/CNT	BET SSA (m^2/g)	103	135.4	165.2	197.1	205.4	205.7	200.6
rGO/CNT sphere	BET SSA (m^2/g)	203	381.0	359.5	332.0	303.2	300.0	267.9

Figure 9. Plot and summarized table of specific surface area of crumpled GO/CNT and rGO/CNT sphere with different CNT/GO ratio from 0.1 to 1.5.

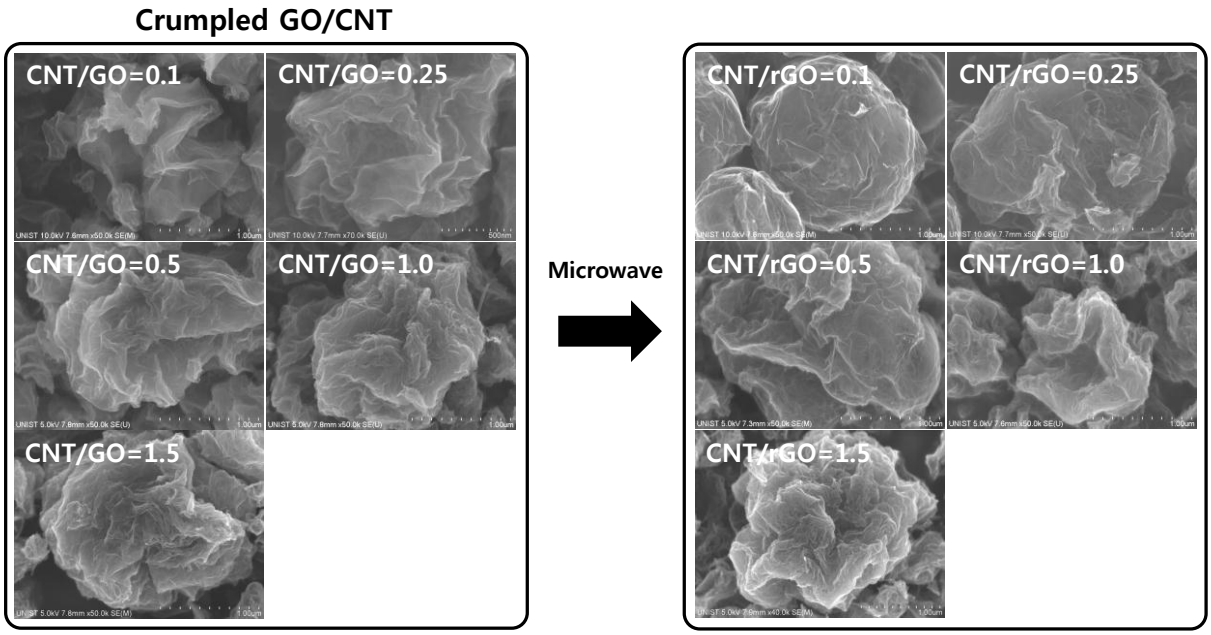

Figure 10. SEM images of crumpled GO/CNT and rGO/CNT sphere with different CNT/GO ratio from 0.1 to 1.5

strong π-π interaction and decreasing the exposure of pores. Therefore, only certain quantity of CNT can be used to form an optimal three-dimensional rGO/CNT sphere structure which exhibits disordered carbon nanotextures with the high surface area.

Figure 11 shows TEM images of the rGO/CNT spheres, and the corresponding HR-TEM images of the edge of rGO/CNT sphere. The HR-TEM images indicated that the rGO/CNT sphere possessed crystalline and graphitic layers with about 4-5 nm in thickness, which was corresponded to 14-15 layers of graphene in a good agreement with our previous studies on rGO sphere. Additionally, Figure 11(c-d) shows TEM images of the CNT-embedded regions where they were located between the graphene sheets.

The chemical structure of the rGO/CNT sphere was analyzed by XPS as shown in Figure 12. The XPS spectra indicate that the carbon backbones, namely sp^2 carbon (C=C) at ~284.4 eV and sp^3 carbon (C-C) at ~285.6 eV, of crumpled GO/CNT powders before microwave treatment were highly functionalized with oxygen-containing groups, such as epoxy, hydroxyl (C–O: ~287.3 eV), carbonyl (C=O: ~288.9 eV) and carboxyl group (O–C=O: 291.2 eV). In contrast, rGO/CNT sphere showed a significantly increased sp^2 carbon (C=C) peak at 284.6, and peaks corresponding to oxygen-containing functional groups were found to mostly disappear. Moreover, the C/O atomic ratio, which was calculated from survey spectrum, was increased from 2.4 to 5.4 after microwave irradiation for 60 min, confirming the reduction of oxygen-containing functional groups (Table in Figure 12).

3.2.2. Effect of CO_2 activation process on surface area of rGO/CNT sphere

Chemical activation is a conventional technology to achieve microporosity in porous carbon-based materials by enlarging the surface area. Such existing techniques have been revisited in the nanotechnology and graphene researches since dramatic capacitance enhancements in KOH-activated graphene were demonstrated, due to increased available surface area. Chemical activation using KOH was attempted first. Although we fabricated a porous rGO/CNT having a high specific surface area up to 1,500 m^2/g, it was found that the three-dimensional sphere structure was destroyed by the harsh chemical reactions (Figure 13). Therefore, we had to find a new activation method for high-surface-area rGO/CNT composite material. Physical activation may be a good alternative.

The porous crumpled rGO/CNT and rGO/CNT sphere could be readily achieved through CO_2 activation. In order to enlarge the surface area and to provide an additional porous structure, we chose to physically activate the three-dimensional rGO/CNT nanostructure with CO_2 at a high temperature (Typically above 800 ^oC). The morphologies of porous crumpled rGO/CNT were examined by electron microscopy. The results revealed the three-dimensional structure of crumpled rGO/CNT, in which the pore walls were composed of CO_2-activated rGO nanosheets, as observed SEM images in Figure 14. The crumpled structure of three-dimensional rGO/CNT remained intact even after CO_2 activation at a high temperature (900 ^oC). The existence of mesopores could be visualized in a high-

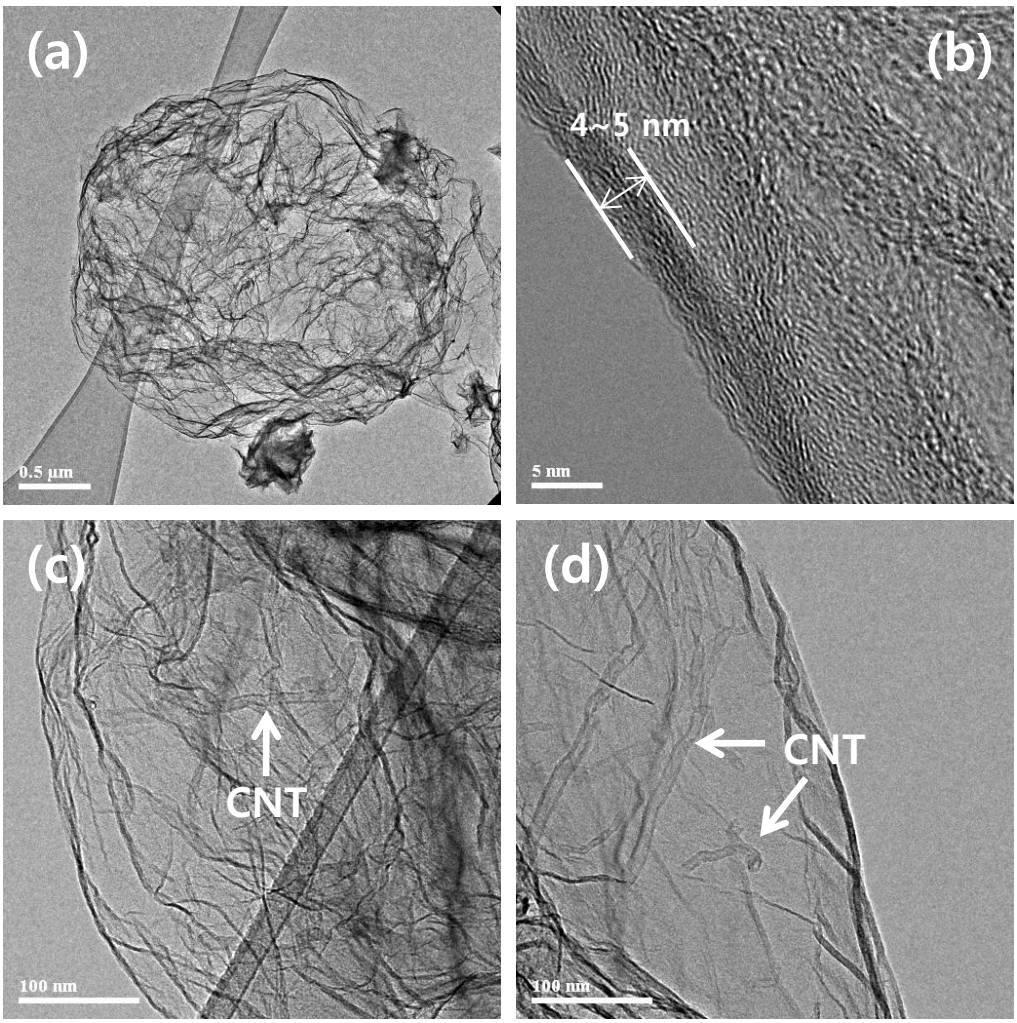

Figure 11. (a) Low and (b-d) high-magnified HR-TEM of rGO/CNT sphere (CNT/GO ratio = 0.05)

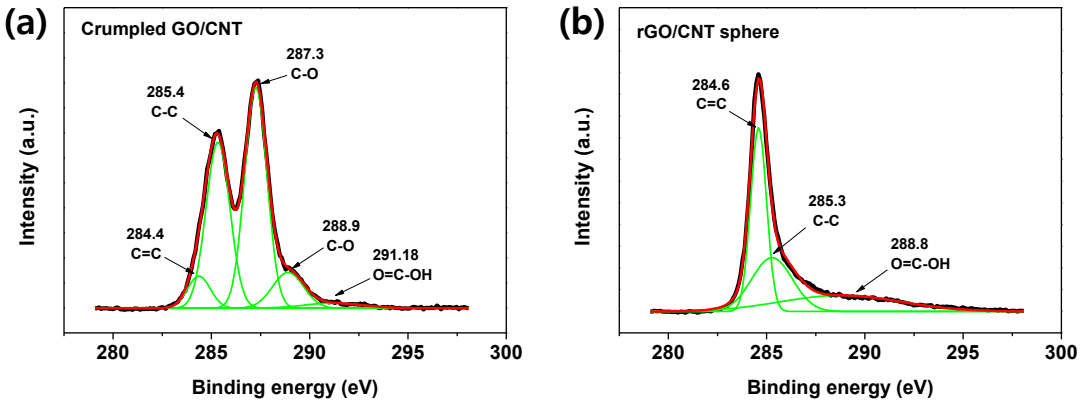

Atomic (%)	Crumpled GO/CNT	rGO/CNT sphere
Carbon	69.5	83.0
Oxygen	28.8	15.3
C/O atomic ratio	2.4	5.4

Figure 12. (a-b) XPS spectrum and atomic contents of crumpled GO/CNT and rGO/CNT sphere

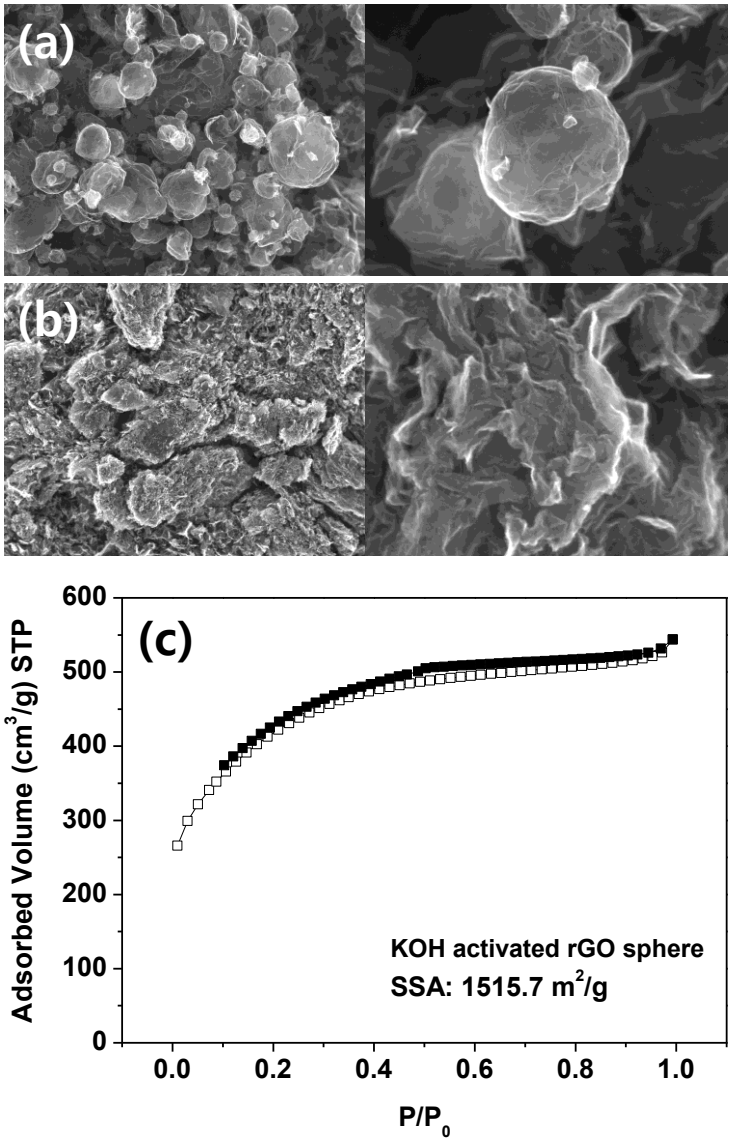

Figure 13. SEM images of rGO/CNT sphere (a) before and (b) after KOH activation, and (c) N_2 adsorption and desorption isotherms of KOH activated rGO/CNT sphere

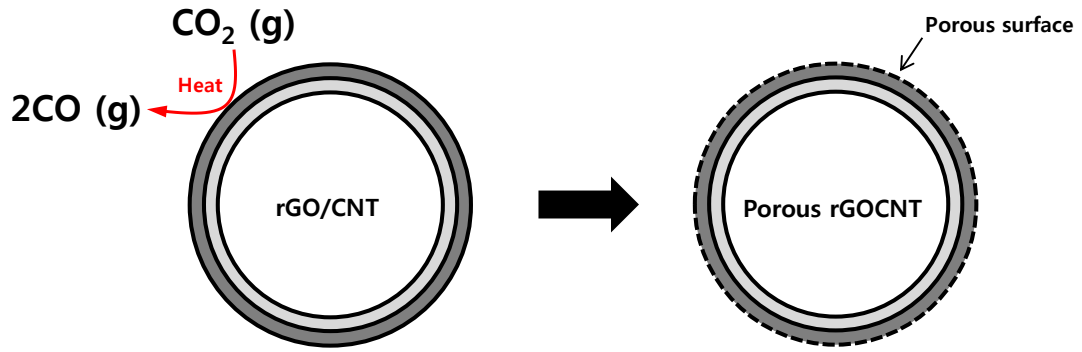

CO_2 + C (g) = 2CO(g), is endothermic (at pressure of 760 mmHg and 749.85 °C, $\triangle H_f$ =169.63 kJ/mol).

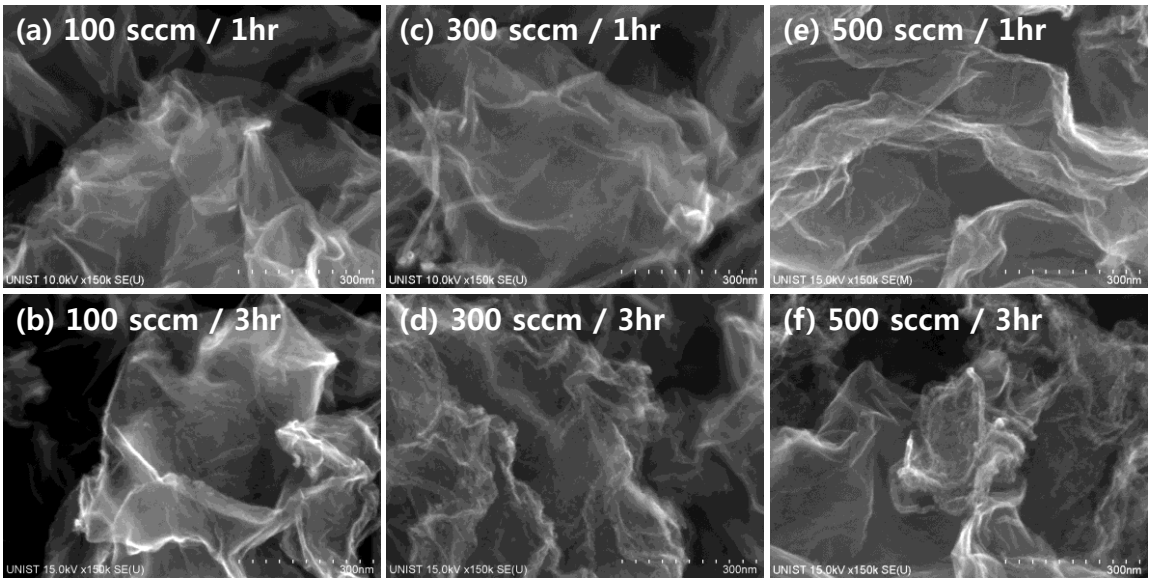

Figure 14. Schematic description of reaction mechanism of CO_2 activation and (a-f) SEM images of CO_2 activated crumpled rGO/CNT with a different reaction condition

magnification of SEM image, whereas very small dark spots might be associated with the existence of micropores. In order to confirm the porous structure of the crumpled rGO/CNT, their textural properties were characterized by N_2 adsorption and desorption isotherms by using BET analysis. A typical type IV isotherm curve of porous crumpled rGO/CNT with hysteresis corresponds to the existence of mesopores. Importantly, the surface area of the porous crumpled rGO/CNT treated with CO_2 300 sccm for 3hr at 900 ^oC dramatically increased to 617.1 m^2/g, ~47.8 times greater than typical values of crumpled rGO/CNT (12.9 m^2/g) (Table in Figure 15). In our system, 3 hours of activation with CO_2 300 sccm was determined to be the optimal condition because the porosity was degraded by CO_2 activation either for longer time or with a higher CO_2 gas flow.

In order to fabricate the high-surface-area and three-dimensional rGO/CNT structure, experimental conditions obtained from CO_2-activated crumpled rGO/CNT were applied to rGO/CNT spheres. In the previous studies, rGO/CNT spheres were found to have higher specific surface area than the crumpled rGO/CNT. Therefore, we expected to achieve a higher specific surface area than the crumpled structure through CO_2 activation. SEM images in Figure 16(a-d) presented as-prepared rGO/CNT sphere and CO_2-activated rGO/CNT sphere at different temperatures between 800 and 900 ^oC with 50 ^oC increments. The microscopic wrinkled structure and corrugated surface were observed in as-prepared rGO/CNT sphere and rGO/CNT spheres were treated at 800 ^oC without pores, whereas rGO/CNT spheres were activated at 850 and 900 ^oC, and showed a porous surface. This indicated that a temperature below 850 ^oC is insufficient to form pores Theoretically, the CO_2 activation can take place at 750 ^oC, but temperature above 850 ^oC is determine to be the optimal condition for porous rGO/CNT sphere. The porosity of rGO/CNT sphere was also confirmed by N_2 adsorption and desorption isotherms by using BET analysis. rGO/CNT spheres exhibited a typical type IV of isotherm curves, which was mesoporous structure with same as the crumpled rGO/CNT samples. The surface area and pore size of as-prepared rGO/CNT sphere was 277.9 m^2/g and 14.69 nm, respectively. There was no significant change in terms of surface area in rGO/CNT sphere activated at 800 ^oC, but a large increase in the surface area was observed in rGO/CNT sphere samples activated at 850 and 900 ^oC. The surface area and pore size were 778.5 m^2/g and 11.85 nm for rGO/CNT sphere activated at 850 ^oC, and 601.1 m^2/g and 14.42 nm for rGO/CNT sphere activated at 900 ^oC (Figure 17). These values are much higher than those of CO_2-activated crumpled rGO/CNT in same condition.

3.3. Electrochemical properties of porous rGO/CNT sphere

The porous and three-dimensional sphere structure enables the rGO/CNT to serve as an excellent electrode for supercapacitors because the porous surface may help to improve the ion kinetics across the rGO sheets. An asymmetric supercapacitor with three-electrode configuration of was assembled using CO_2-activated rGO/CNT sphere samples, and compared its electrochemical capacitance with as-preared rGO/CNT sphere under the identical testing conditions. Figure 18(a) shows the cyclic

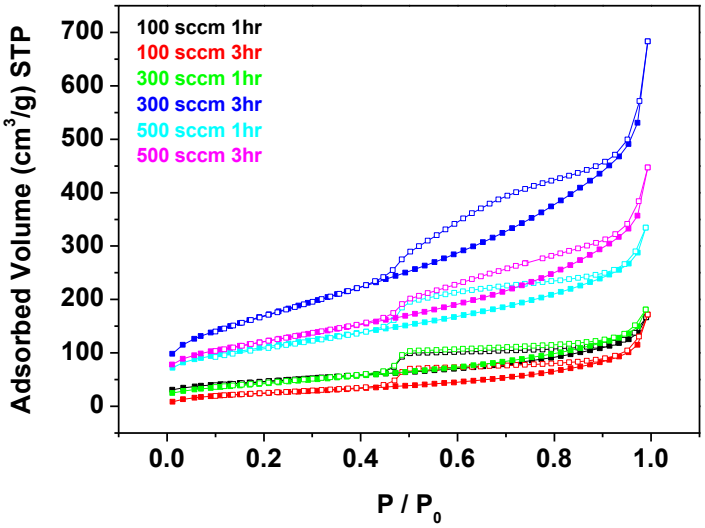

CO_2	Time	SSA (m^2/g)	Pore size (nm)
Crumpled rGO/CNT		12.9	18.87
100 sccm	1hr	162.6	6.34
	3hr	92.6	11.46
300 sccm	1hr	157.1	7.13
	3hr	617.1	6.85
500 sccm	1hr	386.3	5.35
	3hr	425.9	6.49

Figure 15. N_2 adsorption and desorption isotherms and summarized surface area of CO_2 activated crumpled rGO/CNT with different reaction conditions.

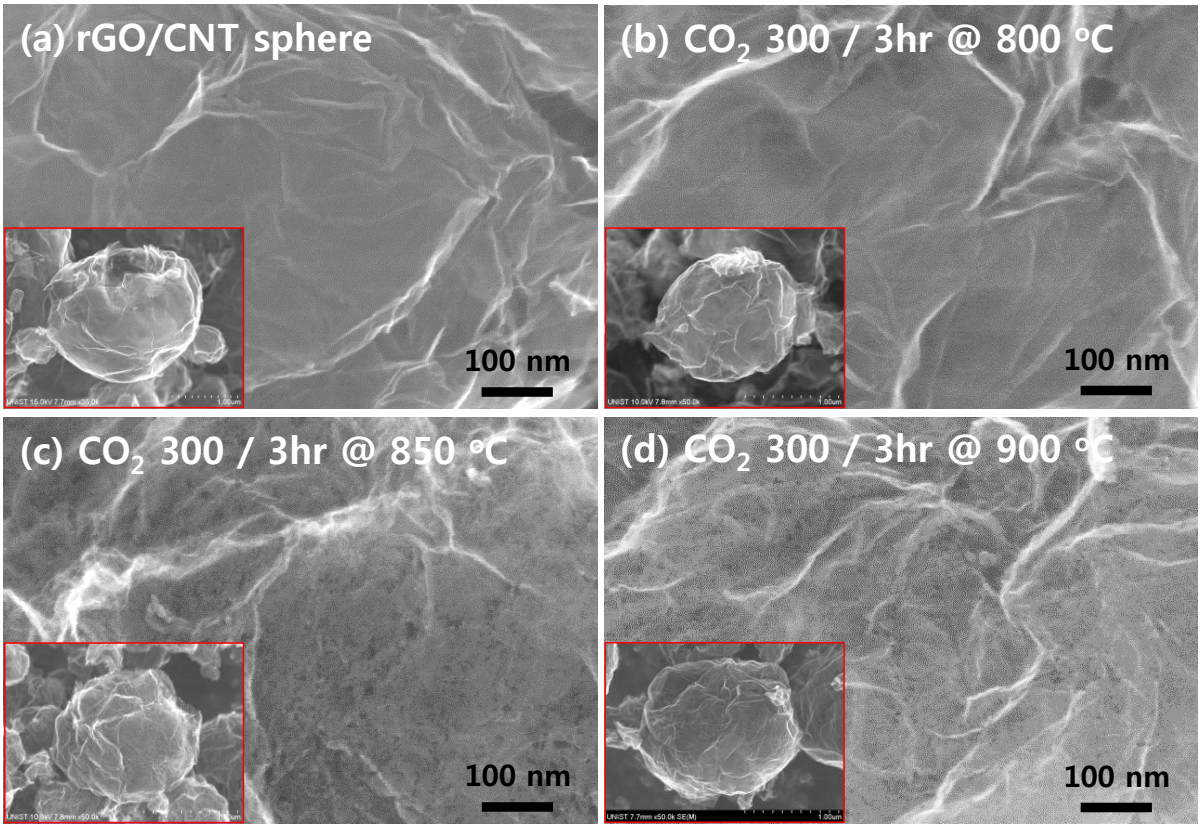

Figure 16. SEM images of CO_2 activated rGO/CNT sphere at different reaction temperature with the flow rate of CO_2 being fixed at 300 sccm.

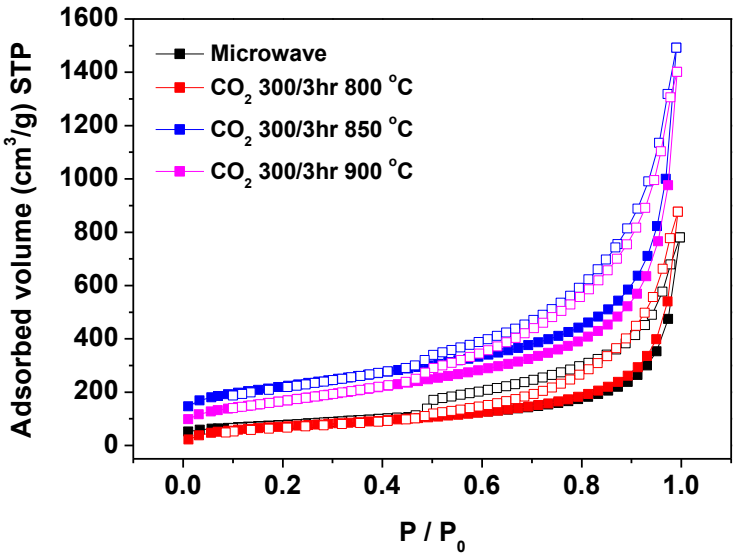

	SSA (m^2/g)	Pore size (nm)
(a) rGO/CNT sphere	277.9	14.69
(b) CO_2 300 / 3hr @ 800 °C	262.7	20.65
(c) CO_2 300 / 3hr @ 850 °C	778.5	11.85
(d) CO_2 300 / 3hr @ 900 °C	601.1	14.42

Figure 17. N_2 adsorption and desorption isotherms and summarized surface area of CO_2 activated rGO/CNT sphere at different reaction temperature with the flow rate of CO_2 being fixed at 300 sccm.

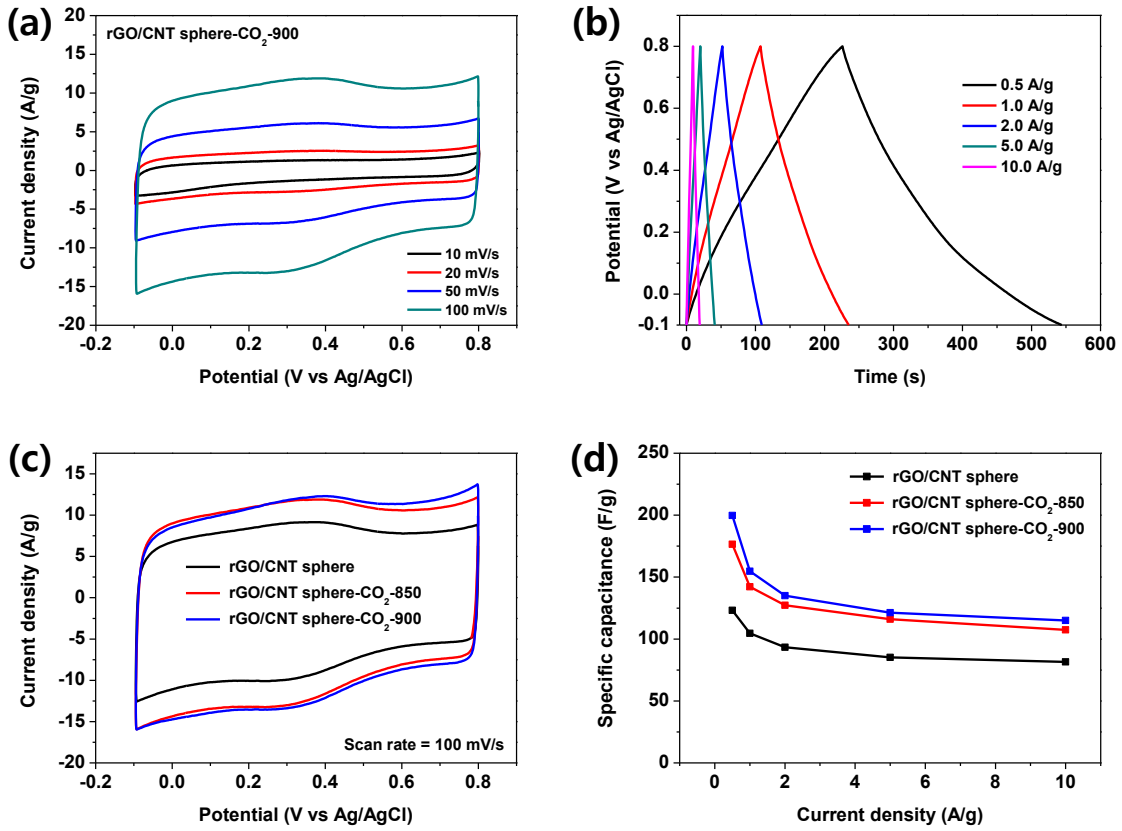

Figure 18. Capacitive performance of rGO/CNT spheres. (a) CV curves at various scan rate and (b) galvanotactic charge-discharge curves of rGO/CNT sphere-CO_2-900. (c) CV curves and (d) specific capacitance retention at different current densities with different samples.

voltammetry (CV) profiles of the rGO/CNT sphere electrode activated at 900 ºC (starting at this point, it is now designated as "rGO/CNT sphere-CO_2-900") over a wide range of scan rates. The rGO/CNT sphere-CO_2-900 displayed a quasi-rentangular CV curve even at high scan rate of 100 mV/s. Figure 18 (b) shows the galvanostatic charge-discharge curves of rGO/CNT sphere-CO_2-900 capacitor at different current densities. The symmetric charge and discharge curves revealed a reversible ion adsorption/desorption at electrode-electrolyte interfaces. The specific capacitance of the rGO/CNT sphere-CO_2-900 at 0.5 A/g was 199.8 F/g and it remained 57 % of its initial capacitance at a current density of 10 A/g (115.1 F/g) (Figure 18(d)). In contrast, although the specific surface area of rGO/CNT sphere-CO_2-850 was higher than rGO/CNT sphere-CO_2-900, they exhibited lower specific capacitance, which might be attributed to the difference in internal electrical resistance.

Electrochemical impedance spectroscopy (EIS) was used to probe the ion transport properties over frequency range from 0.01 Hz to 100 kHz at an open-circuit potential with an AC perturbation of 10 mV and Nyquist plots are shown in Figure 19. Every electrode showed the vertical curves at the low frequency range, which indicated an approximate ideal capacitive behavior with rapid ion diffusion (Figure 19 (a)). At high frequency (close to 100 kHz), the corresponding value of the intercept on a X axis (real axis, *Z'*) represents the intrinsic ohmic resistance or equivalent series resistance (ESR) of the electrode materials and electrolyte. In Figure 19 (b), an expanded view for high frequency range of Nyquist plots were displayed and the results were revealed that rGO/CNT sphere-CO_2-900 showed 2.84 Ω, which was relatively lower than 3.31 and 3.57 Ω for rGO/CNT sphere-CO_2-850 and as-prepared rGO/CNT sphere electrodes, respectively. It is worth nothing that the ESR is related to both electrical resistance of electrode and ion diffusion resistance inside the electrode. Although rGO/CNT sphere-CO_2-850 electrode was supposed to have higher surface area than rGO/CNT sphere-CO_2-900, higher reduction temperature will provide lower electrical resistance, resulting in the lower ESR.

The effect of electrical conductivity on electrochemical performance was examined by unoxidized CNT. The different type of water-dispersible CNT can be prepared by using sodium dodecylbenzene sulfonate (SDBS) as a surfactant without oxidation process. We compared the crystallinity of oxidized CNT and unoxidized CNT using SDBS (starting at this point, it is now designated as "S-CNT") from Raman spectroscopy in Figure 20. Raman spectrum of CNT showed the characteristic features of CNT including the D and G band at 1,340 and 1,573 cm^{-1} with a peak height ratio G/D (I_G/I_D) of 1.10, whereas oxidized CNT showed an increased D band intensity and a broaden G band with decreased I_G/I_D of 0.87 (Figure 20(a)). Moreover, intensity of 2D band at 2,680 also was significantly declined, which means that oxidative reflux introduced functional groups on the tube side walls, resulting in the damaged or destroyed structure of six-membered carbon. In contrast, unoxidized S-CNT obtained from SDBS treatment did not show any noticeable changes in terms of height increase of D band, broadening of G band and decrease of 2D band as shown in Figure 20(b). It means that SDBS used as surfactant can provide water dispersivity by forming the hydrophilic micelle on CNT surfaces without

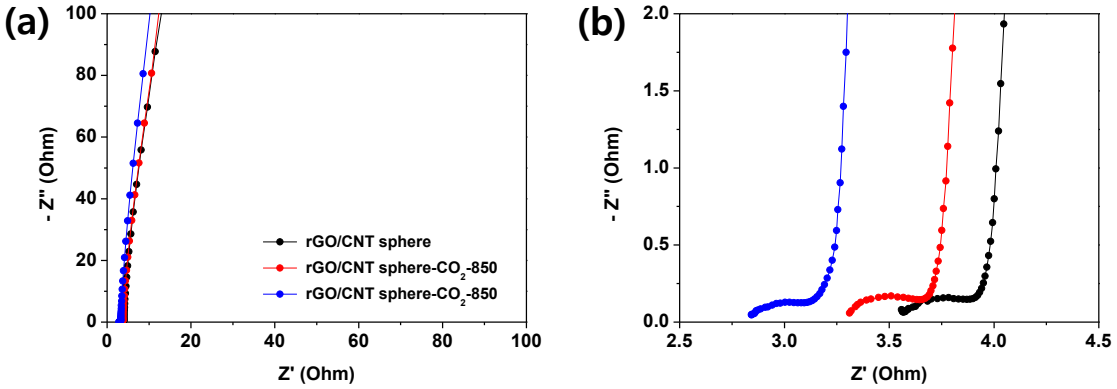

(c)

	SSA (m^2/g)	Pore size (nm)	F/g at 0.5 A/g	R_E (Ω)
rGO/CNT sphere	277.9	20.65	123.1	3.57
rGO/CNT sphere-CO_2-850	778.5	11.85	176.5	3.31
rGO/CNT sphere-CO_2-900	601.1	14.42	199.8	2.84

Figure 19. (a) ESI measurement, (b) magnified high frequency region, and (c) comparison of surface area and electrochemical performances of supercapacitor made of rGO/CNT spheres and porous rGO/CNT spheres activated with different temperatures.

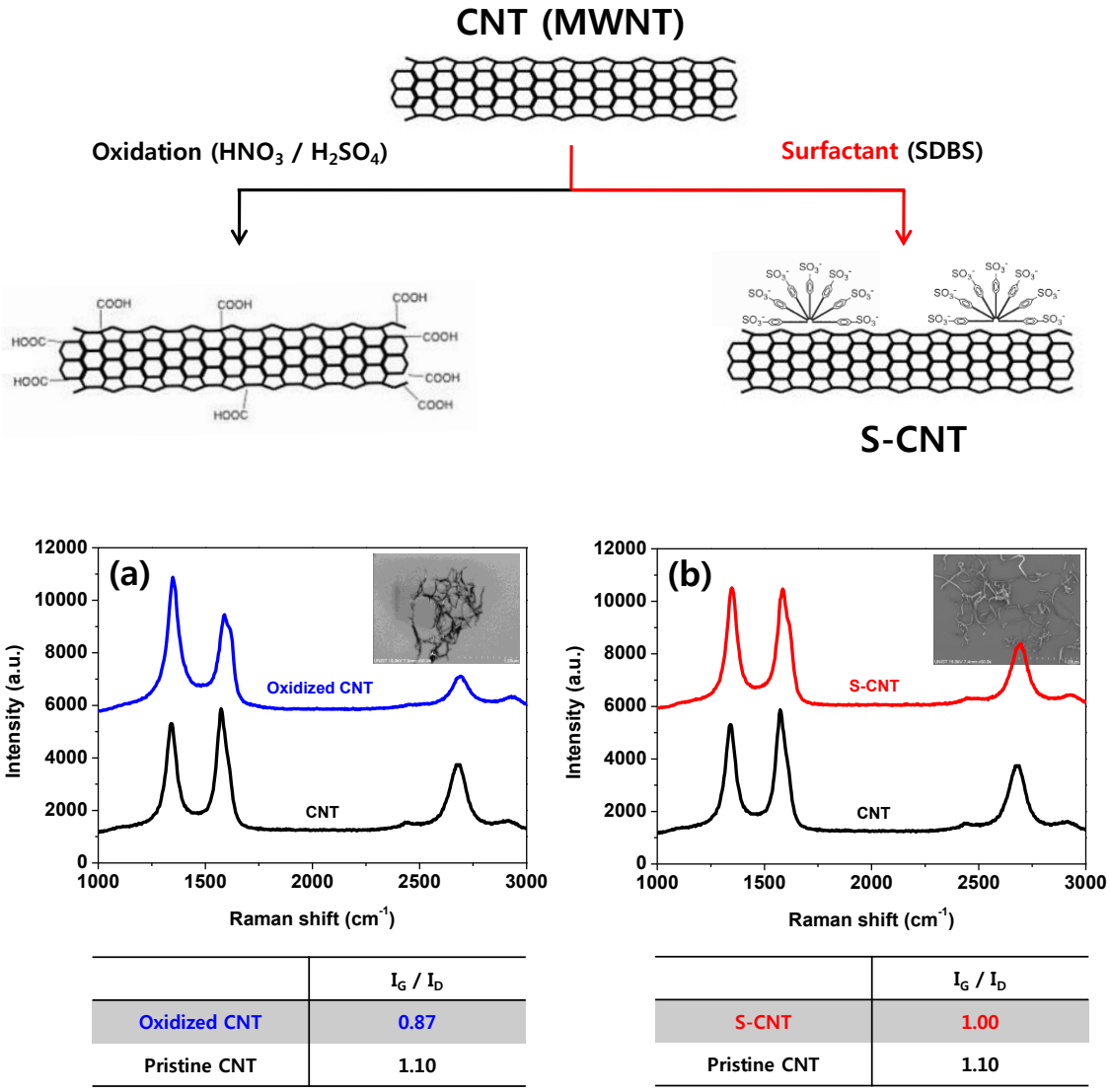

	I_G / I_D
Oxidized CNT	0.87
Pristine CNT	1.10

	I_G / I_D
S-CNT	1.00
Pristine CNT	1.10

Figure 20. Schematic description of preparation of oxidized CNT and surfactant-treated CNT. Comparison of Raman spectrum of (a) CNT and oxidized CNT, and (b) CNT and surfactant-treated CTN

structural defects, as demonstrated schematically in Figure 20. Note that slight increase of D band in S-CNT was supposed to have been affected by sp^3 carbon chains from SDBS. Raman spectrum can reflect the structural crystallinity and electrical conductivity of the carbon material including graphene and CNT. Therefore, it is expected that unoxidized S-CNT can provide better electrochemical performance of the rGO/CNT spheres by improving electrical conductivity.

The porous rGO/S-CNT spheres were successfully fabricated by microwave treatment of crumpled GO/S-CNT and followed CO_2 activation, which were the same method as the previous experiment. Morphologies and specific surface area of porous rGO/CNT-S spheres were characterized by SEM and BET analysis, and displayed in Figure 21 (a-c). Both rGO/S-CNT sphere and rGO/S-CNT activated at 900 ^oC (designated as "rGO/S-CNT sphere-CO_2-900") shows the sphere structure with ripples and wrinkles on their surface in common. The only difference was that no pores were found on the surface of rGO/S-CNT sphere, whereas we were able to observe the porous and rough surface from the surface of rGO/S-CNT sphere-CO_2-900 in Figure 21(b). From SEM results, it can be assumed that the two samples will show differences in specific surface area. Specific surface area of both samples was characterized by BET as shown in Figure 21(c). rGO/S-CNT spheres also exhibited a typical type IV of isotherm curves like rGO/CNT sphere, and the surface area and pore size were 317.2 m^2/g and 17.95 nm, respectively. On the other hand, a large increase in the specific surface area was observed in rGO/S-CNT sphere-CO_2-900 sample with 685.4 m^2/g of specific surface are and 13.62 nm of pore size, which were higher than that of as-prepared rGO/CNT-S sphere and CO_2-activated rGO/CNT in the same condition. Figure 22 shows the cyclic voltammetry (CV) profiles of the rGO/S-CNT sphere-CO_2-900 over a wide range of scan rates, and the results displayed a quasi-rectangular CV curve even at a high scan rate (100 mV/s). The symmetric charge and discharge curves revealed a reversible ion adsorption/desorption at electrode-electrolyte interfaces, and the specific capacitance of the rGO/CNT sphere-CO_2-900 at 0.5 A/g was calculated to be 225.1 F/g and it remained 44 % of its initial capacitance at a current density of 10 A/g (99.2 F/g) (Figure 22(d)). EIS was also performed to compare the ESR of each electrode, and Nyquist plots were shown in Figure 23 (a-b). In Figure 23 (b), an expanded view for high frequency range of Nyquist plots is displayed and the result revealed that rGO/S-CNT sphere-CO_2-900 shows 2.80 Ω, which is relatively lower than 3.05 Ω for as-prepared rGO/S-CNT sphere electrodes. Furthermore, the electrochemical performance of rGO/S-CNT sphere-CO_2-900 electrode shows a higher value than rGO/CNT sphere electrode, which could be explained as not only increase of ion diffusion resistance due to the higher surface area but also improvement of internal electrical resistance.

4. Conclusions

We have demonstrated the preparation of porous and three-dimensional rGO/CNT sphere through the spray drying system and CO_2 activation. This study also demonstrated the effective inhibition on

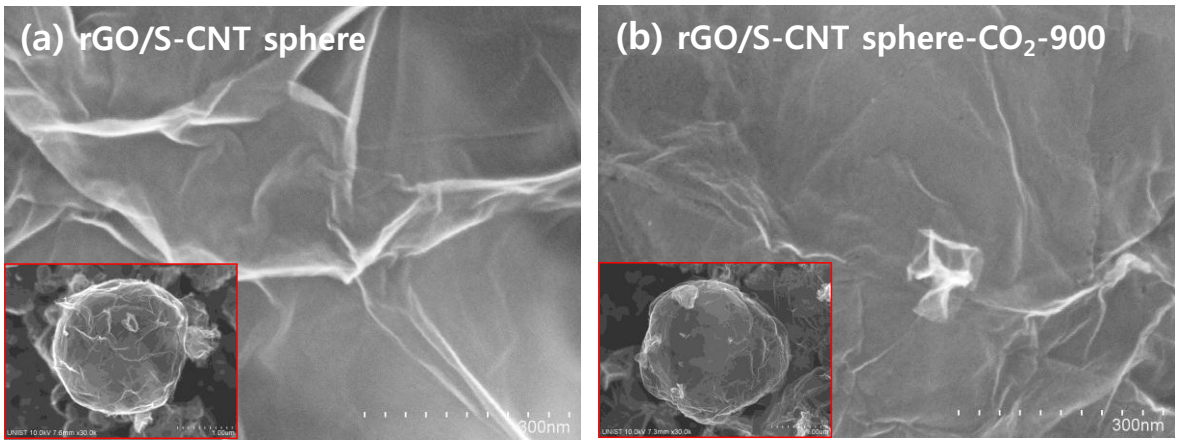

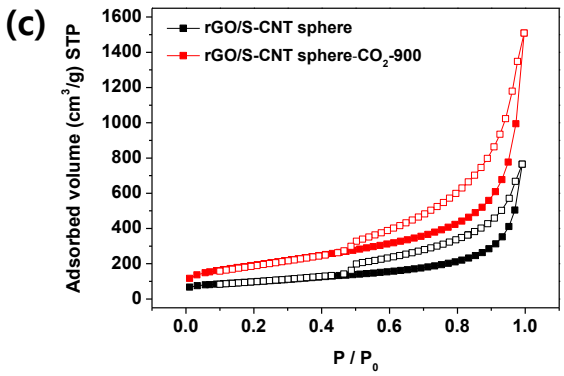

	SSA (m^2/g)	Pore size (nm)
rGO/S-CNT sphere	317.2	17.95
rGO/S-CNTsphere-CO_2-900	685.4	13.62

Figure 21. SEM images of (a) rGO/S-CNT sphere and (b) rGO/S-CNT sphere-CO_2-900. (c) N_2 adsorption and desorption isotherms and summarized surface area of rGO/S-CNT sphere and rGO/S-CNT sphere-CO_2-900.

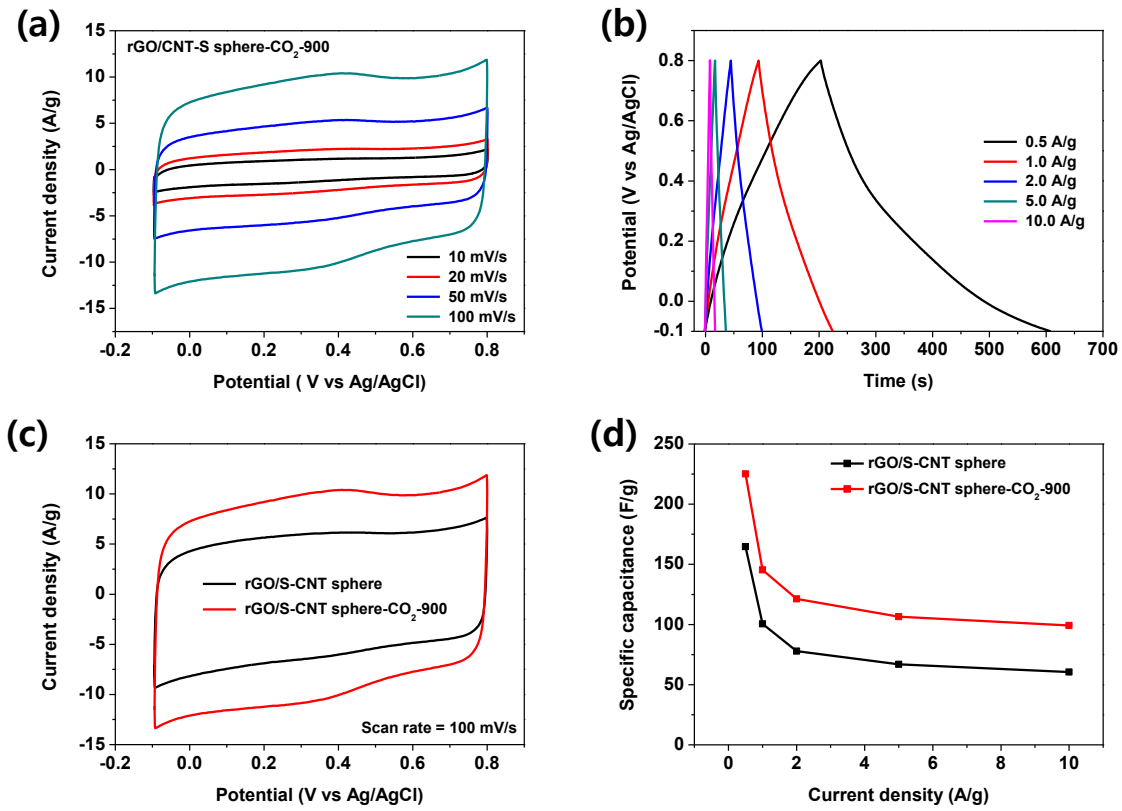

Figure 22. Capacitive performance of rGO/S-CNT spheres. (a) CV curves at various scan rates and (b) galvanotactic charge-discharge curves of rGO/S-CNT sphere-CO_2-900. (c) CV curves and (d) specific capacitance retention at different current densities with different samples.

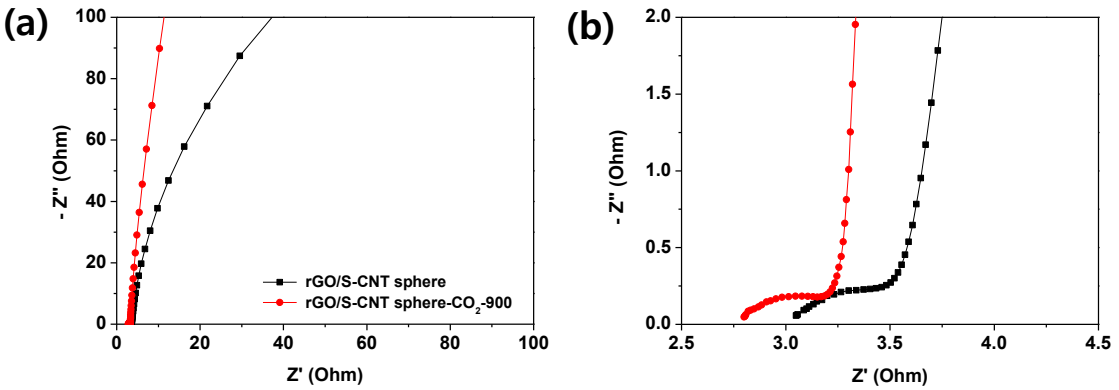

(c)

	SSA (m^2/g)	Pore size (nm)	F/g at 0.5 A/g	R_E (Ω)
rGO/S-CNT sphere	317.2	17.95	164.6	3.05
rGO/S-CNT sphere-CO_2-900	685.4	13.62	225.1	2.80

Figure 23. (a) ESI measurement, (b) magnified high frequency region, and (c) comparison of surface area and electrochemical performances of supercapacitor made of rGO/S-CNT spheres and rGO/S-CNT spheres-CO_2-900 samples.

the aggregation and restacking of rGO sheets by introducing CNT as a spacer. The porous and three-dimensional rGO/CNT spheres exhibited synergetic effects on enhancing the electrochemical capacitive performance. The specific capacitance of the porous rGO/S-CNT sphere showed 225.1 F/g at 0.5 A/g, which was higher than rGO/CNT (199 F/g). Thus, surface area as well as electrical conductivity were also important issue to enhance the graphene-based supercapacitor electrode. Considering the wide applications of graphene-based materials in electrochemistry. These results can be extended to improve the performance of different electrochemical systems, such as fuel cells, sensors and batteries.

5. References

1. Farghali, A.; Bahgat, M.; El Rouby, W.; Khedr, M., Preparation, decoration and characterization of graphene sheets for methyl green adsorption. *Journal of Alloys and Compounds* **2013,** *555*, 193-200.
2. Kamat, P. V., Graphene-based nanoarchitectures. Anchoring semiconductor and metal nanoparticles on a two-dimensional carbon support. *The Journal of Physical Chemistry Letters* **2009,** *1* (2), 520-527.
3. Novoselov, K. S.; Geim, A. K.; Morozov, S. V.; Jiang, D.; Zhang, Y.; Dubonos, S. V.; Grigorieva, I. V.; Firsov, A. A., Electric field effect in atomically thin carbon films. *science* **2004,** *306* (5696), 666-669.
4. Stankovich, S.; Dikin, D. A.; Dommett, G. H.; Kohlhaas, K. M.; Zimney, E. J.; Stach, E. A.; Piner, R. D.; Nguyen, S. T.; Ruoff, R. S., Graphene-based composite materials. *nature* **2006,** *442* (7100), 282-286.
5. Kamat, P. V., Graphene-based nanoassemblies for energy conversion. *The Journal of Physical Chemistry Letters* **2011,** *2* (3), 242-251.
6. Ng, Y. H.; Lightcap, I. V.; Goodwin, K.; Matsumura, M.; Kamat, P. V., To what extent do graphene scaffolds improve the photovoltaic and photocatalytic response of TiO2 nanostructured films? *The Journal of Physical Chemistry Letters* **2010,** *1* (15), 2222-2227.
7. Rao, C. e. N. e. R.; Sood, A. e. K.; Subrahmanyam, K. e. S.; Govindaraj, A., Graphene: the new two-dimensional nanomaterial. *Angewandte Chemie International Edition* **2009,** *48* (42), 7752-7777.
8. Dreyer, D. R.; Park, S.; Bielawski, C. W.; Ruoff, R. S., The chemistry of graphene oxide. *Chemical Society Reviews* **2010,** *39* (1), 228-240.
9. Luo, J.; Jang, H. D.; Sun, T.; Xiao, L.; He, Z.; Katsoulidis, A. P.; Kanatzidis, M. G.; Gibson, J. M.; Huang, J., Compression and aggregation-resistant particles of crumpled soft sheets. *ACS Nano* **2011,** *5* (11), 8943-8949.
10. Cranford, S. W.; Buehler, M. J., Packing efficiency and accessible surface area of crumpled graphene. *Physical Review B* **2011,** *84* (20), 205451.
11. Zhang, L.; Zhang, F.; Yang, X.; Long, G.; Wu, Y.; Zhang, T.; Leng, K.; Huang, Y.; Ma, Y.; Yu, A., Porous 3D graphene-based bulk materials with exceptional high surface area and excellent conductivity for supercapacitors. *Scientific reports* **2013,** *3*.
12. Balankin, A. S.; Ochoa, D. S.; León, E. P.; de Oca, R. C. M.; Rangel, A. H.; Cruz, M. Á. M., Power law scaling of lateral deformations with universal Poisson's index for randomly folded thin sheets. *Physical Review B* **2008,** *77* (12), 125421.
13. Balankin, A. S.; Huerta, O. S., Entropic rigidity of a crumpling network in a randomly folded thin

sheet. *Physical Review E* **2008,** *77* (5), 051124.

14. Ali, I., New generation adsorbents for water treatment. *Chemical Reviews* **2012,** *112* (10), 5073-5091.
15. Yang, K.; Xing, B., Adsorption of organic compounds by carbon nanomaterials in aqueous phase: Polanyi theory and its application. *Chemical reviews* **2010,** *110* (10), 5989-6008.
16. Conway, B. E., *Electrochemical supercapacitors: scientific fundamentals and technological applications*. Springer Science & Business Media: 2013.
17. Balaya, P., Size effects and nanostructured materials for energy applications. *Energy & Environmental Science* **2008,** *1* (6), 645-654.
18. Behl, M.; Yeom, J.; Lineberry, Q.; Jain, P. K.; Shannon, M. A., A regenerable oxide-based H2S adsorbent with nanofibrous morphology. *Nature Nanotechnology* **2012,** *7* (12), 810-815.
19. Bansal, R. C.; Donnet, J.-B.; Stoeckli, F., *Active carbon*. M. Dekker: 1988.
20. Zhu, Y.; Murali, S.; Stoller, M. D.; Ganesh, K.; Cai, W.; Ferreira, P. J.; Pirkle, A.; Wallace, R. M.; Cychosz, K. A.; Thommes, M., Carbon-based supercapacitors produced by activation of graphene. *Science* **2011,** *332* (6037), 1537-1541.
21. Zhang, L. L.; Zhao, X.; Stoller, M. D.; Zhu, Y.; Ji, H.; Murali, S.; Wu, Y.; Perales, S.; Clevenger, B.; Ruoff, R. S., Highly conductive and porous activated reduced graphene oxide films for high-power supercapacitors. *Nano Letters* **2012,** *12* (4), 1806-1812.
22. Wang, D. W.; Li, F.; Liu, M.; Lu, G. Q.; Cheng, H. M., 3D aperiodic hierarchical porous graphitic carbon material for high-rate electrochemical capacitive energy storage. *Angewandte Chemie* **2008,** *120* (2), 379-382.
23. Liu, C.; Li, F.; Ma, L. P.; Cheng, H. M., Advanced materials for energy storage. *Advanced Materials* **2010,** *22* (8).
24. Simon, P.; Gogotsi, Y., Materials for electrochemical capacitors. *Nature Materials* **2008,** *7* (11), 845-854.
25. Hong, T.-K.; Lee, D. W.; Choi, H. J.; Shin, H. S.; Kim, B.-S., Transparent, flexible conducting hybrid multilayer thin films of multiwalled carbon nanotubes with graphene nanosheets. *ACS Nano* **2010,** *4* (7), 3861-3868.
26. Priya, B.; Byrne, H., Investigation of sodium dodecyl benzene sulfonate assisted dispersion and debundling of single-wall carbon nanotubes. *The Journal of Physical Chemistry C* **2008,** *112* (2), 332-337.

Chapter 5: Effect of sheet morphology and porosity on the electrochemical activity of graphene-supported Pt catalyst for oxygen reduction reaction

1. Introduction

While the two-dimensional (2D) shape of graphene is desirable for many of its applications, it actually limits the potential of graphene to be realized in practical applications like catalyst, battery and supercapacitor, *etc.* For example, in supercapacitor, 2D graphene sheets can easily stack to form layered microstructures parallel to the current collectors, especially when compressed during electrode preparation. This could affect the device performance adversely in two ways: The effective surface area of the electrodes can be reduced due to aggregation of graphene sheets. The horizontal alignment of the graphene stacks can hinder electron and ion transport since both prefer the direction perpendicular to the current collector. Vertically aligned graphene sheets directly grown on the current collector have been reported and indeed showed outstanding ultracapacitor performance.[1]

The origin of the aggregation is the strong Van der Waals attraction between parallel sheets, which scales with the overlapping area (S) and fourth power of the inverse of separating distance (d) between sheets ($1/d^4$).[2] With the high aspect ratio of 2D morphology, graphene-based sheets are soft and tend to form conformal contact with a surface or each other, which very effectively increases S and reduces d, thus resulting in a strong attraction. To overcome the attraction, several general methods have been developed. Within the paradigm of colloidal chemistry, one can introduce electrostatic repulsion between the sheets by chemically tuning the surface charge of graphene and tailoring the graphene-solvent interactions.[3-5] On the other hand, one can insert molecular or nanostructured spacer materials to prevent the stacking of graphene sheets.[6] Recently, an alternative strategy was developed for making graphene resist aggregation by crumpling the 2D sheets into fractal-dimensional ball-like structure.[7] Crumpled graphene balls showed improved resistance for aggregation. Since crumpled graphene balls have more open structure, they can have relatively higher specific surface area than the stacked graphene sheets. Nevertheless, ions are difficult to stabilize and diffuse in the graphene without defects, and the performance of graphene-based electrodes normally suffers from severe graphene aggregation, which would inevitably hinder inferior ionic accessibility.[8-10] Therefore, a better design of a graphene structure is essential to improve the performance of graphene in electrochemical devices.

Compared to the intrinsic structure of graphene-based materials, porous graphene has a larger specific surface area and a larger number of additional defects in the basal plane of graphene, which increases the number of electrochemical active reversible storage sites.[11-15] Porous graphene with well-defined pores (2–300 nm) can further accelerate the ion diffusion kinetics and minimize the ion insertion/extraction distance.[16-18] In addition, introducing a carbon vacancy into graphene network increased adsorption energy of the clusters and graphene flakes containing five or seven rings

increased the adsorption energy of the clusters more than a flat, defect-free graphene sheet.[19]

Recently, porous graphene have shown that introducing holes through the nanosheet basal plane could be an extremely efficient strategy to achieve much improved volumetric performance.[20-21] Different from the pore generation in which physical space is created between the intact nanosheets, and porous graphene is synthesized by chemically etching the basal plane of nanosheet. Among a handful of available strategies, nanolithography methods were used to prepare the porous graphene with highly periodic arrays of evenly distributed size holes, however these methods are not scalable.[22-24] For large-scale preparation but with less precision in hole size distribution, several methods were reported, such as etching with steam,[14] refluxing or sonicating with nitric acid,[25-26] chemical activation,[15] catalytic oxidation using metal or metal oxide nanoparticles,[27-28] enzymatic oxidation,[29] and photocatalytic oxidation.[30] Although the porous structure of graphene may have relatively higher electrical resistance because of the partial removal of the carbon atoms on the basal plane of graphene sheets, ions or gas species can be easily transported through the porous structures.[31] Based on its structural features, three-dimensional and porous graphene can be considered to be an ideal supporter for maximization of the accessible surface areas and the development of high-performance Pt-based catalyst.

Herein, we demonstrate a simple method for preparing a superior electrocatalyst based on porous crumpled reduced graphene oxide and platinum (rGO/Pt) for oxygen reduction reaction (ORR). The porous crumpled rGO/Pt was fabricated from colloidal mixture of GO and $H_2PtCl_6 \cdot 6H_2O$ through spray drying followed by thermal reduction. We also examined the effect of sheet morphology and porosity on the electrochemical activity of rGO-supported Pt catalyst for oxygen reduction reaction. Since the crumpled and porous morphology inhibits the formation of re-stacked layered structures of rGO sheets, it results in a microstructure for both electron and ion transport. Therefore, this morphology should be more desirable than the flat or even wrinkled sheets for rGO-based electrocatalyst.

2. Experimental section

2.1. Materials

Graphite (SP-1, Baycarbon), H_2SO_4 (98 %, Merck), $KMnO_4$ (99 %, Sigma) and Chloroplatinic acid hexahydrate ($H_2PtCl_6 \cdot 6H_2O$, Sigma-Aldrich) were used as received without further purification.

2.2. Preparation of GO

Graphite oxide was prepared from purified natural graphite (SP-1, Bay Carbon) using the modified Hummers method.[32] Graphite powder (2.0 g) was added to concentrated H_2SO_4 (46 mL), and $KMnO_4$ (6.0 g) was added gradually with stirring and cooling, while the temperature of the mixture was

maintained below 20 °C. The mixture was then stirred at 35 °C for 2 hr, and distilled water (92 mL) was added. After 15 min, the reaction was terminated by the addition of a large amount of distilled water (280 mL) and a 30% H_2O_2 solution (5.0 mL), after which the color of the mixture changed from black to bright yellow. The mixture was centrifuged at 4000 rpm and washed with a 1:10 HCl solution (500 mL) in order to remove metal ions. The graphite oxide product was suspended in distilled water producing a viscous, brown dispersion, which was subjected to dialysis to completely remove metal ions and acids. To obtain the GO dispersion, the graphite oxide was exfoliated by ultrasonication (Sonic Dismembrator Model 500, Fisher Scientific) at 100 W for 15 min and then centrifugation at 4000 rpm for 10 min.

2.3. Fabrication of porous and crumpled rGO-supported Pt catalyst

The colloidal mixture of GO and $H_2PtCl_6 \cdot 6H_2O$ were used as starting materials for porous and crumpled rGO-supported Pt catalyst, and their weight ratio was 1:0.5 with the concentration of GO in colloidal mixture fixed at 0.5 mg/mL. Then, crumpled rGO/Pt was fabricated by the spray dryer (Buchi B-90 spray dryer) followed by thermal annealing at 900 °C (ramp: 5 °C/min) in a vacuum for 3 hr. In this process, micrometer-sized droplets of dispersion were produced by the atomizer (Nozzel with 7.0 μm) of the spray dryer. The droplets were carried away and dried by inflow warm air (120 °C) to produce powder particles. The dry powders were settled by a cyclone separator and the air was discharged from the separator along with small particles. The atomizer pressure was about 30 mbar and the hot air temperature was 120 °C. In all experiments, 30-40 % of the spray rate was used for spraying the dispersions.

The porous crumpled rGO/Pt samples were prepared in a single-step air oxidation process by directly heating the starting crumpled rGO/Pt sample in static air at an elevated temperature in an open-ended tube furnace. The samples were prepared at 350 °C and held for 3 hr, and then, thermally reduced at 900 °C (ramp: 5 °C/min) in a vacuum for 3 hr to remove oxidized carbon in rGO.

2.4. Electrode preparation.

Catalyst inks were prepared by dispersing a catalyst and a conducting agent in 0.45 ml of ethanol, 0.45 ml of isopropyl alcohol and 0.1 ml of 5 wt% nafion solution (Sigma-Aldrich 274704). The total amount of the catalyst and the conducting agent was fixed at 20 mg. Carbon black (C; Akzo Nobel Ketjenblack 600JD) was used as the conducting agent, and the catalyst ink was dropped on the disk compartment of ring-disk electrodes. For comparison, 20 wt% platinum nanoparticles supported by carbon black (Pt/C; Premetek P10A200) was used as a control.

2.5. Characterization

The morphology of the flat rGO, crumpled rGO, and crumpled rGO/Pt was analyzed using and

scanning electron microscope (SEM, FEI VERIOS 460). Atomic resolution microscopy was performed with high-resolution transmission electron microscope (HR-TEM, JEOL JEM-2100F). Chemical structures of samples were identified by X-ray photoelectron spectroscopy (XPS) using ESCALAB250Xi (Thermo Scientific) equipped with monochromatic Al K-Alpha source.

Cyclic voltammograms (CV) were obtained on disk and ring electrodes simultaneously by a bipotentiostat (iviumstat, Ivium Technologies). Ring-disk electrodes (RDE) of glassy carbon disk and platinum ring was used as the working electrode (disk area = 0.1256 cm^2) while a platinum wire and a Hg/HgO electrode were used as the counter and reference electrodes respectively. The RDEs were rotated at various controlled speeds (1600 rpm unless otherwise indicated) by a RDE controller (ALS RRDE-3A). An aqueous solution of 0.1M KOH was used as the electrolyte. ORR polarization curves were obtained on the disk electrode from a cathodic sweep from 0.1 to -0.8 V (vs. Hg/HgO) at 10 mV/s after five cycles of CVs.

3. Results and discussion

Crumpled rGO/Pt were made by isotropic capillary force in rapidly evaporating droplet of GO suspension including Pt precursor using nanospray drying setup, and followed by a thermal reduction. Specifically, GO concentration was kept at 0.5 mg/mL, and used as synthesized without further pH tuning. Upon drying of drop solution, rGO paper was obtained with ordered layered structure. Scanning electron microscopy (SEM) studies in Figure 1 reveals that microstructure of rGO/Pt materials of the three different morphologies agree with the corresponding paper models. For each sample, SEM images were obtained at both the low and high magnified surface. As expected, the flat rGO/Pt pack like a stack of paper with smooth corrugation and ordered lamellar cross section (Figure 1(a)). For the crumpled rGO/Pt (Figure 1(c)), although the morphology of individual particles was largely unchanged after thermal reduction, we were able to identify the newly formed platinum nanoparticles on the surface (Figure 1(d)). It shall be noted that there is free space inside each crumpled rGO/Pt particle as well as between them. Thus, crumpled rGO/Pt should be less dense that that of flat rGO/Pt structure. In order to obtain porous rGO, crumpled rGO/Pt samples were subjected to controlled in air oxidation via heating in an open-ended tube furnace. As shown in Figure 1(e and f), after oxidation treatment of crumpled rGO/Pt at 350 ^oC for 3 hr, significant number of holes appeared on the originally intact crumpled rGO surfaces (starting at this point it is now designated as ‘porous crumpled rGO/Pt’). The as-prepared crumpled rGO/Pt, where a vacuumed atmosphere was used, could be viewed as the control sample for porous crumpled rGO/Pt. Therefore, the observed pores clearly indicate that Pt nanoparticles catalyzed the oxidation of rGO surfaces. The catalytic role of metal nanoparticles to the oxidation of graphitic carbon such as graphite and CNT has been known for a few decades and sometimes referred to as catalytic carbon gasification as CO and CO_2 are generated during the process.[33-35] More recently, it was reported that their traces were able to be formed on a

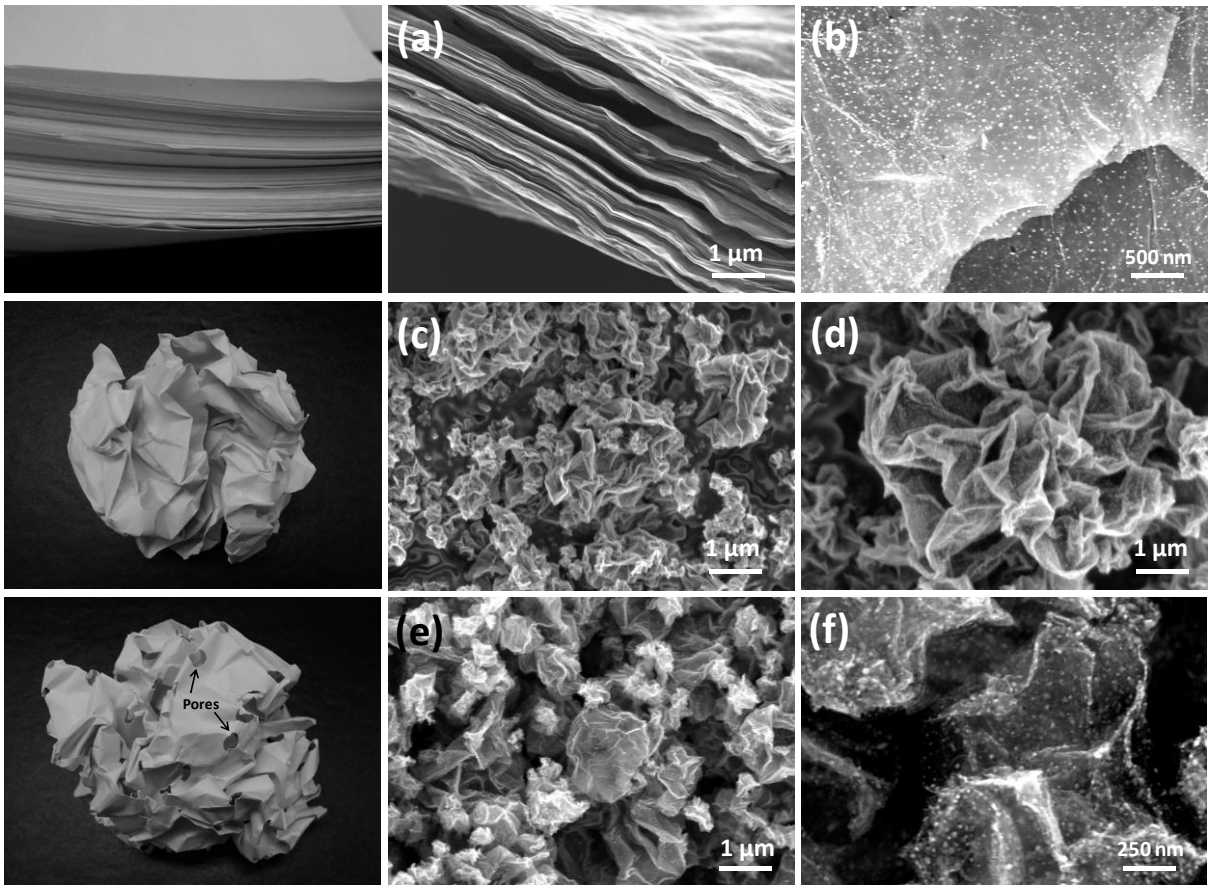

Figure 1. Paper models and SEM images of (a and b) flat rGO/Pt, (c and d) crumpled rGO/Pt and (e and f) porous crumpled rGO/Pt.

highly oriented pyrolytic graphite (HOPG) substrates.[36] This is analogous to our experiments, which were carried out in rGO as the substrate. It is plausible that the Pt nanoparticle-catalyzed thermal oxidation of crumpled rGO started at the well-conformed contact area between Pt and rGO.

To ensure the porous structure, high-resolution transmission electron microscopy (HR-TEM) was conducted as shown in Figure 2. Most holes were associated with at least on Pt particle. Some holes also appeared as tracks, which were apparently associated with directional motion of the attached Pt nanoparticles under the given conditions. This was likely due to etching-induced motions (Figure 2(a)). As shown in our previous studies, since the number of crumpled rGO sheets were 11-14 layers thick, the catalytic oxidation of carbon on crumpled rGO could penetrate through all layers in most case (Figure 2(b)). Each hole or track, which might not have originated from multiple adjacent Pt nanoparticles, could merge to form branched tracks or one single hole (Figure 2(c and d)). Although the diameter of the contact area between Pt and rGO was smaller than the corresponding Pt nanoparticle, the diameters of the holes including the width of the etching-induced tracks could be equivalent or even slightly larger than the diameter of the corresponding Pt nanoparticles. This might be due to the unbalanced etching-induced motion of non-spherical Pt nanoparticles. The motion of noble metal nanoparticles on graphitic surface should be self-rotation along with movements in a slightly spiral and zig-zag fashion.[36] The rather rough edges of the holes and tracks might also have originated from such unbalanced movement of Pt nanoparticles.

The X-ray diffraction (XRD) patterns of the as-prepared flat, crumpled and porous crumpled rGO/Pt are shown in Figure 3. The results exhibited the characteristic face-centered cubic (FCC) Pt lattice: diffraction peak at 39.8 ^{o} for Pt (111), 46.2^{o} for Pt (200) and 67.5 ^{o} for Pt (220), confirming that the Pt precursor has been completely reduced to Pt nanoparticles during the thermal reduction at 900 ^{o}C (Figure 3(a)). Moreover, a small and broad diffraction of graphitic carbon (002) at around 26 ^{o} appeared. This was attributed to the restacked and layered structure of rGO sheets, indicating the sufficient reduction of GO. Compared to “Flat rGO/Pt” samples, the (002) diffraction peak intensity of crumpled and porous crumpled rGO/Pt was markedly reduced and dramatically broadened, which means that regular stacks of rGO sheets were inhibited by the crumpled structure (Figure 3(b)). In addition, a larger increase in full width at half maximum (FWHM) of (002) peak in porous crumpled rGO/Pt is also noted, which is consistent with the presence of high density of pores.

Further characterizations by X-ray photoelectron spectroscopy (XPS) were performed to examine the chemical structure of rGO/Pt composites. The C 1s XPS spectrum of GO/H_2PtCl_6 clearly indicates a considerable degree of oxidation with four components that correspond to carbon atoms in different functional groups (Figure 4(a and b)). Deconvolution revealed the presence of C-C/C=C (284.1 eV), the C C–O (285.7 eV), C=O (286.2 eV), and the carboxylate carbon (O–C=O, 287.5 eV). Although the C 1s XPS spectrum of porous crumpled rGO/Pt also exhibit the same oxygen functionalities that have been assigned for GO/H_2PtCl_6, the peak intensities of these components in the reduced samples

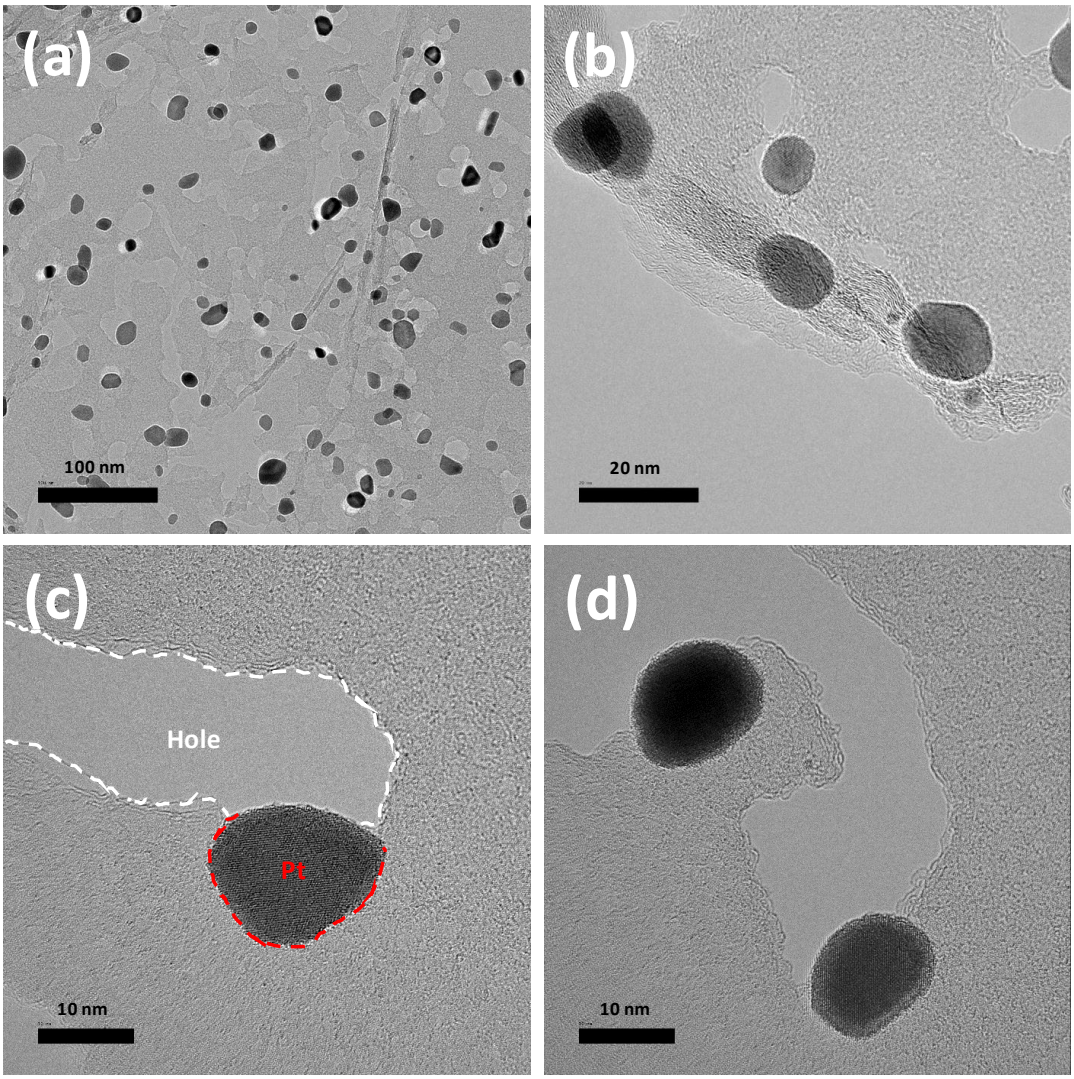

Figure 2. HR-TEM images of porous crumpled rGO/Pt

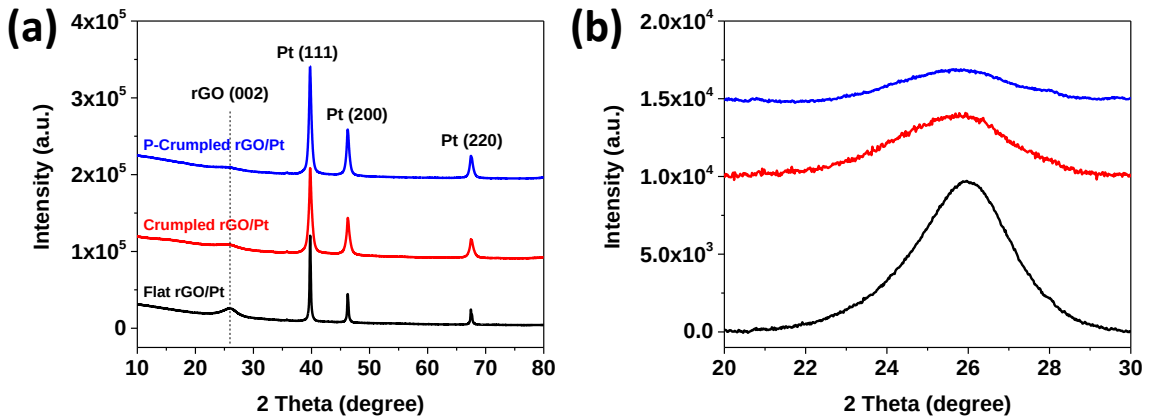

Figure 3. (a) XRD patterns and (b) the rGO (002) region of flat, crumpled and porous crumpled rGO/Pt.

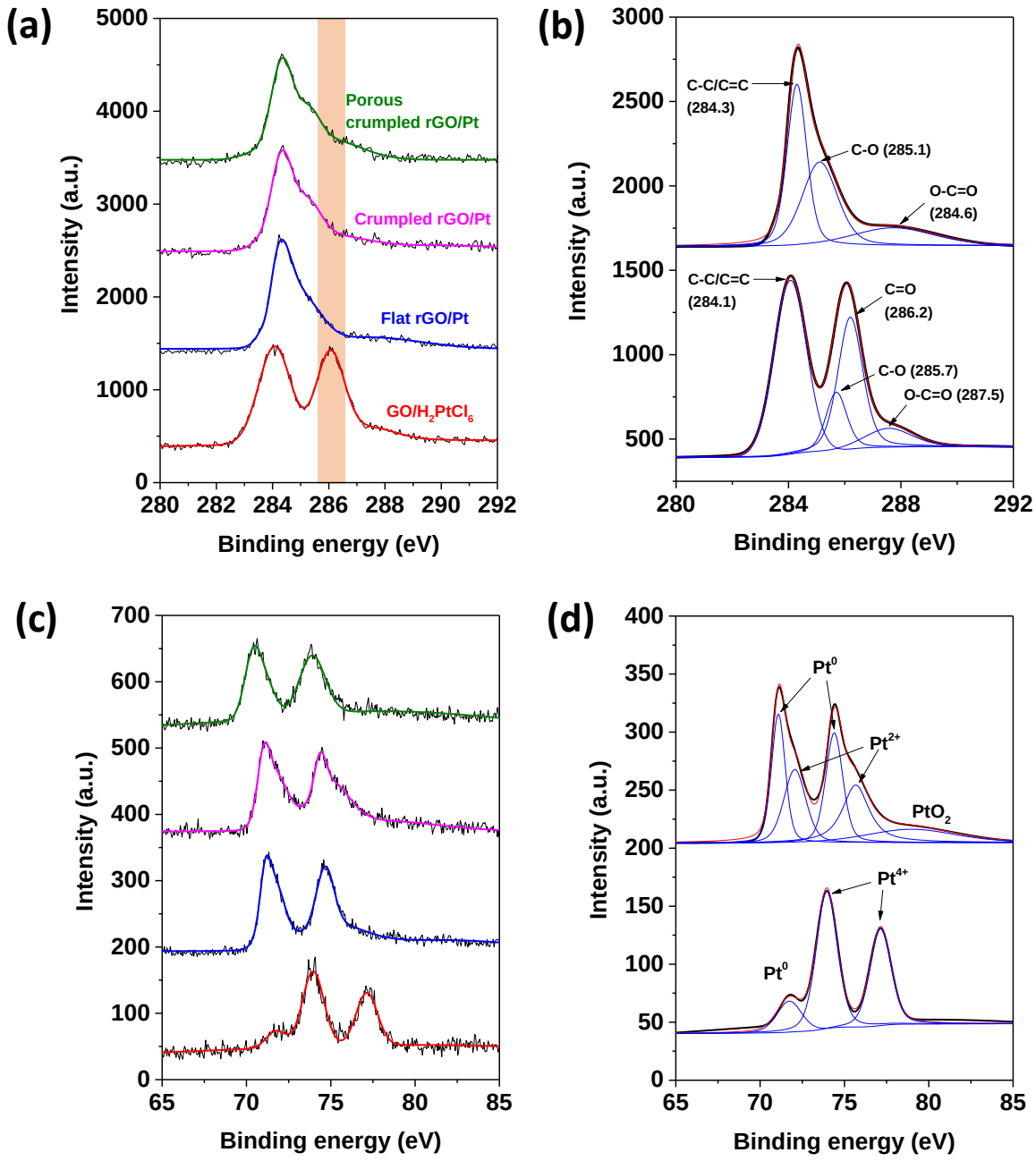

Figure 4. Raw and deconvoluted XPS spectra in (a) C 1s and (b) Pt 4f region of GO/H_2PtCl_6, Flat, crumpled and porous crumpled rGO/Pt produced by thermal reduction at 900 °C.

are much smaller than those in the GO, indicating considerable de-oxygenation by the thermal reduction at 900 °C. In order to identify the chemical bonding between the Pt nanoparticles and rGO, we measured the XPS spectra of Pt 4f, and presented in Figure 4(c and d). The Pt 4f signal of GO/H_2PtCl_6 was deconvoluted into three components. The binding energies were located at 71.7, 73.9 and 77.1 eV, which were assigned to Pt^0 and Pt^{4+} species, respectively. Note that Pt^0 originated from partial reduction of H_2PtCl_6 through the spray drying process with 120 °C inlet flow air. On the other hand, porous crumpled rGO/Pt showed the peaks located to 71.1 (Pt $4f_{7/2}$) and 74.3 eV (Pt $4f_{5/2}$) which were assigned to Pt^0. This is where, the weaker ones were detected at 72.0 (Pt $4f_{7/2}$) and 75.6 eV (Pt $4f_{5/2}$) and they corresponded to Pt^{2+} in PtO. From XPS results, we could confirm that the rGO and Pt nanoparticles were effectively reduced by thermal annealing at 900 °C, and the results were in a good agreement with XRD results.

In order to evaluate the electrocatalytic performance of rGO/Pt composite catalysts, oxygen reduction reaction (ORR) measurements were further conducted in 0.1 M KOH aqueous solution using glassy carbon rotating disk electrode (GC RDE) at room temperature. Figure 5 shows the ORR polarization curves for the flat, crumpled, porous crumpled rGO/Pt and commercial Pt/C catalyst. The half-wave potential ($E_{1/2}$) of flat, crumpled and porous crumpled rGO/Pt was determined to be -0.152, -0.132 and -0.065 V, respectively (see summarized table in Figure 5). For porous crumpled rGO/Pt, its $E_{1/2}$ was only 10 mV higher than commercial Pt/C (-0.075 V) catalyst. This value is very comparable to that observed for the rGO-supported Pt catalyst in literature. It shall be noted that there is more free space inside individual crumpled and porous crumpled rGO/Pt as well as between them. Therefore, the crumpled structures should be less dense than that of the flat structure. Indeed, the former has large and segregated voids inside and between the particles, which should be more favorable for the ionic flow and electron transport for ORR catalysts.[37]

In addition to the activity of catalysts, durability is another important parameter to evaluate their performance in the ORR. In order to assess their ability to sustain activity, we have performed durability tests by applying a cyclic potential sweep between -0.8 and 0.1 V at a sweep rate of 10 mV/s and a rotation speed of 1,600 rpm in O_2-saturated 0.1 M KOH aqueous solution at room temperature. As mentioned above, of porous crumpled rGO/Pt catalyst exhibited comparable ORR activity to Pt/C and, besides, it showed high durability of 90 % after 10 hr cycle test, which was 15 % higher than commercial Pt/C (Figure 6(a and b)). Furthermore, Figure 6(c) showed that the half-wave potential of porous crumpled rGO/Pt remained high after durability test after 10,000 cycles, and even a positive shift of 37 mV at 3 mA/cm^2. In contrast, the Pt/C catalyst showed significantly reduced diffusion-limiting currents (Figure 6(d)). It indicates that part of Pt nanoparticles has dissolved, agglomerated and detached from rGO supporter, raising the concern that the Pt/C has limited binding to the electrode. This feature should be ascribed to the relatively strong interaction of Pt nanoparticle with porous and crumpled structure of rGO.

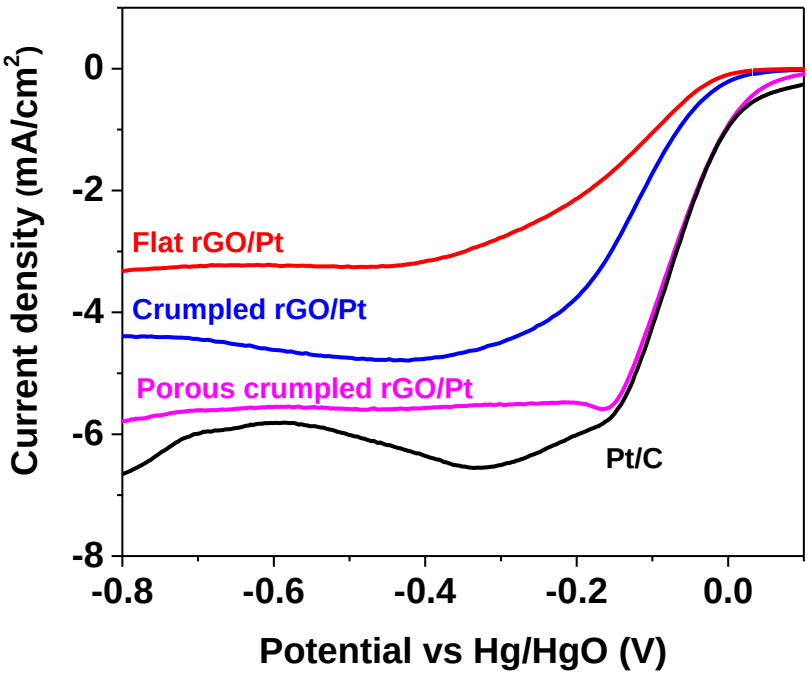

	Flat rGO/Pt	Crumpled rGO/Pt	Porous crumpled rGO/Pt	Pt/C
$E_{1/2}$ (V vs. Hg/HgO)	-0.152	-0.132	-0.065	-0.075
E (*i* at -3 mA/cm^2)	-0.347	-0.157	-0.072	-0.069

Figure 5. ORR polarization curves of flat, crumpled and porous crumpled rGO/Pt samples with commercial Pt/C.

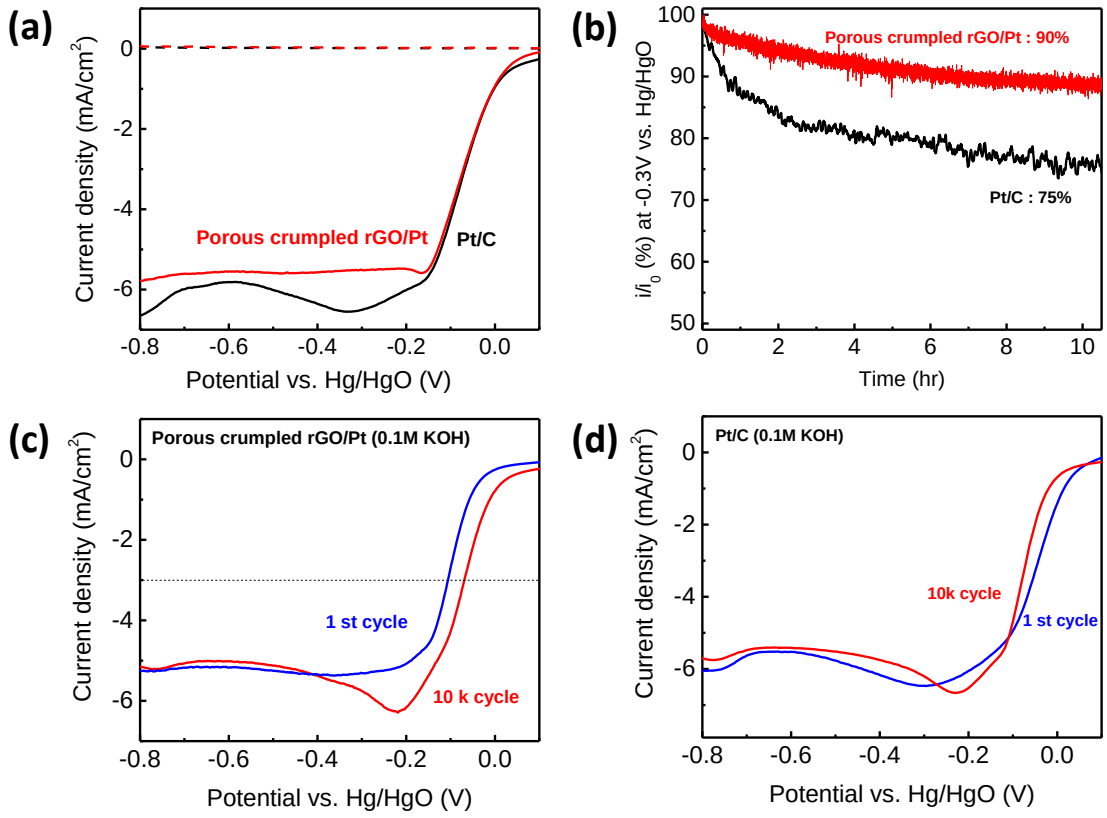

Figure 6. (a) Initial polarization curves and (b) ORR chronoamperometric response of porous crumpled rGO/Pt and Pt/C at a constant voltage of 0.3 V. (c-d) Durability tests of porous crumpled rGO/Pt and Pt/C by running ORR rection after 10000 cycles. All tests were performed in O_2-saturated 0.1 KOH solution at scan rate 10 mV/s.

4. Conclusions

In conclusion, converting flat rGO into crumpled and porous crumpled morphology can significantly improve the electrocatalytic performance of rGO-supported Pt catalyst. The aggregation-resistant properties of the crumpled structure of rGO/Pt allows them to have a better ion-accessible surface than that of the flat rGO/Pt. Moreover, porous crumpled rGO/Pt from controlled air oxidation exhibited through-the-thickness holes and enhanced electrocatalytic performance in terms of durability in comparison with the crumpled rGO/Pt and commercial Pt/C catalyst. The increased electroatalytic activity could be closely related the increase in specific surface area of rGO. Therefore, porous crumpled rGO/Pt shed a light on the design and fabrication of architectures for a high-performance ORR catalyst.

5. References

1. Miller, J. R.; Outlaw, R.; Holloway, B., Graphene double-layer capacitor with ac line-filtering performance. *Science* 2010, *329* (5999), 1637-1639.
2. Brennan, R. O., The interlayer binding in graphite. *The Journal of Chemical Physics* 1952, *20* (1), 40-48.
3. Eda, G.; Chhowalla, M., Chemically derived graphene oxide: towards large-area thin-film electronics and optoelectronics. *Advanced Materials* 2010, *22* (22), 2392-2415.
4. Allen, M. J.; Tung, V. C.; Kaner, R. B., Honeycomb carbon: a review of graphene. *Chemical reviews* 2009, *110* (1), 132-145.
5. Huang, X.; Qi, X.; Boey, F.; Zhang, H., Graphene-based composites. *Chemical Society Reviews* 2012, *41* (2), 666-686.
6. Yu, D.; Dai, L., Self-assembled graphene/carbon nanotube hybrid films for supercapacitors. *The Journal of Physical Chemistry Letters* 2009, *1* (2), 467-470.
7. Luo, J.; Jang, H. D.; Sun, T.; Xiao, L.; He, Z.; Katsoulidis, A. P.; Kanatzidis, M. G.; Gibson, J. M.; Huang, J., Compression and aggregation-resistant particles of crumpled soft sheets. *ACS Nano* 2011, *5* (11), 8943-8949.
8. Wang, Z.-L.; Xu, D.; Wang, H.-G.; Wu, Z.; Zhang, X.-B., In situ fabrication of porous graphene electrodes for high-performance energy storage. *ACS Nano* 2013, *7* (3), 2422-2430.
9. Reddy, A. L. M.; Srivastava, A.; Gowda, S. R.; Gullapalli, H.; Dubey, M.; Ajayan, P. M., Synthesis of nitrogen-doped graphene films for lithium battery application. *ACS Nano* 2010, *4* (11), 6337-6342.
10. Pan, D.; Wang, S.; Zhao, B.; Wu, M.; Zhang, H.; Wang, Y.; Jiao, Z., Li storage properties of disordered graphene nanosheets. *Chemistry of Materials* 2009, *21* (14), 3136-3142.
11. Carr, L. D.; Lusk, M. T., Defect engineering: Graphene gets designer defects. *Nature Nanotechnology* 2010, *5* (5), 316.
12. Han, S.; Wu, D.; Li, S.; Zhang, F.; Feng, X., Porous graphene materials for advanced electrochemical energy storage and conversion devices. *Advanced Materials* 2014, *26* (6), 849-864.
13. Ning, G.; Fan, Z.; Wang, G.; Gao, J.; Qian, W.; Wei, F., Gram-scale synthesis of nanomesh graphene with high surface area and its application in supercapacitor electrodes. *Chemical Communications* 2011, *47* (21), 5976-5978.
14. Han, T. H.; Huang, Y.-K.; Tan, A. T.; Dravid, V. P.; Huang, J., Steam etched porous graphene oxide network for chemical sensing. *Journal of the American Chemical Society* 2011, *133* (39), 15264-15267.
15. Zhu, Y.; Murali, S.; Stoller, M. D.; Ganesh, K.; Cai, W.; Ferreira, P. J.; Pirkle, A.; Wallace, R.

M.; Cychosz, K. A.; Thommes, M., Carbon-based supercapacitors produced by activation of graphene. *Science* 2011, *332* (6037), 1537-1541.

16. Yang, S.; Feng, X.; Wang, L.; Tang, K.; Maier, J.; Müllen, K., Graphene-Based Nanosheets with a Sandwich Structure. *Angewandte Chemie International Edition* 2010, *49* (28), 4795-4799.
17. Sun, B.; Huang, X.; Chen, S.; Munroe, P.; Wang, G., Porous graphene nanoarchitectures: an efficient catalyst for low charge-overpotential, long life, and high capacity lithium–oxygen batteries. *Nano Letters* 2014, *14* (6), 3145-3152.
18. Fang, Y.; Lv, Y.; Che, R.; Wu, H.; Zhang, X.; Gu, D.; Zheng, G.; Zhao, D., Two-dimensional mesoporous carbon nanosheets and their derived graphene nanosheets: synthesis and efficient lithium ion storage. *Journal of the American Chemical Society* 2013, *135* (4), 1524-1530.
19. Okamoto, Y., Density-functional calculations of icosahedral M 13 (M= Pt and Au) clusters on graphene sheets and flakes. *Chemical Physics Letters* 2006, *420* (4), 382-386.
20. Xu, Y.; Lin, Z.; Zhong, X.; Huang, X.; Weiss, N. O.; Huang, Y.; Duan, X., Holey graphene frameworks for highly efficient capacitive energy storage. *Nature communications* 2014, *5*.
21. Han, X.; Funk, M. R.; Shen, F.; Chen, Y.-C.; Li, Y.; Campbell, C. J.; Dai, J.; Yang, X.; Kim, J.-W.; Liao, Y., Scalable holey graphene synthesis and dense electrode fabrication toward high-performance ultracapacitors. *ACS Nano* 2014, *8* (8), 8255-8265.
22. Sinitskii, A.; Tour, J. M., Patterning graphene through the self-assembled templates: toward periodic two-dimensional graphene nanostructures with semiconductor properties. *Journal of the American Chemical Society* 2010, *132* (42), 14730-14732.
23. Liang, X.; Jung, Y.-S.; Wu, S.; Ismach, A.; Olynick, D. L.; Cabrini, S.; Bokor, J., Formation of bandgap and subbands in graphene nanomeshes with sub-10 nm ribbon width fabricated via nanoimprint lithography. *Nano Letters* 2010, *10* (7), 2454-2460.
24. Bai, J.; Zhong, X.; Jiang, S.; Huang, Y.; Duan, X., Graphene nanomesh. *Nature Nanotechnology* 2010, *5* (3), 190-194.
25. Wang, X.; Jiao, L.; Sheng, K.; Li, C.; Dai, L.; Shi, G., Solution-processable graphene nanomeshes with controlled pore structures. *Scientific reports* 2013, *3*.
26. Zhao, X.; Hayner, C. M.; Kung, M. C.; Kung, H. H., Flexible holey graphene paper electrodes with enhanced rate capability for energy storage applications. *ACS Nano* 2011, *5* (11), 8739-8749.
27. Zhao, Y.; Hu, C.; Song, L.; Wang, L.; Shi, G.; Dai, L.; Qu, L., Functional graphene nanomesh foam. *Energy & Environmental Science* 2014, *7* (6), 1913-1918.
28. Lin, Y.; Watson, K. A.; Kim, J.-W.; Baggett, D. W.; Working, D. C.; Connell, J. W., Bulk preparation of holey graphene via controlled catalytic oxidation. *Nanoscale* 2013, *5* (17), 7814-7824.

29. Kotchey, G. P.; Hasan, S. A.; Kapralov, A. A.; Ha, S. H.; Kim, K.; Shvedova, A. A.; Kagan, V. E.; Star, A., A natural vanishing act: the enzyme-catalyzed degradation of carbon nanomaterials. *Accounts of Chemical Research* 2012, *45* (10), 1770-1781.

30. Radich, J. G.; Kamat, P. V., Making graphene holey. Gold-nanoparticle-mediated hydroxyl radical attack on reduced graphene oxide. *ACS Nano* 2013, *7* (6), 5546-5557.

31. Zhang, L. L.; Zhao, X.; Stoller, M. D.; Zhu, Y.; Ji, H.; Murali, S.; Wu, Y.; Perales, S.; Clevenger, B.; Ruoff, R. S., Highly conductive and porous activated reduced graphene oxide films for high-power supercapacitors. *Nano Letters* 2012, *12* (4), 1806-1812.

32. Hummers, W. S.; Offeman, R. E., Preparation of graphitic oxide. *Journal of the American Chemical Society* 1958, *80* (6), 1339-1339.

33. Wang, X.; Pan, Y.; Wang, J.; Tian, Y., Synthesis of magnetic dual-mesoporous carbon spheres and lysozyme release behavior. *Microporous and Mesoporous Materials* 2013, *180*, 257-261.

34. García, A.; Nieto, A.; Vila, M.; Vallet-Regí, M., Easy synthesis of ordered mesoporous carbon containing nickel nanoparticles by a low temperature hydrothermal method. *Carbon* 2013, *51*, 410-418.

35. Weisweiler, W.; Subramanian, N.; Terwiesch, B., Catalytic influence of metal melts on the graphitization of monolithic glasslike carbon. *Carbon* 1971, *9* (6), 755-761.

36. Severin, N.; Kirstein, S.; Sokolov, I.; Rabe, J., Rapid trench channeling of graphenes with catalytic silver nanoparticles. *Nano Letters* 2008, *9* (1), 457-461.

37. Luo, J.; Jang, H. D.; Huang, J., Effect of sheet morphology on the scalability of graphene-based ultracapacitors. *ACS Nano* 2013, *7* (2), 1464-1471.

[Publication lists]

1. Dong Wook Lee, Tae-Keun Hong, **Dongwoo Kang**, Jisook Lee, Mihee Heo, Jin Young Kim, Byeong-Su Kim and Hyeon Suk Shin, "Highly controllable transparent and conducting thin films using layer-by-layer assembly of oppositely charged reduced graphene oxides", J. Mater. Chem., 2011,21, 3438-3442
2. **Dongwoo Kang** and Hyeon Suk Shin, "Control of size and physical properties of graphene oxide by changing the oxidation temperature", Carbon Letters, 2012, 13, 39-43
3. Bo Ram Lee, Jung-woo Kim, **Dongwoo Kang**, Dong Wook Lee, Seo-Jin Ko, Hyun Jung Lee, Chang-Lyoul Lee, Jin Young Kim, Hyeon Suk Shin, and Myoung Hoon Song, "Highly Efficient Polymer Light-Emitting Diodes Using Graphene Oxide as a Hole Transport Layer", ACS Nano, 2012, 6, 2984–2991
4. **Dongwoo Kang**, Jee Youn Kwon, Hyun Cho, Jae-Hyoung Sim, Hyun Sick Hwang, Chul Su Kim, Yong Jung Kim, Rodney S. Ruoff, and Hyeon Suk Shin, "Oxidation Resistance of Iron and Copper Foils Coated with Reduced Graphene Oxide Multilayers", ACS Nano, 2012, 6, 7763–7769
5. A-Rang Jang, Eun Kyung Jeon, **Dongwoo Kang**, Gwangwoo Kim, Byeong-Su Kim, Dae Joon Kang, and Hyeon Suk Shin, "Reversibly Light-Modulated Dirac Point of Graphene Functionalized with Spiropyran", ACS Nano, 2012, 6, 9207–9213
6. Jung Woo Kim, **Dongwoo Kang**, Tae Hyeong Kim, Sung Guk Lee, Nami Byun, Dong Wook Lee, Byung Hwa Seo, Rodney S. Ruoff, and Hyeon Suk Shin, "Mosaic-like Monolayer of Graphene Oxide Sheets Decorated with Tetrabutylammonium Ions", ACS Nano, 2013, 7, 8082–8088
7. Jieun Yang, Damien Voiry, Seong Joon Ahn, **Dongwoo Kang**, Ah Young Kim, Manish Chhowalla, and Hyeon Suk Shin, "Two-Dimensional Hybrid Nanosheets of Tungsten Disulfide and Reduced Graphene Oxide as Catalysts for Enhanced Hydrogen Evolution", Angew. Chem. Int. Ed. 2013, 52, 13751 –13754
8. Sang-Ha Hwang, **Dongwoo Kang**, Rodney S. Ruoff, Hyeon Suk Shin*, and Young-Bin Park*, "Poly(vinyl alcohol) Reinforced and Toughened with Poly(dopamine)-Treated Graphene Oxide, and Its Use for Humidity Sensing", ACS Nano, 2014, 8, 6739–6747 **(Sang-Ha Hwang and Dongwoo Kang were equal major contributors to this work)**
9. **Dongwoo Kang**, Young-Eun Shin, Hyunhyub Ko and Hyeon Suk Shin, "Mechanical properties of poly(dopamine)-coated graphene oxide and poly(vinyl alcohol) composite fibers coated with reduced graphene oxide and their use for piezoresistive sensing", Part. Part. Syst. Charact., Submitted.

[Acknowledgement]

학위 과정 중에 많은 일들이 있었습니다. 우여곡절 끝에 도착한 종착점에서 마음이 홀가분하지 만은 않은 것은 그냥 흘려 보낸 후회되는 시간들이 많았기 때문인 것 같습니다. 그래도 무사히 학위 과정을 마칠 수 있게 물심양면으로 보살펴 주신 아버지, 어머니 그리고 장인 어른과 장모님께 정말 감사하다는 말을 전하고 싶습니다. 힘들 때마다 제 편이 되어주고 용기를 주었던 사랑하는 아내 경희에게도 고맙고, 사랑한다고 전하고 싶습니다. 항상 인생의 본보기가 되어준 형과 형수님 그리고 세상에서 제일 귀여운 우리 조카 예림이도 고맙습니다. 진주의 병현이 형님도 너무 고맙고 갚아야할 고마운 마음의 짐이 많습니다. 우리고 가족들에게 보답하며, 떳떳하고 자랑스러운 사람이 되도록 항상 노력하며 살겠습니다.

지도 교수님 이신 신현석 교수님께는 원망스러운 마음이 많았지만, 돌이켜 보면 한편으로는 죄송한 마음도 컸습니다. 학위 과정 중 가져야할 마음가짐을 항상 일깨워 주시고, 많은 가르침을 주셔서 정말 감사합니다. 그리고 학위 과정 중에 연구실에서 만났던 많은 선배후배 분들(양지은, 이동욱, 이지숙, 김정우, 장아랑, 김병환, 김해식, 임현섭, 윤창성, 김광우, 윤성인, 안성준, 이훈주, 마경열, 조혜진, 홍석모, 박영진, 현초희, 남한재, 장윤정) 에게도 정말 고맙다는 말을 전하고 싶습니다. 그 외에도 오피스에서 동고동락했던 많은 선후배들과 힘들 때 술잔을 같이 기울여 주던 고등학교, 대학교 친구 및 선후배분들께도 감사 드립니다.

짧지 않았던 울산에서의 삶과 인생의 중요한 전환점을 마무리 할 수 있어 다행입니다. 다시 한번 도와 주신 모든 분들과 하느님께 감사 드립니다.